

AD-A042 338

UNITED TECHNOLOGIES CORP STRATFORD CONN SIKORSKY AIR--ETC F/G 1/3
INVESTIGATION OF THE COMPLIANT ROTOR CONCEPT.(U)

JUN 77 R H BLACKWELL

DAAJ02-76-C-0003

UNCLASSIFIED

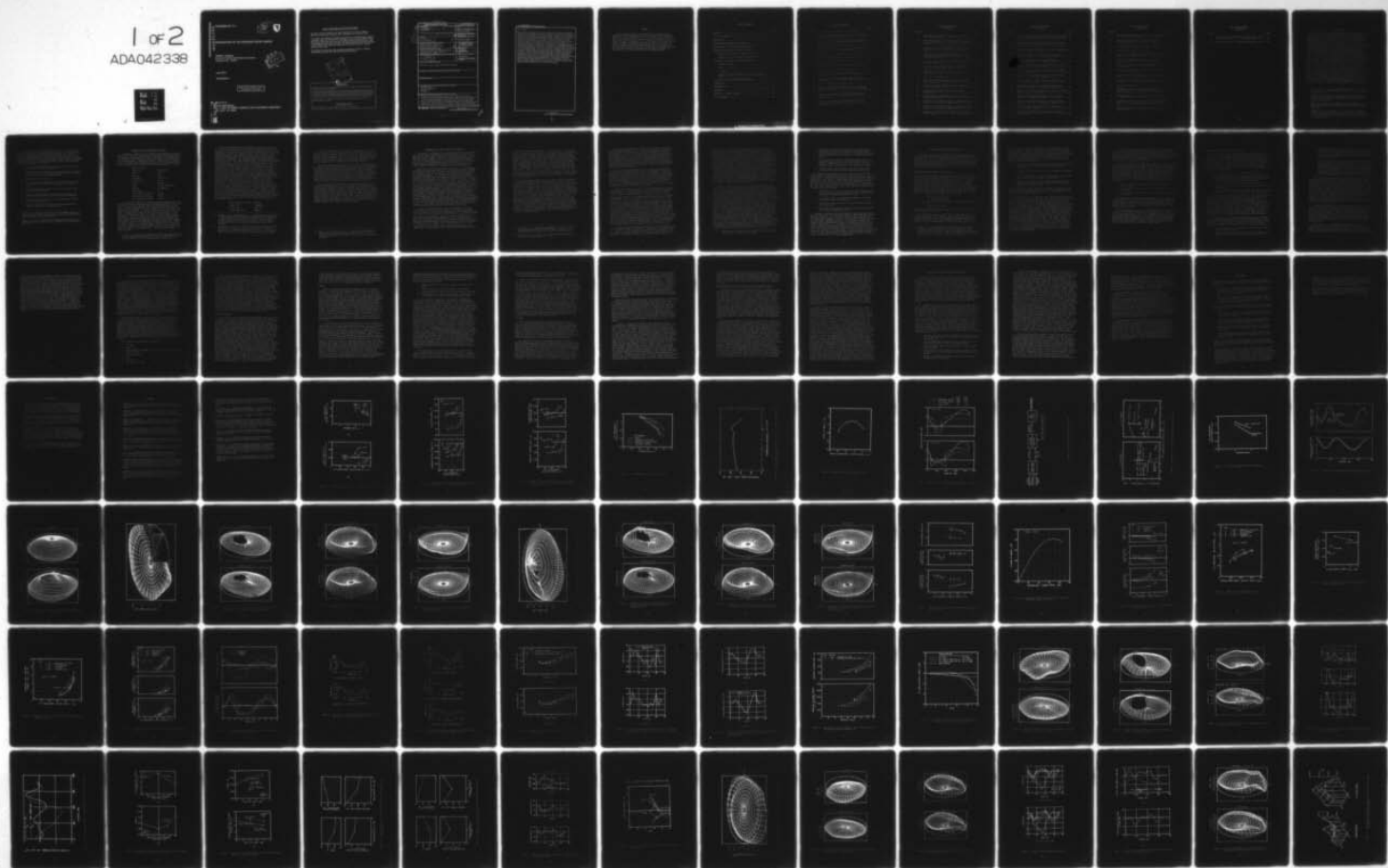
SER-50985

USAAMRDL-TR-77-7

NL

1 of 2

ADA042338



AD A 042338

USAAMRDL-TR-77-7

12
NW



INVESTIGATION OF THE COMPLIANT ROTOR CONCEPT

SIKORSKY AIRCRAFT
Division of United Technologies Corporation
Stratford, Conn. 06602



June 1977

Final Report

Approved for public release;
distribution unlimited.

DDC FILE COPY

Prepared for
EUSTIS DIRECTORATE
U. S. ARMY AIR MOBILITY RESEARCH AND DEVELOPMENT LABORATORY
Fort Eustis, Va. 23604

EUSTIS DIRECTORATE POSITION STATEMENT

This report has been reviewed by the Eustis Directorate, U.S. Army Air Mobility Research and Development Laboratory and is considered to be technically sound.

This program was initiated to investigate the potential for using blade torsional response to favorably modify the distribution of a helicopter's main rotor blade's angle of attack. Blade design features that result in an elastic twisting response that reduces rotor loads and improves performance were identified. The operating capabilities and flight envelopes of two compliant rotor designs were calculated and compared to those of a present-generation rotor system.

This program was conducted under the technical management of Mr. D. J. Merkley, Aeromechanics Technical Area, Technology Applications Division.

PROCESSING for	Write Section <input checked="" type="checkbox"/>
NTIS	Buff Section <input type="checkbox"/>
DCG	
UNCLASSIFIED	
JUSTIFICATION	
BY	DISTRIBUTION/AVAILABILITY CODES
DATE	DATE and/or SPECIAL

[Handwritten signature]

DISCLAIMERS

The findings in this report are not to be construed as an official Department of the Army position unless so designated by other authorized documents.

When Government drawings, specifications, or other data are used for any purpose other than in connection with a definitely related Government procurement operation, the United States Government thereby incurs no responsibility nor any obligation whatsoever; and the fact that the Government may have formulated, furnished, or in any way supplied the said drawings, specifications, or other data is not to be regarded by implication or otherwise as in any manner licensing the holder or any other person or corporation, or conveying any rights or permission, to manufacture, use, or sell any patented invention that may in any way be related thereto.

Trade names cited in this report do not constitute an official endorsement or approval of the use of such commercial hardware or software.

DISPOSITION INSTRUCTIONS

Destroy this report when no longer needed. Do not return it to the originator.

Unclassified

SECURITY CLASSIFICATION OF THIS PAGE (When Data Entered)

REPORT DOCUMENTATION PAGE		READ INSTRUCTIONS BEFORE COMPLETING FORM	
1. REPORT NUMBER USAAMRDL-TR-77-7	2. GOVT ACCESSION NO.	3. RECIPIENT'S CATALOG NUMBER	
4. TITLE (and Subtitle) INVESTIGATION OF THE COMPLIANT ROTOR CONCEPT	5. TYPE OF REPORT & PERIOD COVERED Technical Report		
7. AUTHOR(s) Robert A. H. Blackwell	8. CONTRACT OR GRANT NUMBER(s) DAAJ02-76-C-0003 new		
9. PERFORMING ORGANIZATION NAME AND ADDRESS Sikorsky Aircraft Division of United Technologies Corporation Stratford, Conn. 06602	10. PROGRAM ELEMENT, PROJECT, TASK AREA & WORK UNIT NUMBERS 62209A-1F262209AH76 00 138 EK		
11. CONTROLLING OFFICE NAME AND ADDRESS Eustis Directorate, U.S. Army Air Mobility Research and Development Laboratory Fort Eustis, Va. 23604	12. REPORT DATE June 1977		
14. MONITORING AGENCY NAME & ADDRESS (if different from Controlling Office) (12) 109p.	13. NUMBER OF PAGES 115		
16. DISTRIBUTION STATEMENT (of this Report) Approved for public release; distribution unlimited.		15. SECURITY CLASS. (of this report) Unclassified	
17. DISTRIBUTION STATEMENT (of the abstract entered in Block 20, if different from Report)			
18. SUPPLEMENTARY NOTES			
19. KEY WORDS (Continue on reverse side if necessary and identify by block number) Helicopter Rotor Torsional Flexibility Dynamic Twist Tip Sweep			
20. ABSTRACT (Continue on reverse side if necessary and identify by block number) An analytic investigation was conducted to determine the feasibility of improving helicopter performance and reducing flight loads by passive control of blade torsional response. Distributions of time-varying blade elastic twist that improve performance and decrease blade stress are identified. Blade design features producing the desired twisting are then sought through examination of model and full-scale torsional response data and through an analytic evaluation of significant parameters. Results indicate a significant			

DD FORM 1 JAN 73 1473 EDITION OF 1 NOV 65 IS OBSOLETE

Unclassified

SECURITY CLASSIFICATION OF THIS PAGE (When Data Entered)

323 800

1/B

Unclassified

SECURITY CLASSIFICATION OF THIS PAGE(When Data Entered)

20. ABSTRACT

potential for inducing 1P and 2P elastic twisting. Tip sweep on a blade of reduced torsional stiffness improves performance and reduces control loads and blade stress by inducing a 1P torsional response, which decreases advancing-blade twist and increases retreating-blade twist. Negative airfoil camber is shown to reduce blade stress but generally degrade performance. Control of the spanwise distribution of aerodynamic center--elastic axis offset is shown to be effective in producing 2P elastic twist, which improves forward-flight performance. The potential for improving hover performance by inducing large negative elastic twist is demonstrated. Preliminary design of two compliant rotors is accomplished. Relative to a conventional baseline rotor, both designs employ four-to-one torsional stiffness reductions outboard of the 50-percent radius. The first design uses a 20-degree swept tip at the 90-percent radius to induce 1P elastic twist, which improves rotor L/D by an average of 4 percent for the conditions analyzed. Vibratory pushrod loads are reduced by up to 50 percent, and blade flatwise stress is reduced by approximately 10 percent. The second design has its aerodynamic center 15 percent of the chord forward of the elastic axis from 63- to 86-percent radius, and 20-degree swept tip at 90-percent radius. This design produces 2P elastic pitching, which improves rotor L/D by approximately 7 percent, and reduces flatwise stress by from 10 to 20 percent. Vibratory hub forces are increased by the introduction of 2P elastic pitching.

Unclassified

SECURITY CLASSIFICATION OF THIS PAGE(When Data Entered)

PREFACE

The work reported herein was performed by the Sikorsky Aircraft Division of United Technologies Corporation under Contract DAAJ02-76-C-0003 for the Eustis Directorate, U.S. Army Air Mobility Research and Development Laboratory, Fort Eustis, Virginia. The work was carried out under the technical cognizance of Mr. Donald Merkley of the Eustis Directorate, USAAMRDL. The program was conducted under the management of Sikorsky Aeromechanics Branch Manager Mr. Peter Arcidiacono and Aeromechanics Chief of Dynamics Mr. William Kuczynski. Aeromechanics personnel involved directly in the program were Mr. Robert Blackwell, Mr. Robert Moffitt, Mr. Robert Studwell, and Mr. Lawrence Levine.

TABLE OF CONTENTS

	<u>Page</u>
PREFACE	3
LIST OF ILLUSTRATIONS.....	6
INTRODUCTION	11
DEFINITION OF REFERENCE ROTOR ATTRIBUTES	13
DETERMINATION OF IDEAL ROTOR ELASTIC TWISTING	16
EXAMINATION OF ROTOR ELASTIC TWIST TEST DATA	21
Examination of Model Rotor Elastic Twist Data	21
Examination of CH-53D Swept Tip Flight Test Data	24
EVALUATION OF COMPLIANT ROTOR DESIGN PARAMETERS	27
Torsional Stiffness	28
Camber	29
Tip Sweep	31
Chordwise Location of Blade Elastic Axis and Aerodynamic Center	33
SELECTION OF OPTIMAL COMPLIANT ROTOR DESIGNS	35
CONCLUSIONS	38
RECOMMENDATIONS	40
REFERENCES	41
APPENDIX A - ANALYTIC METHODS	109
LIST OF SYMBOLS	113

LIST OF ILLUSTRATIONS

<u>Fig. No.</u>		<u>Page</u>
1	Calculation of Reference Rotor Stall Boundaries	43
2	Buildup of Reference Rotor Power and Flatwise Stress With Advance Ratio and Lift Coefficient	44
3	Buildup of Reference Rotor 3P Rotating Vertical Hub Shear and Pushrod Loads with Advance Ratio and Lift Coefficient	45
4	Stall Boundaries of the Reference Rotor	46
5	Perceived Noise Levels of the Reference Rotor for 250-ft Altitude Flyover at $\mu = 0.4$ and $C_L/\sigma = 0.085$	47
6	Hover Figure of Merit of Reference Rotor	48
7	Angle of Attack Distribution of Ideal Rotors at $\mu = 0.4$.	49
8	Maximum L/Q_D Rotor Iteration Process	50
9	Equivalent Lift-to-Drag Ratios of Reference and Ideal Rotors	51
10	Reference and Ideal Rotor Stall Boundaries	52
11	Reduction of Profile Drag Torque With Maximum L/Q_D Rotor	53
12	Comparison of Reference and Maximum L/Q_D Rotor Twist Distributions at $\mu = 0.3$ and $C_L/\sigma = 0.10$ (Uniform Inflow)	54
13	The Use of Compliant Rotor Surface Plots	55
14	Comparison of Reference and Maximum L/Q_D Rotor Angle of Attack Distributions at $\mu = 0.3$ and $C_L/\sigma = 0.10$ (Uniform Inflow)	56
15	Comparison of Reference and Maximum L/Q_D Rotor Airload Distributions at $\mu = 0.3$ and $C_L/\sigma = 0.10$ (Uniform Inflow)	57
16	Comparison of Reference and Maximum L/Q_D Rotor Profile Drag Torque Distributions at $\mu = 0.3$ and $C_L/\sigma = 0.10$ (Uniform Inflow)	58

LIST OF ILLUSTRATIONS

(continued)

<u>Fig. No.</u>		<u>Page</u>
17	Twist Required to Maximize L/Q_D at $\mu = 0.3$ and $C_L/\sigma = 0.10$ (Variable Inflow)	59
18	Comparison of Reference and Maximum L/Q_D Rotor Angle of Attack Distributions at $\mu = 0.3$ and $C_L/\sigma = 0.10$ (Variable Inflow)	60
19	Comparison of Reference and Maximum L/Q_D Rotor Airload Distributions at $\mu = 0.3$ and $C_L/\sigma = 0.10$ (Variable Inflow)	61
20	Comparison of Reference and Maximum L/Q_D Rotor Profile Drag Torque Distributions at $\mu = 0.3$ and $C_L/\sigma = 0.10$ (Variable Inflow)	62
21	Variation of Ideal Rotor Twist with Advance Ratio and Lift Coefficient	63
22	Variation of Hover Figure of Merit with Equivalent Linear Twist Angle at $C_T/\sigma = 0.10$	64
23	Variation of Model Rotor Elastic Twist with Lift Coefficient at $\mu = 0.3$	65
24	Model Rotor Performance Data at $\mu = 0.3$	66
25	Effect of 1P Lateral Twisting on 9-ft-diameter Model Rotor Performance at $\mu = 0.3$	67
26	Buildup of Vibratory Blade Root Torsional Moments with Lift Coefficient at $\mu = 0.3$	68
27	Buildup of Fixed System Control Loads with Lift Coefficient at $\mu = 0.3$	69
28	Torsional Deflection and Flatwise Stress of Three 9-ft Diameter Model Rotors at $\mu = 0.3$	70
29	The Effect of H-53 Blade Tip Sweep on Pushrod Load Time Histories at 150 Knots at 42,000 lb Lift	71
30	The Effect of H-54 Blade Tip Sweep on Pushrod Load Time Histories at 150 Knots and 42,000 lb Lift	72
31	The Effect of Tip Sweep on the Buildup of H-54 Blade Flatwise Stress	73

LIST OF ILLUSTRATIONS

(continued)

<u>Fig. No.</u>		<u>Page</u>
32	Comparison of Measured and Predicted Effects of Tip Sweep on Pushrod Load Time Histories of H-54 Blade at 150 Knots and 42,000 lb Lift	74
33	Comparison of Measured and Predicted Effects of Tip Sweep on Flatwise Stress Time Histories of H-54 Blade at 150 Knots and 42,000 lb Lift	75
34	Measured and Calculated Buildup of H-54 Blade Pushrod Loads and Flatwise Stress at 42,000 lb Lift	76
35	Variation of Blade Torsional Response Amplitude With Torsional Stiffness at $\mu = 0.4$ and $C_L/\sigma = 0.085$	77
36	Effect of Negative Camber on the Distribution of Torsional Response at $\mu = 0.4$ and $C_L/\sigma = 0.085$	78
	Effect of Negative Camber on the Distribution of Angle of Attack at $\mu = 0.4$ and $C_L/\sigma = 0.085$	79
38	Effect of Negative Camber on the Distribution of Airloads at $\mu = 0.4$ and $C_L/\sigma = 0.085$	80
39	Effect of Negative Camber on the Distribution of Blade Torque at $\mu = 0.4$ and $C_L/\sigma = 0.085$	81
40	Effect of Negative Camber on Maximum Flatwise Stress at $\mu = 0.4$ and $C_L/\sigma = 0.085$	82
41	Variation of Flatwise Stress and Power With Pitching Moment Coefficient at $\mu = 0.4$ and $C_L/\sigma = 0.085$	83
42	Variation of Power and Flatwise Stress With Built-In Twist Angle for $c_{m_0} = +0.015$ and $+0.03$	84
43	Variation of Power and Rotor System Loads With Sweep Angle at $\mu = 0.4$ and $C_L/\sigma = 0.085$	85
44	Variation of Power and Rotor System Loads With Spanwise Location of Sweep at $\mu = 0.4$ and $C_L/\sigma = 0.085$	86
45	Effect of Sweep on the Distribution of Blade Torque at $\mu = 0.4$ and $C_L/\sigma = 0.085$	87
46	Reduction of Advancing Blade Drag Torque With Swept Tip Compliant Rotor	88

LIST OF ILLUSTRATIONS

(continued)

<u>Fig. No.</u>		<u>Page</u>
47	Aerodynamic Pitching Moment of Swept Tip Compliant Rotor at $\mu = 0.4$ and $C_L/\sigma = 0.085$	89
48	Effect of Tip Sweep on the Distribution of Blade Torsional Response at $\mu = 0.4$ and $C_L/\sigma = 0.085$	90
49	Effect of Tip Sweep on the Distribution of Airloads at $\mu = 0.4$ and $C_L/\sigma = 0.085$	91
50	Reference Rotor Airload Time Histories	92
51	Effect of Forward Midspan Aerodynamic Center on Elastic Twist at $\mu = 0.4$ and $C_L/\sigma = 0.085$	93
52	Effect of Forward Midspan Aerodynamic Center on the Distribution of Airload at $\mu = 0.4$ and $C_L/\sigma = 0.085$	94
53	Variation of Required Power and Flatwise Stress With Tip Sweep and Camber at $\mu = 0.4$ and $C_L/\sigma = 0.085$	95
54	Variation of Control Loads With Tip Sweep and Camber at $\mu = 0.4$ and $C_L/\sigma = 0.085$	96
55	Variation of 3P Vertical Hinge Force With Tip Sweep and Camber at $\mu = 0.4$ and $C_L/\sigma = 0.085$	97
56	Penalty Functions Illustrating the Effects of Tip Sweep and Camber	98
57	Compliant Rotor Designs	100
58	The Buildup of Power, Stress, Control Loads, and Vibratory Shear Force for Compliant Rotor Design #1 and Reference Rotor	101
59	Operating Boundaries of Compliant Rotor Design #1 and Reference Rotor	103
60	The Buildup of Power, Stress, Control Loads, and Vibratory Shear Force for Compliant Rotor Design #2 and Reference Rotor	104
61	Operating Boundaries of Compliant Rotor Design #2 and Reference Rotor	106

LIST OF ILLUSTRATIONS

(continued)

<u>Fig. No.</u>		<u>Page</u>
62	Flyover Perceived Noise Levels of Compliant Rotor Designs and Reference Rotor at $\mu \approx 0.4$ and $C_L/\sigma = 0.085$	107
63	Hover Figure of Merit of Reference and Compliant Rotors ..	108

INTRODUCTION

Two problems constrain the flight capability of conventional helicopters. The first is the less-than-optimal use of available power. The second is the buildup of rotor system loads and vibratory hub forces. Aerodynamic efficiency of fixed-geometry blades inevitably decreases in high-speed flight as regions of the rotor disc become disproportionately loaded. Rotor and control-system loads build up as a direct result of increasingly severe advancing-blade compressibility effects combined with retreating-blade stall effects. In seeking to relieve the various forward-flight limitations and maintain good hover performance, blade designers are faced with trade-offs in establishing such parameters as radius, airfoil, planform, and twist. Lack of a detailed airload prediction capability, together with concern for the complexity of blades with in-flight varying geometry, has typically resulted in a fixed-geometry design which is a compromise between those desired for the different operating regimes. More recently, rotors with controllable twist, circulation, or flap deflection, and rotors with multicyclic feathering have been proposed to alter blade or control-system characteristics with flight condition or blade position to achieve improved loading distributions. Improvements in performance and reductions in flight loads have been demonstrated with these mechanisms (References 1-4). In each case, active pitch (loading) control is achieved at some penalty in system simplicity, cost, or reliability. A desirable objective is to achieve the benefits of active control devices by passively controlling blade torsional response through proper aeroelastic design. If blade aerodynamic and structural properties can be selected so that torsional response to applied aerodynamic loads matches that supplied by an active device, improvements in operating capability can be obtained without the potential attendant weight and cost penalties of active control approaches. With passive control, the blades naturally tend to comply with desired pitch requirements. A rotor based on these principles is referred to in this report as a compliant rotor.

1. Lemnios, A. Z., et al., FULL SCALE WIND TUNNEL TESTS OF A CONTROL-LABLE TWIST ROTOR, American Helicopter Society, 32nd Annual National Forum, May 1976
2. McCloud, J. L., and Kretz, M., MULTICYCLIC JET FLAP CONTROL FOR ALLEVIATION OF HELICOPTER BLADE STRESSES AND FUSELAGE VIBRATION, American Helicopter Society, Specialists' Meeting on Rotorcraft Dynamics, February 1974
3. McHugh, F. H., and Shaw, J., BENEFITS OF HIGHER HARMONIC BLADE PITCH: VIBRATION REDUCTION, BLADE LOAD REDUCTION, AND PERFORMANCE IMPROVEMENT, American Helicopter Society, Symposium on Rotor Technology, August 1976
4. Balcerak, J. C., and Erickson, J. C., SUPPRESSION OF TRANSMITTED HARMONIC VERTICAL AND INPLANE ROTOR LOADS BY BLADE PITCH CONTROL, Cornell Aeronautical Laboratory; USAAVLABS Technical Report 69-39, U.S. Army Aviation Materiel Laboratories, Fort Eustis, Virginia, July 1969, AD 860352

Past designs have demonstrated favorable effects of compliant design concepts. The Sikorsky swept-tip blade reduced control loads and blade stress by altering blade torsional response (Reference 5). Tests of reduced-stiffness blades with swept tips and negative camber reported in Reference 6 demonstrated significant reduction in blade stress. In general, however, there exists little detailed information which quantifies potential compliant rotor benefits and identifies design criteria. The objectives of the present study are as follows:

1. Define ideal compliant rotor twisting and quantify the effects on performance and rotor system loads.
2. Provide preliminary compliant rotor design guidelines by identifying the effects of blade design parameters for improving rotor capability by inducing favorable twisting.

The following approach was adopted:

1. Define the hover performance and level flight operating limits of a baseline (noncompliant) rotor designed for a transport mission.
 2. Identify improvements in flight capability achievable through idealized elastic twisting.
 3. Examine existing test data to identify blade parameters and compliant mechanisms which tend to produce desired twisting.
 4. Determine and evaluate the type of twist produced by a variety of blade design parameters.
 5. Evolve two compliant rotor designs providing expanded flight capability relative to the baseline rotor.
-
5. Prillwitz, R., STRUCTURAL EVALUATION OF HIGH PERFORMANCE ROTOR BLADE SWEPT TIPS, Engineering Report SER-651073, Sikorsky Aircraft Division, United Technologies Corp., October 1972
 6. Doman, G. S., et al., INVESTIGATION OF AEROELASTICALLY ADAPTIVE ROTOR SYSTEMS, American Helicopter Society, Symposium on Rotor Technology, August 1976

DEFINITION OF REFERENCE ROTOR ATTRIBUTES

To provide a reference for the compliant rotor designs to be evolved later in the study, the design and level-flight operating capabilities of a conventional (noncompliant) rotor were established. This design served as a baseline for the parametric evaluation of compliant rotor parameters to be discussed below. Although the compliant rotor concept has applicability to a range of helicopter missions, the focus of the present study was a transport mission. Baseline rotor design parameters are as follows:

number of blades	4
rotor type	articulated
radius	26.5 ft
solidity	.083
tip speed	730 ft/sec
offset ratio	.047
airfoil	SC 1095
twist	-12 deg (nonlinear)
planform	rectangular
Locke number	10
first flatwise frequency	2.8/rev
first edgewise frequency	4.8/rev
first torsional frequency	5.2/rev

To establish the approximate operating limits of the reference rotor, the NASA rotary-wing performance charts presented in Reference 7 were used in conjunction with the Sikorsky Generalized Rotor Performance program (GRP). The GRP analysis and the other analyses used in the study are described in the Appendix. Reference 7 shows that the blade profile drag torque parameter, bC_{QD}/σ , is a reliable indicator of the degree of rotor stall. Examination of flight-test data has shown that $bC_{QD}/\sigma = 0.004$ indicates incipient stall (lower stall limit) and that $bC_{QD}/\sigma = 0.008$ corresponds to deep stall (upper stall limit). Operation beyond the upper stall limit is typically prohibitive, based on power requirements and control-system loads. The rigid-blade GRP analysis was used to determine the buildup of the stall parameter with airspeed and rotor lift. Results are shown in Figure 1. The combinations of advance ratio and rotor lift coefficient analyzed are denoted by symbols in Figure 1(a). Figure 1(b) shows the variation of the stall parameter in relation to the lower stall limit and identifies the combinations of μ and C_L/σ corresponding to incipient stall.

-
7. Tanner, W. H., CHARTS FOR ESTIMATING ROTARY WING PERFORMANCE IN HOVER AND HIGH FORWARD SPEEDS, Engineering Report SER-50379, Sikorsky Aircraft Division, United Technologies Corp., August 1964

Rotor-load and performance characteristics were then calculated in the vicinity of the GRP stall boundary using the Normal Modes Blade Aeroelastic Analysis (Appendix). Because they were shown in Reference 8 to be necessary for accurate modeling of control loads and blade stress, unsteady aerodynamics and nonuniform inflow were used. The so-called α , A, B unsteady aerodynamic model described in Reference 9 was used. Variable inflow was calculated using the UTRC Prescribed Wake Inflow Analysis described in the Appendix. The buildups of main rotor power, blade stress, vibratory hub loads, and control-system loads were calculated and compared to allowable levels. The variation of significant measures of these quantities are presented versus μ and C_L/σ in Figures 2 and 3. The main rotor power requirements shown in Figure 2(a) include parasite power corresponding to an aircraft equivalent flat plate area, f , of 25 ft². Flatwise bending stress, shown in Figure 2(b), was the most significant source of blade stress. At the 60-percent span station where maximum total stress was generally predicted, edgewise bending stresses were found to be less than 15 percent of the total. Peak-to-peak levels of pushrod load were selected as the measure of control-system loads, because they reflect in a single parameter both the high frequency stall-induced torsional loads (which cause bP fixed-system control loads), and 1P camber-, twist-, and sweep-induced torsion moments, which contribute significantly to steady fixed-system loads. A significant indicator of the level of vibratory hub loads is the 3P rotating system vertical shear force at the hinge. Vibration trends generally follow predicted levels of 3P, 4P, and 5P rotating system shear forces. The 3P component was used because it is most reliably predicted by analysis. It should be pointed out that vibratory hub loads present a less fundamental limit than the other rotor loads, because resulting vibration can be controlled by detuning airframe modes or adding vibration-suppression equipment. Flight envelope restrictions based on each of the four loads were established, based on the following limits:

available main rotor power	2800 hp
flatwise stress	$\pm 17,000$ psi
pushrod load	± 1400 lb
3P hinge axial force	± 800 lb

-
8. Blackwell, R. H., and Commerford, G. L., INVESTIGATION OF THE EFFECTS OF BLADE STRUCTURAL DESIGN PARAMETERS ON HELICOPTER STALL BOUNDARIES, Sikorsky Aircraft Division, United Technologies Corp., USAAMRDL Technical Report 74-25, Eustis Directorate, U.S. Army Air Mobility Research and Development Laboratory, Fort Eustis, VA, May 1974, AD 784594
 9. Arcidiacono, P. J., et al., INVESTIGATION OF HELICOPTER CONTROL LOADS INDUCED BY STALL FLUTTER, Sikorsky Aircraft Division, United Technologies Corp.; USAAVLABS Technical Report 70-2, U.S. Army Aviation Materiel Laboratories, Fort Eustis, Virginia, March 1970, AD 869823

Limits were estimated based on existing design trends. Actual limits of a given design would, of course, depend upon detailed blade, control system, airframe, and engine definition. The stress limit is based on the endurance limit of titanium. The flight envelope as determined by each of the rotor loads is shown in Figure 4. Based on the somewhat arbitrary set of load limits given above, power and vibratory hub load represent the primary limitations to the forward-flight operating envelope.

In order to permit an evaluation of the acoustic characteristics of the compliant rotor designs, perceived noise levels (PNL) of the reference rotor were calculated using the Sikorsky Aircraft version of HERON II, the Lowson-Ollerhead noise prediction method (Reference 10). This method calculates drag rise noise due to compressibility effects, and accounts for the effects on rotor noise of blade twist, tip geometry and airload distribution. PNL were calculated at several field points to generate a flyover history as a function of rotor/observer separation distance. Figure 5 presents the results for a flight condition corresponding to the operating limit of the reference rotor at an advance ratio of 0.4.

Hover performance of the reference rotor was calculated using the Sikorsky Circulation Coupled Hover Analysis Program (CCHAP), which is described in the Appendix. A recent refinement to this analysis allows the treatment of flatwise bending and torsional windup in the calculation of rotor inflow velocities and hover performance. This feature is particularly valuable for the investigation of compliant rotor hover performance. Figure 6 shows the hover figure of merit (FM) of the reference rotor as a function of thrust coefficient-solidity ratio. The elastic windup of the baseline rotor is approximately -2.5 degrees. Reference rotor-hover and forward-flight data of Figures 2 through 6 will be compared with corresponding compliant rotor results later in the report.

-
10. Lowson, M. V., and Ollerhead, J. B., STUDIES OF HELICOPTER ROTOR NOISE, Wyle Laboratories; USAAVLABS Technical Report 68-60, U.S. Army Aviation Materiel Laboratories, Fort Eustis, VA, January 1969, AD 684394

DETERMINATION OF IDEAL ROTOR ELASTIC TWISTING

The potential for expanding the operating capability of the reference rotor through ideal compliant rotor twisting was the next subject to be addressed. In effect, the capability of a rotor with completely controllable twisting was examined. This effort defined the hover twist and the time-varying forward-flight twist of an ideal compliant rotor without regard for the loading mechanisms needed to achieve them. The search for realistic means of achieving desired twisting is the subject of the section entitled "Evaluation of Compliant Rotor Design Parameters."

Elastic twist can be used to improve several of the rotor attributes which limit forward-flight capability. The torsional responses required to reduce each of the loads are not necessarily identical and trade-offs are inevitably required. For example, twist which reduces blade stress may degrade performance. It is, therefore, essential that compliant response be directed toward relieving primary limitation both in terms of absolute flight boundaries and efficiency at design conditions. A fundamental level-flight limit of the reference rotor is installed power (Figure 4). A variety of methods exist for reducing blade stress or vibration to satisfactory levels in either design or experimental development. Control loads can be tolerated by strengthening control-system hardware and paying the accompanying weight penalty. It should also be noted that level-flight control loads, although they build up with stall, generally remain below design levels which for military aircraft are based on maneuvers. The latitude for improving aerodynamic flight capability for a given installed power is generally smaller. Power required necessarily builds up with airspeed and lift. A common result is an aircraft for which rotor loads are nondamaging within the aerodynamically defined operating envelope. For this reason, examination of ideal compliant rotor twisting concentrated on responses which improve performance both at cruise and extreme conditions. It is anticipated that performance improvements which result from avoiding retreating blade stall will also reduce control loads.

A number of ideal-performance rotors were examined. Two ideal-performance rotors which have been proposed in the past were examined first. Performance characteristics and angle-of-attack distributions were calculated for a rotor having each blade element at $c_{l_{max}}$ and for a second rotor having blade elements at the angle of attack for maximum l/d . In each case, the effects of Mach number and reverse flow were treated. Rotor net rolling moment was balanced by constraining outboard sections of the advancing blade to operate at negative angles of attack corresponding to $-(l/d)_{max}$ and $-c_{l_{max}}$ subject to the constraint that $c_d \leq .1$. These constraints specify one angle-of-attack distribution and rotor lift coefficient at a given advance ratio. Similar investigations reported in

Reference 11 showed the potential of a $c_{l_{max}}$ ideal rotor for increasing rotor lift capability while avoiding stall. Angle-of-attack time histories of the two ideal performance rotors are compared in Figure 7 to those calculated for the reference rotor in the vicinity of the stall boundary ($bC_{QD}/\sigma = 0.004$). These results based on uniform inflow and steady aerodynamics correspond to an advance ratio of 0.4. The lift coefficients and lift-to-equivalent-drag ratios achieved by the three rotors are shown. Rotor equivalent drag, D_E , is the drag of a body which absorbs the same power in translating at airspeed V as the rotor uses in producing lift. ($D_E V = 550[HP - HP_{PAR}]$). The ratio of lift to equivalent drag is a convenient measure of rotor efficiency. The $c_{l_{max}}$ rotor has a high lift capability but a low L/D_E . At this condition, the maximum c_l/c_d rotor is more efficient than the reference rotor. At $\mu = 0.3$, however, a rotor with all sections at maximum l/d has a rotor L/D_E worse than that of the reference rotor at the same C_L/σ .

Because the maximum section l/d and c_l criteria did not consistently improve performance and moreover do not identify the manner in which angle of attack should be changed for variations in lift at fixed airspeed, additional criteria were sought. The final criterion selected was the minimization of integrated drag torque at each azimuth while maintaining the lift of the reference blade. The radial distribution of loading which minimizes the integral of blade element drag torque subject to maintaining a specified total blade lift can be determined using variational calculus (Reference 12). For a given relationship between airfoil angle of attack, lift, and drag, the optimal radial distribution of angle of attack is defined. This optimization criteria was used in the Sikorsky Airload Optimization Analysis (Appendix) to determine angle of attack and twist distributions at each azimuth which resulted in a rotor with the maximum total lift-to-drag torque ratio, L/Q_D . It should be pointed out that the effects of induced drag are not included under this optimization criteria. Minimization of induced drag would be a somewhat more involved process because of the need to iterate between airload and resulting inflow distributions in seeking an optimum. Drag torque is the more significant component for high-speed flight.

-
11. Arcidiacono, P. J., THEORETICAL PERFORMANCE OF HELICOPTERS HAVING SECOND AND HIGHER HARMONIC FEATHERING CONTROL, Journal of the American Helicopter Society, Vol. 6, No. 2, April 1961, pp 8-19
 12. Gelfand, I. M., and Fomin, S. V., CALCULUS OF VARIATIONS, Prentice-Hall, Inc., Englewood Cliffs, N. J., 1963

The process of minimizing drag torque with the airload optimization analysis assuming uniform inflow is illustrated in Figure 8. For a given flight condition, the GRP analysis is used to determine the azimuthal distribution of total lift, the required controls, and the inflow angles of a baseline rotor. The airload optimization program then specifies the radial distributions of angle of attack which minimizes drag torque. The required twist is computed based on the desired angles of attack, the control angles, and the inflow angles. Finally, the time-varying twist is impressed upon the baseline blade and the rotor performance is calculated. The process is repeated until the two analyses achieve consistent control angles, flapping, and twisting.

Results of these calculations indicate a significant potential for improving rotor forward-flight performance. Improvements in efficiency achieved with the maximum L/Q_D rotor are shown in Figure 9. Expansion of the reference rotor power boundary, based on the 2800-hp limit, is shown in Figure 10. Results are based on uniform inflow and steady aerodynamics. Rotor lift-to-equivalent-drag ratios show consistent improvements over those of the reference rotor at advance ratios of 0.3 and 0.4 (Figure 9). At $\mu = 0.3$, the maximum L/Q_D rotor achieves a 20-percent increase in maximum C_L/σ . Points denoting the performance of the $c_{l_{\max}}$ and $(c_l/c_d)_{\max}$ rotors described above are included for comparison.

The performance gains predicted for the maximum L/Q_D rotor can be put into perspective by comparing results to those of two ideal minimum-drag rotors. Figure 9 shows the equivalent lift-to-drag ratio of a rotor for which every blade section operates at $c_{d_{\min}}$ as a function of Mach number (Curve 1), and of a rotor which suffers no drag rise as a function of Mach number, i.e., $c_d = c_{d_{\text{inc}}}$ (Curve 2). Curve 1 describes a rotor which achieves required lift without exceeding the angle of attack for minimum drag, and therefore defines a limit greater than or equal to what can be achieved through ideal angle of attack optimization. Gains from Curve 1 to Curve 2 are the additional benefits to be achieved by eliminating the effects of compressibility drag rise, possibly through the use of advanced airfoils and tip design, or reduced tip speed. The maximum lifting capability of each rotor is limited by retreating-blade stall as indicated in the figure. It is apparent that the maximum L/Q_D rotor achieves a significant fraction of the performance gains achievable through angle of attack optimization, especially at the 0.4 advance ratio. It is apparent, however, that further gains should be possible by reducing rotor tip speed in order to minimize compressibility losses. Further, results such as these apply to only one airfoil design. Examination of airfoil and tip speed variations were beyond the scope of this investigation.

The nature of the performance improvement achieved by maximizing L/Q_D is illustrated in Figures 11 through 16. Results for the condition shown ($\mu = 0.3$, $C_L/\sigma = 0.10$) are typical of the other points included in Figure 9. Figure 11 compares reference and maximum L/Q_D rotor azimuthal distributions of drag torque coefficient, c_{Q_D} , and blade axial hinge force

coefficient, c_z . As shown, the maximum L/Q_D rotor achieves torque reductions at each azimuth while matching baseline rotor lift. Figure 12 presents a surface plot of the total twist required to maximize L/Q_D . These plots, which are used extensively in this report, are a perspective view of a surface which represents the magnitude of a given quantity as a function of radial and azimuthal position by a vertical displacement from a zero plane. Data needed to define surfaces for all significant aerodynamic and dynamic quantities are stored on file for each performance and blade response calculation. Surface plots, as well as standard XY plots versus azimuth or radius, are then generated on an interactive basis from a graphic display terminal. The vantage point of the observer relative to the surface can be arbitrarily selected. In the plots of Figures 12 through 16, the observation point is located above and directly behind the rotor disc at an elevation angle of about 30 degrees. The primary utility of surface plots is in allowing rapid qualitative assimilation of a large body of data. Quantitative information can, however, be obtained as illustrated in Figure 13. Radial lines can be drawn in the zero plane at azimuth angles of interest. Vertical displacements of points on the surface from corresponding radial lines can then be measured and compared to the vertical scale included with each figure.

Figure 12 compares the twist pattern of the maximum L/Q_D rotor at $\mu = 0.3$ and $C_L/\sigma = 0.10$ with the fixed (built-in) twist of the reference rotor. As shown, the primary features of the ideal rotor twist pattern are a reduction in advancing-blade twist and an increase in retreating-blade twist, especially in the tip region. The manner in which the maximum L/Q_D rotor improves performance is illustrated by surface plots of angle of attack, airload, and elemental drag torque shown in Figures 14, 15, and 16. As shown in Figure 14, the ideal rotor reduces retreating-blade tip angles of attack and avoids negative advancing-blade angles for which $c_d > c_{d_{min}}$ (M). Reverse flow region angles of attack are eliminated for clarity. A comparison of airload distributions in Figure 15 shows a slight tendency to shift high tip airloads inboard. Dramatic savings in drag torque are shown in Figure 16. Drag torque is reduced at every azimuth. Advancing blade tip torque contributions remain high because of the high tip Mach numbers. These data are based on the assumption of uniform inflow. One result of this assumption is the prediction of high angles of attack and drag coefficients at the tip for the baseline rotor. As a result, tip contributions to drag torque may have been overpredicted. To study this question further, the effects of including variable inflow on torque savings and required twist were studied at two flight conditions ($\mu = 0.3$, $C_L/\sigma = 0.10$ and $\mu = 0.4$, $C_L/\sigma = 0.085$). This computation involved iteration between GRP, the Airload Optimization Analysis and the Prescribed Wake Inflow Analysis. Baseline and maximum L/Q_D rotor variable inflow results corresponding to the uniform inflow data given above are presented in Figures 17 through 20. The principal results are as follows:

1. Magnitudes of the torque reductions predicted with uniform and variable inflow are generally comparable.

2. The LP twist requirement calculated with variable inflow is essentially the same as that predicted with uniform inflow. Higher harmonic twisting, in particular a nosedown twisting in the third quadrant of rotor azimuth, is predicted with variable inflow.
3. The reference rotor angle of attack distribution, based on variable inflow, includes a large positive region in the third quadrant. Examination traces this fluctuation to positive induced velocities resulting from close blade-vortex passage.
4. Variable inflow torque reductions result more from avoiding retreating blade stall than from eliminating high tip drag.

The amount and the manner by which the optimal twist varies with flight condition has important implications in the selection of a compliant rotor design. A loading mechanism will be sought which achieves nearly optimal twist for a range of forward-flight conditions and hover. Airload optimization results based on uniform inflow were examined to show the variation in twist requirements with flight condition. Figure 21 shows the total steady twist (built-in twist plus steady elastic twist) and the sine and cosine components of LP elastic twist required for maximum L/Q_D . Four observations can be drawn:

1. At an advance ratio of 0.3, increases in steady (negative) twist and LP sine twist (advancing blade noseup and retreating blade nosedown) are required with increases in C_L/σ .
2. At an advance ratio of 0.4, twist requirements do not change significantly with lift coefficient.
3. The effect of advance ratio is to require increases in steady and LP sine twist.
4. The lateral (LP sine) twist component is more significant than the fore-and-aft component (LP cos).

The impact of twist on hover performance was also examined to determine the ideal value. The variation of figure of merit with linear twist angle was computed at $C_T/\sigma = 0.10$ with the CCHAP analysis (Figure 22). The primary power component in hover is induced power. Moderate increases in twist improve induced efficiency by shifting airloads inboard and creating a more uniform downwash field. The optimal twist predicted by CCHAP is approximately -25 to -30 degrees. Peak figure of merit is 0.76. Blades having such a large amount of built-in twist would necessarily experience large flatwise bending moments in forward flight. It is the goal of the compliant rotor design study to select aerodynamic and structural properties which improve hover performance by inducing steady nosedown elastic twisting and which improve forward-flight performance by inducing a time-varying twist such as that described above.

EXAMINATION OF ROTOR ELASTIC TWIST DATA

To provide guidance for the compliant rotor design analysis, test data for rotors experiencing significant dynamic twisting were examined. Objectives were: first, to define the twisting induced by specific design parameters, and second, to determine the effects of the twisting on rotor performance and blade loads. Two sets of test data which exhibit significant variations in blade torsional response are the 9-ft-diameter model rotor data described in Reference 13 and the full-scale CH-53D swept-tip flight-test data presented in Reference 5.

EXAMINATION OF MODEL ROTOR ELASTIC TWIST DATA

Test data were examined for dynamically scaled H-34 model rotors which incorporated parametric variations in stiffness, twist, and camber. These rotors were not tested in connection with a study of compliance. Three have conventional torsional stiffness and one has an increased torsional stiffness. The goal of the data analysis was to identify elastic twisting mechanisms which could be expected to have powerful effects on a blade of reduced torsional stiffness. The four 9-ft-diameter rotors were tested in the 18-ft test section of the UTRC main wind tunnel under Army Contract DAAJ02-76-C-0026. Rotors were tested to an advance ratio of 0.5 and for various combinations of shaft angle and collective pitch. The following four configurations were tested.

1. a baseline untwisted blade,
2. a 3 x scale stiffness blade,
3. a blade with 20-percent chord, 5 degree deflection plain flap, and
4. a -8-degree twist blade.

Rotors had a solidity of 0.063 and employed an NACA 0012 airfoil section. Rotor tip speed was 330 ft/sec.

The first phase of the data analysis was to define the effects of design parameters on elastic twisting. Blade elastic twist angles were estimated, based on measured torsion moments and moment/deflection relationships calculated for the first torsional blade mode. Particular effort was devoted to understanding the effects of blade design on 1P

-
13. Niebanck, C. F., MODEL ROTOR TEST DATA FOR VERIFICATION OF BLADE RESPONSE AND ROTOR PERFORMANCE CALCULATIONS, Sikorsky Aircraft Division, United Technologies Corporation, USAAMRDL Technical Report 74-29, Eustis Directorate, U.S. Army Air Mobility Research and Development Laboratory, Fort Eustis, VA, May 1974, AD 786562

torsional response. With the exception of stalled conditions for which stall flutter was present, the first harmonic was the primary torsional response component. Trends of steady and LP elastic twist, with changes in airspeed and rotor lift, were analyzed for propulsive force coefficients corresponding approximately to those of the reference rotor ($f = 25 \text{ ft}^2$). Figure 23 illustrates the variation of steady and LP tip elastic twist with lift coefficient-solidity ratio at an advance ratio equal to 0.3. Principal results are listed below:

1. All blade sets experience an increase in both steady and retreating blade (LP sine) nosedown twisting with increasing lift coefficient.
2. Positive camber introduces significant advancing-blade nosedown twisting.
3. The 3 x stiffness blade experiences approximately one-third the steady and LP torsional response of the baseline.
4. Relative to an untwisted blade, introducing negative built-in twist decreases steady nosedown elastic twist and reduces the amplitude of LP elastic twist.

Similar results were evident from the $\mu = 0.4$ data. The only significant effect of increasing advance ratio from 0.3 to 0.4 at fixed C_L/σ and parasite area was a 30-percent increase in the LP sine component of twist experienced by the cambered blade.

The second phase of the model rotor data analysis examined effects of torsional response on rotor performance, blade stress, and control-system loads. Figure 24 compares the performance characteristics of the four rotors at an advance ratio of 0.3. Results show that relative to the baseline, increasing stiffness degrades performance and increasing negative twist or introducing positive camber improves performance (at least at the low tip Mach numbers of these rotors). The performance effects of twist- and camber-induced torsional response cannot be isolated from the primary aerodynamic effects of the parameters. A direct measure of the effects of torsional response is, however, available from comparisons of configurations 1 and 2, which differ only in blade stiffness. Elastic twist and performance data of Figures 23 and 24 suggest that relative to the 3 x stiffness blade, the baseline blade exhibits a performance advantage by virtue of increased LP sine twisting. Figure 25 presents torque coefficient data from the two rotors as a function of this twist component. At each lift coefficient the effect of increased advancing-blade noseup twist and retreating-blade nosedown twist is favorable. A 15-percent performance benefit is shown at a blade loading of 0.10. This result is in agreement with predictions of the twist required for minimum profile drag torque described earlier.

For the untwisted model blades, it is likely that the performance gain was a result of nosedown retreating-blade twist rather than noseup advancing-blade twist. Increased retreating-blade twist reduces tip stall and profile drag torque by shifting airloads to inboard stations. Increasing advancing-blade noseup twist for the untwisted rotor would be expected to increase profile drag torque requirements. This effect may have been small at model scale advancing tip Mach numbers.

Control load and blade stress data were examined to identify possible effects of elastic twisting. Although the different configurations experienced somewhat different control loads, no direct effects of compliance such as retreating-blade stall avoidance could be definitely established. Figure 26 shows the buildup with lift coefficient of peak-to-peak blade root torsional moment. These data include significant 1P moment components. Figure 27 compares the various rotors in terms of the 4P fixed-system control loads which each would generate. These results are based on resolving 3, 4, and 5P rotating system control loads into 4P swashplate forces and moments. The following observations can be made from Figures 26 and 27:

1. The 3 x stiffness blade generally experienced the highest vibratory loads.
2. The cambered blade resulted in the lowest 4P fixed system loads at high C_L/σ .
3. Control loads of the -8 degree twist and the baseline blade were comparable.

The reduction in high-frequency torsional moments experienced by the baseline blade relative to the 3 x stiffness blade may be the result of avoiding retreating blade outboard stall through 1P twisting. The results of work reported in Reference 6 indicate that some reduction in high-frequency torsional moments is to be expected as a direct result of the reduced torsional stiffness.

The only significant effect of elastic twist on blade stress was the tendency of camber-induced twisting to increase peak-to-peak flatwise stress. Data presented in Figure 28 for an advance ratio of 0.4 show that the advancing-blade nosedown twist of the cambered blade increases tip-down flatwise bending in essentially the same fashion as built-in twist. Although this stress component is not a problem for the untwisted model blades, it suggests that the combination of positive camber and large built-in twist can result in significant flatwise stress.

EXAMINATION OF CH-53D SWEPT-TIP FLIGHT TEST DATA

The second source of test data exhibiting significant effects of elastic twist is the CH-53D flight-test evaluation of swept tips reported in Reference 5. Sweep imparts torsional moments to the blade which are proportional to tip airloads. Therefore, under high-speed conditions, noseup advancing-blade twist and nosedown twist at other azimuths generally result. Data were analyzed to determine the potential effect of this twisting mechanism on compliant rotor behavior. Reference 5 compares test data for three sets of swept-tip blades with that of baseline unswept blades, all flown on the CH-53D aircraft. The five blade configurations analyzed are described below.

1. H-53 blade (-6 degree twist, modified NACA 0011 airfoil).
2. H-53 blade, modified to incorporate a 20-degree aft swept tip at the 95-percent span station, a cambered airfoil outboard of the 88-percent span station and a 2.5-degree increase in negative twist at approximately the 90-percent span station.
3. H-54 blade (-14 degrees twist, modified NACA 0011 airfoil).
4. H-54 blade with the sweep, camber and tip twist modifications of configuration 2.
5. H-54 blade, modified to include the camber and sweep of configurations 2 and 4, but with the standard H-54 twist (-14 degrees).

Analysis of the data shows that in addition to anticipated beneficial effects on performance and noise achieved by relieving advancing blade drag divergence, the swept tip had beneficial aeroelastic effects. Vibratory control-system loads and blade flatwise bending stresses were reduced. A primary source of vibratory flatwise bending moments and blade twisting moments is the tendency for the tip of the advancing blade to bend down, which then causes tip drag loads to create a large nosedown twisting moment. By causing the negative lift at the tip of the advancing blade to act behind the elastic axis of the inboard blade sections, the swept tip serves to relieve the nosedown twisting moment. To the degree that this reduction in twisting moment untwists the advancing blade, downloading at the tip is reduced, and the flatwise moment is reduced.

The most significant reduction in twisting moment was accomplished with the low-twist swept tip on the H-54 blade (configuration 5). Figures 29 and 30 compare baseline and swept-tip pushrod load time histories for the low- and high-twist blades at a 150-knot, 42,000-lb-lift flight condition. Examination of these data suggest the following conclusions:

1. High twist aggravates advancing-blade nosedown twisting moments (Figures 29(a) and 30(a)).
2. Adding tip sweep without increasing tip twist was effective in reducing advancing blade nosedown moment (Figures 30(a) and 30(c)).

3. Relative to baseline blades, configurations 2 and 4 did not significantly reduce control loads (Figures 29(a) and (b) and 30(a) and (b)). This was probably because the advancing-blade nosedown moment introduced by the increased tip twist and tip positive camber approximately cancelled the noseup moment introduced by the swept tip.
4. On the H-54 blade, the combination of swept tips and a cambered airfoil outboard of the 88-percent radius position caused a significant reduction in the high-frequency pushrod loads usually attributed to stall flutter. This effect was most significant for the low-twist-swept tip (configuration 5), (Figures 30(a), (b), (c)). Unfortunately, it is not clear whether this improvement results from avoiding stall through compliant twisting of the retreating blade, or from improved dynamic stall characteristics of the SC 1095 relative to the baseline NACA 0011 airfoil.

The effect of sweep-induced twist on flatwise stress was examined. The addition of low-twist swept tips caused sizable reductions in flatwise stress (configuration 5 versus configuration 3). Highly twisted swept tips (configurations 2 and 4) resulted in smaller stress reduction. In these cases, the increase in built-in tip twist and the addition of positive tip camber tend to oppose the reduction in advancing blade twist induced by the tip sweep. Figure 31 compares the buildup with airspeed of flatwise stress at critical blade stations for the three high-twist H-54 blades. 15- to 20-percent stress reductions are achieved with the swept low-twist tip. Further stress reductions were probably not achieved because the high torsion stiffness of the H-54 blades permits only a small elastic untwisting of the advancing blade. Tip region angles of attack, tip download, and advancing blade bending moment are, therefore, not significantly changed. Reduced torsion stiffness would be expected to improve this aspect of swept-tip behavior.

Unfortunately, swept-tip rotor forward flight performance data could not be analyzed because of intermittent malfunctions of the rotor torque measuring system. Two favorable effects of tip sweep on performance are anticipated. First, the swept tip relieves advancing-blade drag divergence penalties. Second, for a blade of sufficiently reduced torsional stiffness, sweeping the tip sets up a feedback mechanism which drives tip angles of attack towards zero. The need for a mechanism which drives advancing blade angles of attack to zero and increases retreating-blade twist was evident from the calculations of ideal rotor angle of attack discussed earlier.

The capability of the Normal Modes Blade Aeroelastic Analysis for modeling the effects of tip sweep was examined by correlating test and analytic results for two CH-53D flight conditions. The correlation of control-load and blade-stress data was examined for standard H-54 blades and for low-twist swept-tip H-54 blades which successfully reduced control

loads and blade stress (configurations 3 and 5). In general, the trends of the test data were reliably predicted. Figures 32 and 33 illustrate measured and calculated effects of tip sweep on time histories of pushrod load and flatwise stress. Test and analytic data are shown on separate plots to illustrate the trends resulting from the addition of tip sweep. Pushrod load data shown in Figure 32 demonstrate that the analysis predicts the tendency of sweep to reduce both LP and high frequency torsional response. Peak-to-peak loads are slightly underpredicted for each blade. Blade flatwise stress results shown in Figure 33 indicate that approximately correct percentage reductions in blade stress resulting from sweep are predicted with the blade response analysis. The magnitude of the tip-down bending in the area of $\psi = 180$ degrees is overpredicted for both blades. This may be the result of not including three-dimensional flow effects in the calculation of airloads. The buildup with airspeed of pushrod loads and blade stress is presented in Figure 34. Again, the trends shown by the test data are accurately described. The predicted effect of tip sweep on required power was a savings of approximately 5 percent relative to the unswept baseline blade (configuration 3) at the 150-knot, 42,000-lb flight condition. This performance improvement resulted primarily from increased retreating blade twist which served to avoid stall.

EVALUATION OF COMPLIANT ROTOR DESIGN PARAMETERS

The capability of blade design parameters for producing elastic twist which improves performance and reduces flight loads was examined with the Normal Modes Blade Aeroelastic Analysis. Parametric variations to reference rotor blade properties were investigated at two flight conditions in the vicinity of the stall boundary and in hover at $C_T/\sigma = 0.10$. The two forward-flight conditions were $\mu = 0.3$ and $C_L/\sigma = 0.10$, which corresponds to 130 knots and 23,230 lb of lift, and $\mu = 0.4$ and $C_L/\sigma = 0.085$, which corresponds to 172 knots and 19,750 lb of lift. This set of flight conditions was considered to ensure that compliant design candidates were effective over a realistic operating range. The primary emphasis was on achieving elastic twist similar to that prescribed earlier for maximum L/Q_D . In order to increase the reliability of control-load and blade-stress predictions, unsteady aerodynamics and nonuniform inflow were used throughout. It was recognized that the optimal twist and the magnitude of the performance benefits predicted with GRP and steady aerodynamics would not necessarily be optimal, assuming unsteady aerodynamics. The basic trends were expected to apply. Reductions in the blade stress, control loads and vibratory hub forces of the baseline rotor were also sought. The parametric data were used in the final selection of compliant rotor designs described in the last section of the report.

Rotors incorporating each of the parametric changes were trimmed to the lift, propulsive force, and head moments of the reference rotor. As noted above, nonuniform inflow was used consistently. In evaluating a blade design change, iteration between the blade response and inflow analyses was found to be essential. Blade design changes were first analyzed, assuming the inflow distribution of the baseline rotor. The inflow was then recalculated with the Prescribed Wake Inflow Analysis based on predicted control angles, flapping, and torsional response. Then the blade response analysis was repeated using the corrected inflow. Experience indicated that first-pass results (compliant design in baseline rotor inflow) could give incorrect performance and rotor-load trends when baseline and compliant rotors exhibited significantly different torsional response.

The following set of parameters was addressed:

1. Tip sweep
2. Camber
3. Blade chordwise aerodynamic center, elastic axis, and center-of-gravity position
4. Torsional stiffness
5. Twist
6. Tip taper
7. Root kinematic coupling

Properties were changed singly and in combination. Variations in the magnitudes and radial distributions of the parameters were examined. In order to reduce the number of design cases to a manageable level, exploratory studies were first conducted which identified the most significant effects and defined the potential role of each of the parameters in contributing to ideal torsional response. Results indicated that the parameters listed above could be divided into those which are sources of loading, those which modulate the magnitude of the steady and time-varying twist, and those which have no significant effect on compliant response. Tip sweep, camber, and offset of the aerodynamic center from the elastic axis were found to be the most powerful sources of compliant loading. Torsional stiffness governed the magnitude and radial distribution of elastic response. The primary role of built-in twist was to permit adjustments to the steady elastic twist which resulted from compliant loading. Exploratory calculations showed that for the flight conditions examined, tip taper and root kinematic coupling offered little benefit in terms of reduced flight loads or improved performance. Further detailed analysis of these two parameters was not conducted. The process of selecting compliant rotor torsional stiffness is discussed below, followed by examination of compliant designs based on each of the three loading mechanisms--camber, tip sweep, and offset of blade lift and elastic axes.

TORSIONAL STIFFNESS

It was evident from the analysis of model and full-scale rotor elastic twist data that reduced torsional stiffness is required to achieve the full benefits of compliance. Rather than analyze variations of the other parameters holding the torsional stiffness of the baseline, levels of stiffness reduction which facilitate achieving ideal rotor twisting were first estimated. Variations to the other blade parameters were then made, assuming reduced torsional stiffness. The amount of stiffness reduction required to achieve specified response amplitudes depends on the strength of the compliant loading. Large lift offset or camber, for example, can induce significant response even on a stiff blade, and vice versa. The approach adopted in the present study was to apply significant compliant loading to a blade of moderately reduced torsional stiffness. The alternative of using a weaker loading mechanism and a very soft blade has potentially undesirable side effects, such as coupling of torsion and first flatwise bending modes, proximity of the torsion mode to 2P and 3P resonances, and increased susceptibility to the track and balance problems which result from blade-to-blade differences in airfoil contour. A realistic estimate of the flexibility needed for ideal performance twisting was made assuming a typical loading mechanism, a 20-degree swept tip at the 90-percent span station. This loading mechanism was used in estimating flexibility requirements because it is effective in producing the 1P lateral component of tip twist found to be necessary for maximum L/Q_D . Figure 35 compares the lateral component of elastic twist for blades of varying torsional stiffness with the ideal rotor requirement at an advance ratio of 0.4 and C_L/σ equal to 0.085. Results show that decreasing outboard blade stiffness (GJ) by a factor of five and increasing root

torsional stiffness (K_θ) results in elastic deflection of approximately correct amplitude. Varying the radial extent of the softened section for a given applied loading can be used to achieve better agreement between actual and desired twisting at specified spanwise locations. Stiffness reductions of four or five to one over the outer 20, 40, and 50 percent of blade span are used in the following design cases as indicated.

CAMBER

Camber is a parameter having a very powerful effect on torsional response. The baseline rotor employs an SC 1095 airfoil for which the below-stall pitching moment coefficient, c_{m_0} , is $-.025$. The effects of varying this coefficient from $-.025$ to $+.03$ were examined by shifting the SC 1095 pitching-moment data by a uniform amount, independent of angle of attack and Mach number. Airfoil lift and drag data were assumed unchanged. This airfoil representation may be somewhat unrealistic, but it allows identification of the significant effects of camber without requiring a detailed airfoil design study. For an unstalled condition, magnitudes of local pitching moments induced by camber follow dynamic pressure. As a result, there are strong steady and LP moments and secondary amounts of $2P$ moment. The LP moment can be such as to twist advancing blades noseup or nosedown, depending upon the sign of c_{m_0} . Based on performance gains and blade-stress reductions anticipated for noseup advancing-blade twist, positive values of c_{m_0} were extensively studied. It should also be noted that the increase with airspeed of the LP lateral twist prescribed for maintaining maximum L/Q_D (Figure 21) is compatible with a fixed positive value of c_{m_0} .

Various magnitudes and radial distributions of c_{m_0} were examined for combinations of torsion stiffness and built-in twist. In general, negative camber ($+c_{m_0}$) had a strongly beneficial effect on flatwise stress but a detrimental effect on performance. The results of a representative noseup pitching moment case are shown in Figures 36 through 40. Figures 36 through 38 present surface plots of torsional response, angle of attack, and airload distribution. Distributions are shown at an advance ratio of 0.4 and C_L/σ equal to 0.085 for the baseline rotor and for a rotor employing $c_{m_0} = +.03$ over the entire blade. This large positive value of c_{m_0} is studied to indicate the trends of performance and rotor loads with camber. Achieving such a large effective camber would require substantial trailing-edge tabs which would, of course, have significant effects on airfoil lift and drag. The compliant design has the built-in twist of the baseline rotor (-12 degrees) and a torsional stiffness which, relative to the baseline, is reduced by a factor of five outboard of the 60-percent span station. In this case, the elastic twist induced by a positive c_{m_0} includes a significant steady component ($+4.1^\circ$) and a large LP component (7.3°), phased to increase advancing-blade pitch. Higher harmonic responses which are also present result from stall on the retreating blade and

transonic flow effects which create positive c_m in the first quadrant. Comparison of the surface plots of angle of attack (Figure 37) and airload (Figure 38) show that positive c_{m_0} in combination with reduced torsional stiffness has the general effect of shifting loading outboard. Four specific observations can be made:

1. Advancing-blade lift is carried on outboard sections of the blade.
2. Negative tip lift in the second quadrant is eliminated.
3. Retreating-blade tip angle of attack and loading are increased.
4. Significant lift is carried in the region $\psi = 340$ degrees to $\psi = 60$ degrees as a result of local noseup elastic twist.

The effect of this redistribution of loading on performance is illustrated in Figure 39. Azimuthal contributions to blade torque for baseline and positive c_{m_0} blades are compared. Torque is broken into a contribution resulting from blade element profile drag and a contribution resulting from blade element lift (induced drag and parasite drag). This breakdown identifies the success with which profile drag torque is driven to the minimum through ideal twisting. As shown in Figure 39(a), large increases in drag torque are experienced by the positive c_{m_0} blade. Reference to Figure 36(a) indicates that these losses result primarily from the higher harmonics of elastic twist induced by negative camber. Noseup torsional oscillations induced by retreating-blade stall result in large torque penalties ($\psi = 240$ degrees, 300 degrees, and 20 degrees). Contributing to the retreating-blade stall is the fact that with negative camber the net hub moment resulting from blade-root pitching moments is positive (aircraft noseup). This moment must be balanced by increasing airloading over the aft portion of the rotor disc. In this case, the required increase in fourth-quadrant loading drives the rotor into stall. In this case ($c_{m_0} = +.03$), advancing-blade drag torque is also increased slightly as a result of excessive advancing-blade noseup twist, which places advancing-blade tip angles of attack above the minimum drag angle. For smaller amounts of negative camber and LP twist, advancing-blade torque savings were achieved but the effect on total drag torque was still unfavorable. The effect of camber on the sum of induced and parasite torque is shown in Figure 39(b). Penalties are indicated at the azimuth positions where additional lift results from noseup twisting. Second-quadrant power savings apparently result from induced power savings achieved by carrying lift at outboard blade stations where inflow angles are smaller.

The redistribution of airloads shown above had a very favorable effect on blade flatwise stress as illustrated in Figure 40. Second-quadrant airloads for the baseline rotor are positive out to approximately 90-percent radius, and negative at the tip. This distribution excites a large response of the first blade bending mode. The positive c_{m_0} blade

reduces inboard uploading and eliminates tip downloading. As a result, second-quadrant bending moments are significantly reduced. In this case, peak-to-peak bending moments were reduced by 45 percent.

Figure 41 presents the variation of blade vibratory stress and power for a range of c_{m_0} at the $\mu = 0.4$, $C_L/\sigma = 0.085$ flight condition. Data are shown for the reference rotor and for a rotor blade having one-fifth the torsional stiffness of the reference rotor outboard of the 60-percent radial station. Figure 41(a) shows that the independent effect of reducing torsional stiffness while holding the SC 1095 camber is to increase stress. The independent effect of increasing c_{m_0} is to reduce stress. Power data are shown in Figure 41(b). Increases in c_{m_0} for the reduced stiffness blade first improve and then degrade performance. Although amplitudes of 1P lateral twisting approximately equal to those prescribed for maximum L/Q_D are achieved for c_{m_0} in the range from +.015 to +.03, total power is not reduced below that of the baseline blade for two reasons: first, undesirable higher harmonics of pitch response are excited; second, the introduction of positive pitching moment reduces the magnitude of the steady negative twist. In order to create a closer match between actual and ideal steady twist, increases in built-in twist were explored for positive c_{m_0} blades. Results shown in Figure 42(a) indicate that increasing built-in twist does reduce power requirements, although not below that of the baseline. The inevitable effect of increased built-in twist is to increase maximum blade stress (Figure 42(b)).

TIP SWEEP

CH-53D test data analyzed earlier indicated the potential of tip sweep for reducing both blade stress and control loads. A favorable effect of sweep on performance was also predicted with the Normal Modes Blade Aeroelastic Response Analysis. The elastic twist induced by tip sweep is proportional to tip airload. As such, a steady nosedown twist and a 1P twist which tends to be noseup on the advancing blade and nose-down on the retreating blade are the primary characteristics of the response. Tip sweep on a blade of sufficiently reduced torsional stiffness can be expected to act as a feedback mechanism which drives advancing-blade tip loading, angle of attack, and drag to minimum values.

The first area of interest in examining sweep was to define the optimal combination of the angle and spanwise position of the sweep. Both the CH-53D and YUH-60A blades employ 20 degrees of sweep at the 95-percent radius position. Reference 6 reports on tests of a compliant model rotor which had 10 degrees of tip sweep starting at the 65-percent span station. Analysis was conducted at an advance ratio of 0.4 and C_L/σ equal to 0.085 for blades having 10 and 20 degrees of sweep at the 90-percent station, and for blades having 10 degrees of sweep at 80- and 70-percent radius. A blade employing the baseline twist distribution and a torsional stiffness reduced by a factor of five outboard of 60-percent radial position was considered. Tip region chordwise center of gravity was assumed to be

maintained at the elastic axis. Effects of varying the angle of sweep at the 90-percent radius position are shown in Figure 43. Increasing sweep has favorable effects on performance, maximum blade stress and vibratory pushrod load. A slightly adverse effect on 4P hub moments is indicated by an increase in 3P rotating system vertical shear forces. Corresponding effects of varying the position at which the sweep begins for a fixed sweep angle are shown in Figure 44. Moving the sweep coordinate inboard from 90- to 80-percent radius has a slightly beneficial effect on performance, but adverse effects on blade stress, control loads, and vibration. Converged results could not be obtained for blades having 10 degrees of sweep at 70-percent radius. Extremely large retreating-blade negative twisting prevented the achievement of a trimmed condition with this design. Based on these data, a 20-degree swept tip at the 0.9R station is the most promising candidate.

The means by which tip sweep relieves power requirements is illustrated in Figures 45 and 46. Figure 45 compares contributions to drag torque for the straight and 20-degree swept-tip blades shown in Figure 43. The unswept blade suffers significant advancing blade drag torque penalties. It should be pointed out that the version of the Normal Modes Blade Aeroelastic Response Analysis being used does not account for the relieving effect of sweep on drag divergence. Drag torque reductions shown in Figure 45(a) are, therefore, a direct result of compliance. In Figure 46, advancing-blade angles of attack for the two cases are compared with the angle of attack for which c_d exceeds its minimum value at the local Mach number by 10 percent. By virtue of decreased twist, the swept-tip blade achieves angles of attack which maintain drag within 10 percent of the minimum.

A number of combinations of built-in twist and radial stiffness distribution were examined for blades with 20 degrees of tip sweep at 90-percent radius. The analysis was conducted at $\mu = 0.3$ and $C_L/\sigma = 0.10$, and $\mu = 0.4$ and $C_L/\sigma = 0.085$. Performance was generally improved over that of the reference rotor. Rotor equivalent drag was reduced by from 2 to 7 percent. Baseline rotor pushrod loads were reduced by as much as 50 percent, primarily as a result of reducing 1P components. Small reductions in blade stress (less than 10 percent) were generally predicted. Figures 47 through 49 illustrate the effects of tip sweep on rotor loading and blade response. The swept-tip compliant design shown, which includes -9 degrees of twist, a four-to-one stiffness reduction outboard of 50-percent radius and an SC 1095 airfoil, offered a 7-percent reduction in rotor equivalent drag (100 horsepower) at this flight condition ($\mu = 0.4$ and $C_L/\sigma = 0.085$). Figures 47 and 48 present surface plots of aerodynamic pitching moment and blade torsional response for the swept-tip design. The torsional response distribution includes a steady nosedown twist and a 1P component which reduces advancing-blade twist and increases retreating-blade twist. Unlike the elastic twist resulting from negative camber (Figure 36), the twist induced by sweep is free of higher harmonic responses. The performance saving resulted from a close match between actual and maximum L/Q_D twist. Although the swept tip tends to reduce second-quadrant

tip downloads (Figure 49), this causes only a small reduction in the excitation of first flatwise mode bending in the second quadrant. Unlike negative camber for which positive second-quadrant elastic twist shifted airloads to the tip and reduced first-mode bending (Figures 36-39), tip sweep achieved only a small reduction in twist relative to the reference rotor. As a result, peak-to-peak flatwise stresses were only reduced by 10 percent.

CHORDWISE LOCATION OF BLADE ELASTIC AXIS AND AERODYNAMIC CENTER

Variations in the relative chordwise positions of aerodynamic center, mass and elastic axes were examined. The blade response analysis treats arbitrary spanwise distributions of center-of-gravity and aerodynamic center position. The blade elastic axis is assumed to be straight and coincident with the pitch axis. Reference 8 describes earlier study of the effects of axis placement on performance and blade loads. Results of that work showed that offset of the aerodynamic center from coincident elastic and mass axes has strong effects on torsional response. A 5 percent of chord aft shift of the aerodynamic center caused a 1P lateral twisting, which was predicted to improve the performance and reduce the high-frequency control loads of the CH-53A. No beneficial effects of mass offset on performance or rotor loads were found. Similar uniform spanwise offsets of blade axes were considered for reduced torsional stiffness compliant rotor designs. No significant performance or rotor-load benefits were found. Inability to improve performance resulted in part from not concentrating twisting in the tip region, as prescribed for minimum-drag torque.

Twisting moments induced by lift offset from the elastic axis are proportional to local lift. Tip airloads are primarily 1P. Inboard blade positions, however, experience substantial 2P airload components as shown in Figure 50 which presents reference rotor airload time histories at two flight conditions. The possibility of using these airloads to induce favorable 2P elastic twisting was examined. This effort represents a departure from the previous studies, in which the goal has been to match the radial distribution of 1P twist prescribed to minimize the drag torque of a rotor having the azimuthal distribution of lift calculated for the reference rotor. The potential performance benefits of applying 2P cyclic pitch at the blade root have been demonstrated by a number of analytical and experimental programs (References 3, 4, 6 and 11). The study of 2P elastic pitch began by running the blade response analysis with the torsional degree of freedom replaced by a specified distribution of torsional response. Elastic pitching distributed radially in proportion to the torsional mode shape and azimuthally at a frequency of 2P was prescribed in the analysis. Various amplitudes and phases of tip 2P twisting were studied. In each case, induced velocity distributions were recalculated to ensure accurate modeling of induced power effects. Results showed that at 172 knots and 19,750 lb of lift, 2 degrees of 2P elastic pitch phased to increase over the nose and tail ($\theta_{tip} = 2^\circ \cos 2\psi$) gave a performance

benefit of 8 percent. Reductions in rotor equivalent drag of approximately 12 percent were predicted at 130 knots and 23,230 lb of lift, with approximately 1 degree of 2P tip twist. The midspan airloads shown in Figure 50 are approximately in phase with this elastic twist. The aerodynamic center must, therefore, be placed ahead of the elastic axis in this span range in order to achieve the desired twisting. Designs were considered which employ aerodynamic centers 10, 15, and 20 percent of the chord forward of the elastic axis for portions of the region between 50- and 90-percent radius. Without tip sweep, the forward aerodynamic center blades were subject to an instability involving coupling of blade torsion and flatwise bending. Addition of a 20-degree swept tip at the 90-percent radius station precluded any unstable response. 2P torsional response was enhanced by decreasing torsional stiffness outboard of 50-percent radius and reducing control-system stiffness. The uncoupled torsion mode frequency was 3.5P. A design employing further stiffness reductions which placed the torsional frequency at 2.5P was considered briefly, in an attempt to amplify 2P response. In this case, however, large-amplitude 1P and 2P responses made it difficult to achieve trimmed analytic solutions.

Figures 51 and 52 illustrate the airloads and response of blades having the aerodynamic center 15 percent of the chord forward of the elastic axis, from 60- to 80-percent radius. The elastic twist achieved by this design is compared in Figure 51(a) to that of a blade having the same stiffness and tip sweep but without the forward aerodynamic center. The difference between the two curves (Figure 51(b)) shows the effectiveness of the forward aerodynamic center in producing 2P response. The airload distributions of the forward aerodynamic center and swept-tip blades are compared in Figure 52. Increases in loading over the front of the disc are balanced as far as rotor pitching moment by increases at $\psi = 340$ degrees and $\psi = 40$ degrees. Lift is decreased abruptly in the azimuth range from 60 to 120 degrees and gradually on the retreating side of the disc. Rotor equivalent drag was reduced by approximately 5 percent in this case. As a result of increasing outboard airloads in the second quadrant flatwise stress was reduced by approximately 20 percent relative to the baseline rotor. Vibratory control loads were increased by 10 percent as a result of noseup advancing-blade twisting moments produced by negative tip lift. Some reduction in these lift-induced control loads could be achieved in designing a compliant rotor blade, by moving the local elastic axis aft of the aerodynamic center and pitch axis, rather than moving the aerodynamic center forward. In this way, local beneficial twisting could be induced without having large offsets of the lift and feathering axes. The version of the normal modes analysis being used does not model offset of feathering and elastic axes. 4P vertical shear forces and hub moments were increased by from 10 to 80 percent as a result of the increases in 3, 4 and 5P airload components which result from the increase in oscillatory blade pitching motion. The attributes of blades having midspan aerodynamic centers forward of the elastic axis will be described further in the following section which selects two optimal compliant rotor designs based on the parametric data generated to this point, and evaluates flight characteristics in hover and throughout the forward-flight envelope.

SELECTION OF OPTIMAL COMPLIANT ROTOR DESIGNS

Compliant designs based on three loading mechanisms--camber, tip sweep, and midspan aerodynamic center-elastic axis offset--have been explored. Torsional stiffness and twist distributions compatible with each design have been established. The remaining task is to explore combinations of the primary parameters which yield greatest overall performance benefits and load reductions. Two optimal compliant designs are to be selected which are suitable for wind tunnel verification testing. The procedure used to select optimal designs was first to calculate blade loads and performance for combinations of the independent parameters (tip sweep and camber, for example). Second, a penalty function involving a weighted combination of the various load and performance indices was used to evaluate the candidate designs. The primary emphasis was on performance improvement and load reduction in forward flight. Hover performance of design candidates was also determined and evaluated in selecting final designs.

Two parameters which offer complementary benefits are camber and tip sweep. Parametric data showed that negative camber reduced stress and tip sweep improved performance. The combination of the two which produces the greatest overall benefits was sought. Nine combinations of sweep angle at the 90-percent radius and below stall pitching moment coefficient, c_{m_0} , were examined at an advance ratio of 0.4 and blade loading equal to 0.085. c_{m_0} values of $-.025$, $+.015$, and $+.03$ and sweep angles of 0, 10, and 20 degrees were considered. A blade having one-fifth the torsional stiffness of the baseline outboard of the 60-percent radius was assumed. Significant results are shown in Figures 53 through 55. The effects of sweep and camber on power, maximum flatwise stress, vibratory pushrod load, average 4P servo load, and 3P rotating vertical shear force are illustrated using three-dimensional surface plots. These response surfaces were generated by performing a polynomial curve fit to the nine data points and evaluating the polynomial at evenly spaced grid points. The following observations can be made:

1. The effects of sweep and camber on power are nonlinear; increasing sweep is favorable for $c_{m_0} = -.025$ and $+.03$ but unfavorable for intermediate c_{m_0} .
2. Positive camber does not achieve as large a reduction in stress on the swept blades as it does on the unswept blades.
3. Vibratory pushrod loads tend to be reduced by tip sweep and/or positive camber.
4. Average 4P servo load is reduced by increasing positive camber. The minimum occurs with 20 degrees of tip sweep and the SC 1095 airfoil.
5. Minimum 3P rotating system vertical shears are achieved with unswept positive camber blades.

In view of the somewhat conflicting effects of sweep and camber on power, stress, control loads, and vibration, it is clear that the selection of an optimal configuration depends entirely on the relative importance of the various loads. Specific mission requirements would dictate the most crucial factors and the optimal design. The relative merits of the possible designs were explored by evaluating penalty functions made up of weighted sums of the five loads shown above. A number of weighting coefficient sets were used. Variations of three typical penalty functions are illustrated in Figure 56. The penalty function weighting coefficients and the equivalent amounts of the five loads are indicated. Penalty functions are normalized to a minimum value of 1.0. The function shown in Figure 56(a) places equal weight on reducing each of the loads by the maximum amount shown to be possible in the parametric studies. In this case, the minimum of the penalty function occurs for a blade with 20 degrees of tip sweep and c_{m_0} equal to -.025. The second penalty function (Figure 56(b)) assumes that blade and control-system loads are below endurance levels and minimizes power and vibratory hub force. Again, a positive camber swept-tip blade is one of the optimal solutions. Only when a very heavy weighting is placed on stress, such as in Figure 56(c), does a blade with negative camber become the design solution. Based on these indications a blade with an SC 1095 airfoil and 20 degrees of tip sweep was selected. Final iterations on the radial distribution of torsional stiffness and on built-in twist yielded a design with one-fourth the torsional stiffness of the baseline outboard of 50-percent radius and -9 degrees of twist. Figure 57 illustrates the planform, stiffness, and twist distributions of this first compliant rotor. Figure 58 compares the performance and rotor loads of this compliant design with those of the baseline rotor for a range of operating conditions. Required power is reduced by 100 hp at the $\mu = 0.4$ and $C_L/\sigma = 0.085$ condition, and by 200 hp at the $\mu = 0.3$ and $C_L/\sigma = 0.115$ condition but is not reduced at the two other conditions shown. Favorable effects on stress and control loads are shown. Vibratory hub moments are reduced at a μ of 0.3, but increased at a μ of 0.4. The impact of this design on the flight limits of the reference rotor (Figure 4) was also examined. Figure 59 shows that the operating limits based on power, stress, and control loads are expanded with the swept-tip compliant design.

The second compliant design selected was one which improved performance by producing 2P elastic pitching. A number of design cases were considered, which varied the tip sweep and camber of a blade having its midspan aerodynamic center forward of its elastic axis. Twenty degrees of tip sweep at 90-percent radius were required for stability. Application of negative camber tended to reduce blade stress but degrade performance. A final design was chosen which has the twist and stiffness distributions of the swept-tip design described above and an aerodynamic center 15 percent of the baseline chord ahead of the elastic axis from 63- to 86-percent radius. The characteristics of this design are included in Figure 57. Figure 60 illustrates the effect of the offset airloading on performance and loads. Significant power savings are predicted at $\mu = 0.3$, especially at $C_L/\sigma = 0.115$, at which the baseline rotor is stalled. Stresses are generally reduced more with this design than with design #1.

Pushrod loads, however, are not significantly reduced and vibratory 3P root shears are substantially increased at the 0.4 advance ratio. The increased shear forces result from increases in 3P airloads induced by 2P and 3P blade pitching. The effects of these trends on absolute flight limits are shown for design #2 in Figure 61. Power and stress boundaries are expanded; the boundary determined by vibration is contracted. Whether or not the vibratory hub loads present a significant boundary is entirely dependent on airframe design and vibration control devices.

The final measure of compliant rotor forward-flight behavior to be examined was noise. The rotor noise prediction program was used to calculate PNL for the compliant rotors performing a 250-ft altitude flyover at $\mu = .4$ and $C_L/\sigma = 0.085$ (172 knots and 19,750 lb of lift). As shown in Figure 62, both compliant designs are quieter than the baseline in the far field (2000-to-500-ft separation). During this portion of the approach, the observer is approximately in the plane of the rotor, and perceived noise levels are dominated by advancing-blade impulsive noise. The compliant rotors achieve noise reductions partially as a result of unloading advancing blades through compliant twisting and partially as a direct result of the effect of sweep on drag. Overhead, compliant rotor design #2 is louder than the baseline. In this case, the PNL is dominated by broadband noise which is sensitive to blade twist. At this flight condition, the mean twist (built-in plus average elastic twist) of this design is less than that of the baseline.

Hover performance of the two compliant designs was compared to that of the reference rotor. One of the goals of the compliant rotor is to achieve improved hover performance by increasing twist through elastic windup rather than by increasing built-in twist which introduces large bending moments in forward flight. Figure 63 presents the trend of hover figure of merit with linear twist angle at $C_T/\sigma = 0.1$. The figures of merit and equivalent linear twist values of the reference rotor and the two compliant rotors are also shown. The baseline rotor has a built-in twist of -12 degrees, and the compliant designs employ approximately -9 degrees of twist. As shown, the elastic windup of the torsionally soft swept-tip blades allows them to achieve approximately peak theoretical figure of merit values.

CONCLUSIONS

1. Optimization analysis shows that torsional response which reduces advancing-blade twist improves performance by minimizing profile drag torque.
 - Results based on uniform inflow and steady aerodynamics indicate that relative to a noncompliant baseline, 10- to 20-percent improvements in rotor L/D can be achieved with from 4 to 7 degrees of 1P elastic twisting.
 - The effect of including an unsteady aerodynamic model in the calculation of performance is to improve performance of the baseline rotor and thereby cut the predicted benefits available through compliance approximately in half.
2. Model and full-scale test data show beneficial effects of 1P lateral twisting, which decreases advancing blade twist and increases retreating blade twist.
 - 9-foot diameter model tests of conventional stiffness blades show 15-percent reductions in power required with 2 degrees of lateral elastic twisting.
 - Test data for model blades of differing torsional stiffnesses and for full-scale swept-tip blades show that increasing retreating-blade twist reduces vibratory control loads.
 - Swept-tip blade flight test data shows that 15- to 20-percent reductions in blade stress result from decreasing advancing-blade twist.
 - The beneficial effects of tip sweep on control loads and blade stress are reliably predicted by the Normal Modes Blade Aeroelastic Analysis.
3. Negative airfoil camber effectively reduces blade flatwise bending moments, but generally degrades performance. The performance penalty results primarily from inducing 2P and 3P elastic twisting of undesirable phase.
4. Tip sweep applied to a blade of reduced outboard torsional stiffness achieves improved performance by virtue of a redistribution of airloads, which reduces advancing-blade profile drag torque and retreating-blade induced drag torque. The magnitude of the power savings is approximately two-thirds of that predicted for an ideal rotor achieving minimum profile drag torque. Large reductions in control loads (as much as 50-percent reductions in vibratory pushrod load) and modest reductions in blade stress (less than 10 percent) are accomplished with tip sweep.

5. Placement of the blade aerodynamic center forward of the elastic axis in the span range from 60- to 90-percent radius, in combination with tip sweep required for stability, produces 2P elastic pitching which improves performance. Vibratory hub forces are generally increased by the introduction of this higher harmonic pitching.
6. Swept-tip compliant rotor designs which improve forward flight performance and reduce flatwise stress also improve hover performance by inducing large elastic windup. Approximately 20 degrees of elastic windup results in figure of merit values of 0.76 at a blade loading of 0.1.

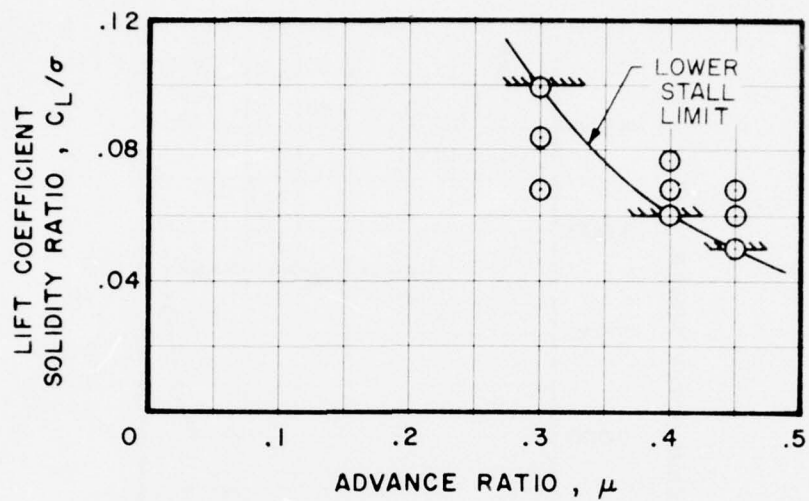
RECOMMENDATIONS

1. The analysis of compliant rotor design parameters conducted herein should be expanded to include additional key parameters such as tip speed, airfoil, radius, and tip geometry. In particular, the effectiveness of using compliance to increase the lifting capability of reduced tip speed rotors should be examined. The potential performance and acoustic benefits of these designs should be quantified.
2. Model tests should be conducted to substantiate the trends predicted for reduced torsional stiffness blades employing tip sweep and noncoincident aerodynamic center and elastic axes in the mid-span region. Model results will also provide data useful in evaluating the adequacy of existing response and performance analyses for predicting compliant rotor behavior.
3. An analysis should be conducted to define the effectiveness of a compliant rotor in satisfying the requirements of a specific Army mission. An analysis of risk areas such as maneuvering flight, handling qualities, sensitivity to blade-to-blade differences (manufacturing differences as well as field damage), and blade combat damage tolerance should be included. The economic trade-offs between compliant and conventional rotors in terms of manufacturing and operating cost should be evaluated.
4. The present airload optimization analysis which prescribes twisting for minimum-profile drag torque based on steady aerodynamics should be expanded to include the effects of induced drag and unsteady aerodynamics.

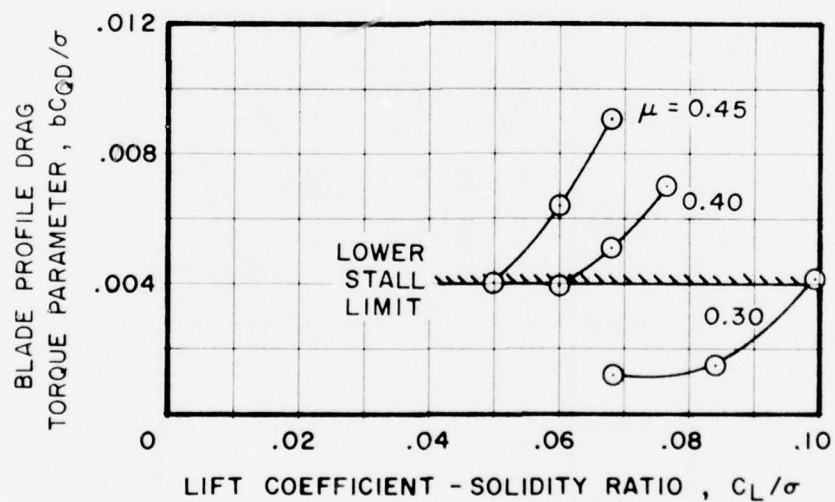
REFERENCES

1. Lemnios, A. Z., et al., FULL SCALE WIND TUNNEL TESTS OF A CONTROL-
LABLE TWIST ROTOR, American Helicopter Society, 32nd Annual National
Forum, May 1976
2. McCloud, J. L., and Kretz, M., MULTICYCLIC JET FLAP CONTROL FOR
ALLEVIATION OF HELICOPTER BLADE STRESSES AND FUSELAGE VIBRATION,
American Helicopter Society, Specialists Meeting on Rotorcraft Dynamics,
February 1974
3. McHugh F. H., and Shaw, J., BENEFITS OF HIGHER HARMONIC BLADE PITCH:
VIBRATION REDUCTION, BLADE LOAD REDUCTION, AND PERFORMANCE IMPROVE-
MENT, American Helicopter Society, Symposium on Rotor Technology,
August 1976
4. Balcerak, J. C. and Erickson, J. C., SUPPRESSION OF TRANSMITTED
HARMONIC VERTICAL AND INPLANE ROTOR LOADS BY BLADE PITCH CONTROL,
Cornell Aeronautical Laboratory; USAAVLABS Technical Report 69-39,
U.S. Army Aviation Materiel Laboratories, Fort Eustis, Virginia, July
1969, AD 860352
5. Prillwitz, R., STRUCTURAL EVALUATION OF HIGH PERFORMANCE ROTOR BLADE
SWEPT TIPS, Engineering Report SER-651073, Sikorsky Aircraft Division,
United Technologies Corporation, October 1972
6. Doman, G. S., et al., INVESTIGATION OF AEROELASTICALLY ADAPTIVE ROTOR
SYSTEMS, American Helicopter Society, Symposium on Rotor Technology,
August 1976
7. Tanner, W. H., CHARTS FOR ESTIMATING ROTARY WING PERFORMANCE IN HOVER
AND HIGH FORWARD SPEEDS, Engineering Report SER-50379, Sikorsky
Aircraft Division, United Technologies Corporation, August 1964
8. Blackwell, R. H., and Commerford, G. L., INVESTIGATION OF THE EFFECTS
OF BLADE STRUCTURAL DESIGN PARAMETERS ON HELICOPTER STALL BOUNDARIES,
Sikorsky Aircraft Division, United Technologies Corporation; USAAMRDL
Technical Report 74-25, Eustis Directorate, U.S. Army Air Mobility
Research and Development Laboratory, Fort Eustis, VA, May 1974, AD
784594
9. Arcidiacono, P. J., et al., INVESTIGATION OF HELICOPTER CONTROL LOADS
INDUCED BY STALL FLUTTER, Sikorsky Aircraft Division, United Technol-
ogies Corporation; USAAVLABS Technical Report 70-2, U.S. Army Avia-
tion Materiel Laboratories, Fort Eustis, Virginia, March 1970, AD
869823

10. Lowson, M. V., and Ollerhead, J. B., STUDIES OF HELICOPTER ROTOR NOISE, Wyle Laboratories; USAAVLABS Technical Report 68-60, U.S. Army Aviation Materiel Laboratories, Fort Eustis, VA, January 1969, AD 68394
11. Arcidiacono, P. J., THEORETICAL PERFORMANCE OF HELICOPTERS HAVING SECOND AND HIGHER HARMONIC FEATHERING CONTROL, Journal of the American Helicopter Society, Vol. 6, No. 2, April 1961, pp 8-19
12. Gelfand, I. M., and Fomin, S. V., CALCULUS OF VARIATIONS, Prentice-Hall, Inc., Englewood Cliffs, N. J., 1963
13. Niebanck, C. F., MODEL ROTOR TEST DATA FOR VERIFICATION OF BLADE RESPONSE AND ROTOR PERFORMANCE CALCULATIONS, Sikorsky Aircraft Division, United Technologies Corporation; USAAMRDL Technical Report 74-29, Eustis Directorate, U.S. Army Air Mobility Research and Development Laboratory, Fort Eustis, VA, May 1974, AD 786562
14. Tanner, W. H., GENERALIZED ROTOR PERFORMANCE METHOD, Engineering Report SER-50304, Sikorsky Aircraft Division, United Technologies Corporation; May 1964
15. Landgrebe, A. J., AN ANALYTICAL METHOD FOR PREDICTING ROTOR WAKE GEOMETRY, Journal of the American Helicopter Society, Vol. 14, No. 4, October 1969, pp. 20-32
16. Arcidiacono, P. J., PREDICTION OF ROTOR INSTABILITY AT HIGH FORWARD SPEEDS, VOL. I, STEADY FLIGHT DIFFERENTIAL EQUATIONS OF MOTION FOR A FLEXIBLE HELICOPTER BLADE WITH CHORDWISE MASS UNBALANCE, Sikorsky Aircraft Division, United Technologies Corporation; USAAVLABS 68-18A, U.S. Army Aviation Materiel Laboratories, Fort Eustis, Virginia, February 1969, AD 685860
17. Landgrebe, A. J., et al., AERODYNAMIC TECHNOLOGY FOR ADVANCED ROTOR-CRAFT, American Helicopter Society, Symposium on Rotor Technology, August 1976



(a)



(b)

Figure 1. Calculation of Reference Rotor Stall Boundaries.

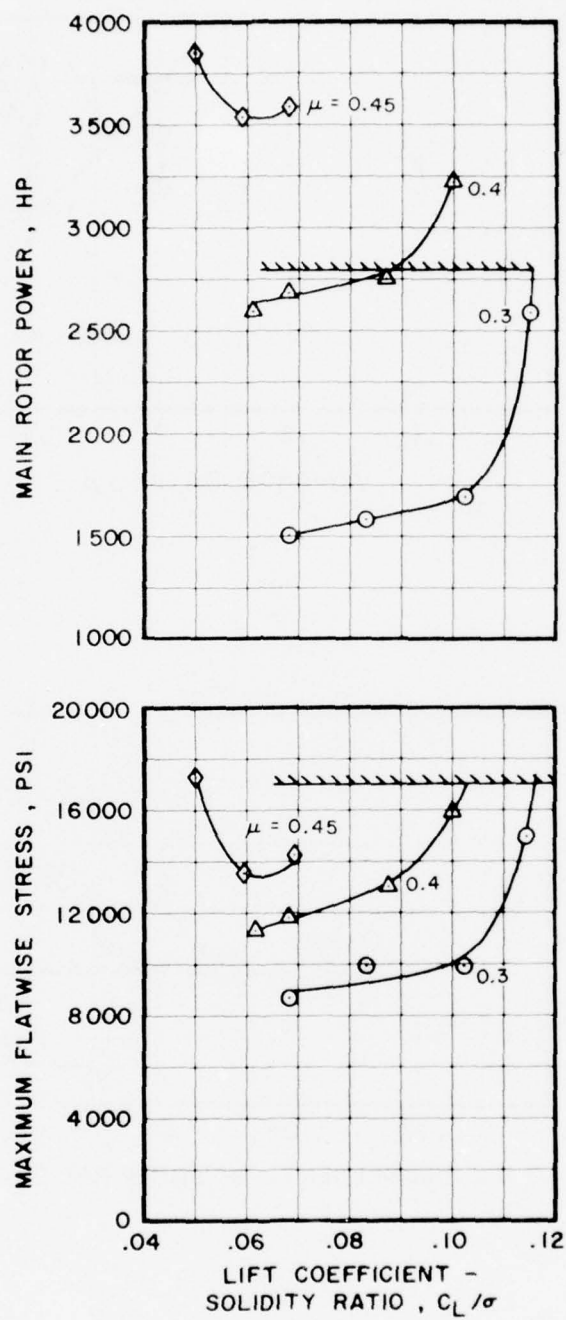


Figure 2. Buildup of Reference Rotor Power and Flatwise Stress With Advance Ratio and Lift Coefficient.

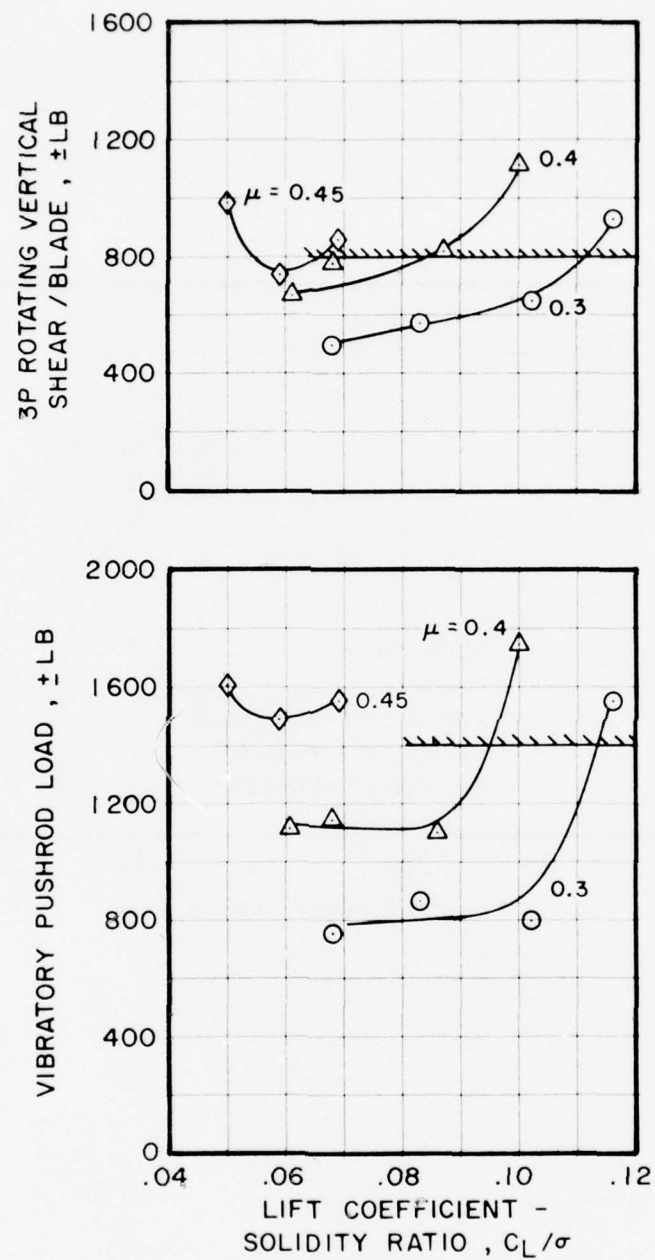


Figure 3. Buildup of Reference Rotor 3P Rotating Vertical Hub Shears and Pushrod Loads With Advance Ratio and Lift Coefficient.

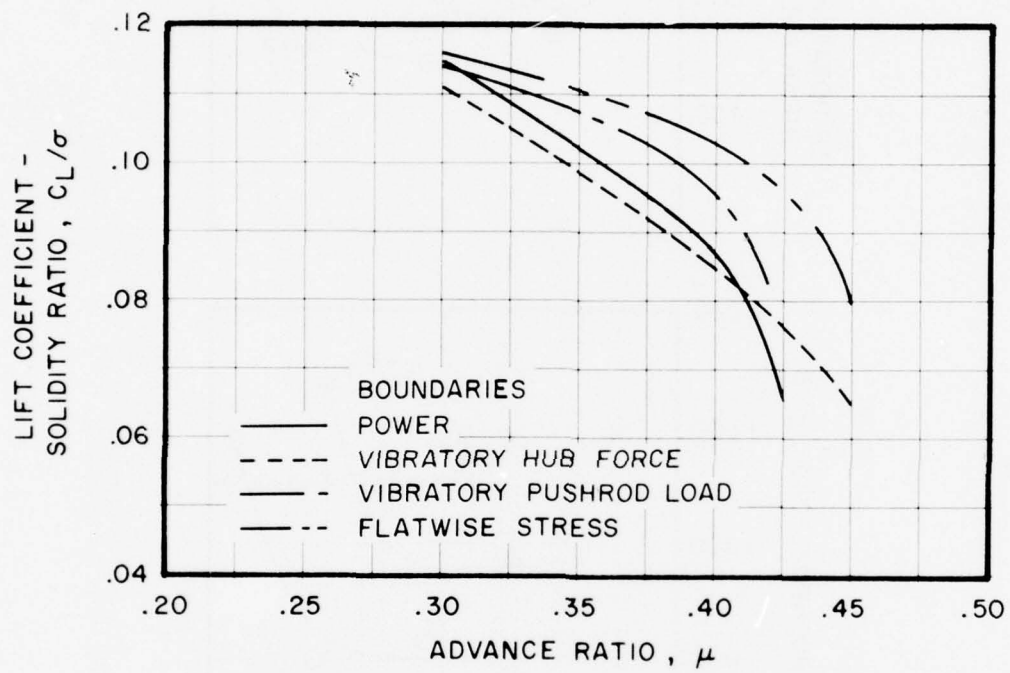


Figure 4. Stall Boundaries of the Reference Rotor.

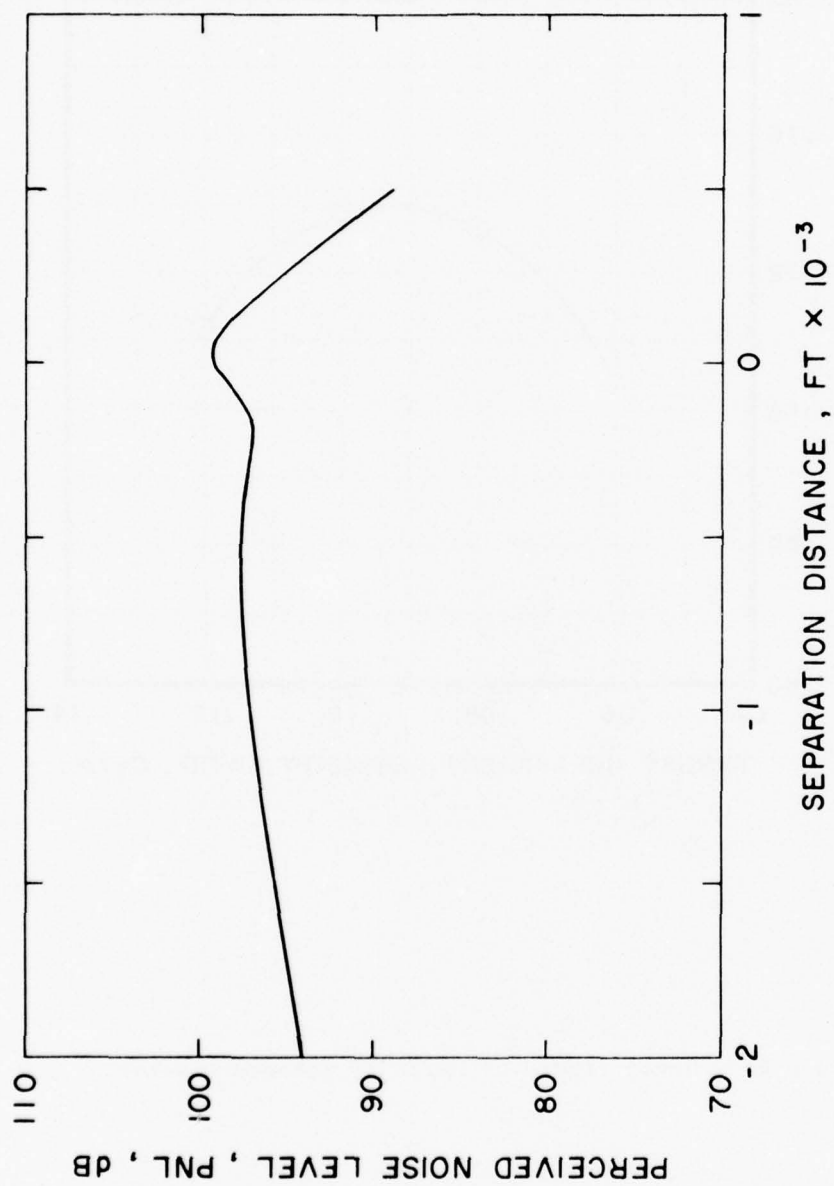


Figure 5. Perceived Noise Levels of the Reference Rotor for 250-ft Altitude Flyover at $\mu=0.4$ and $C_L/\sigma=0.085$.

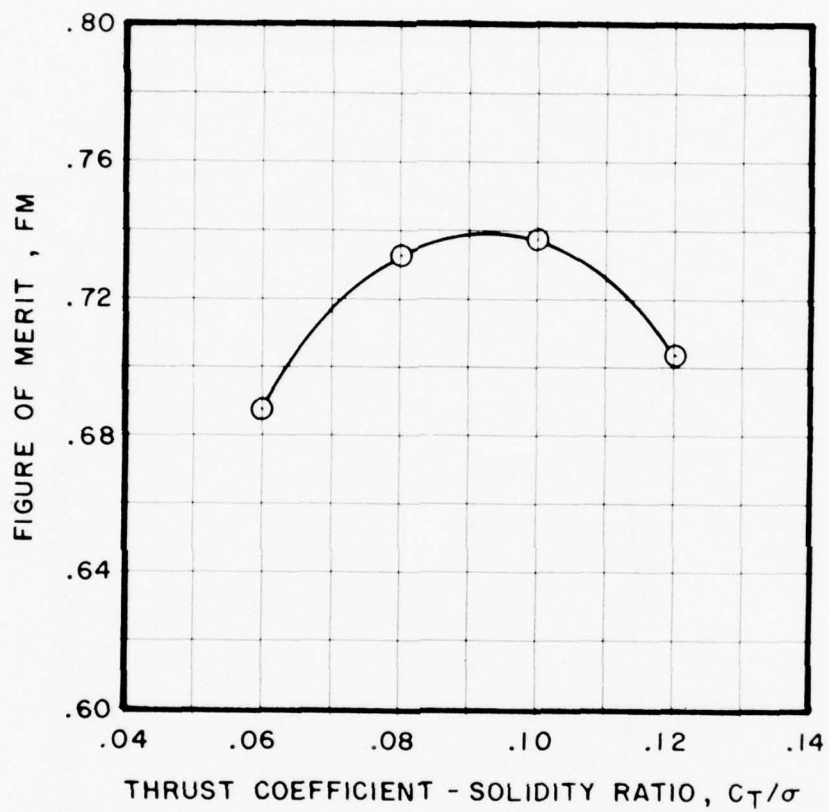


Figure 6. Hover Figure of Merit of Reference Rotor.

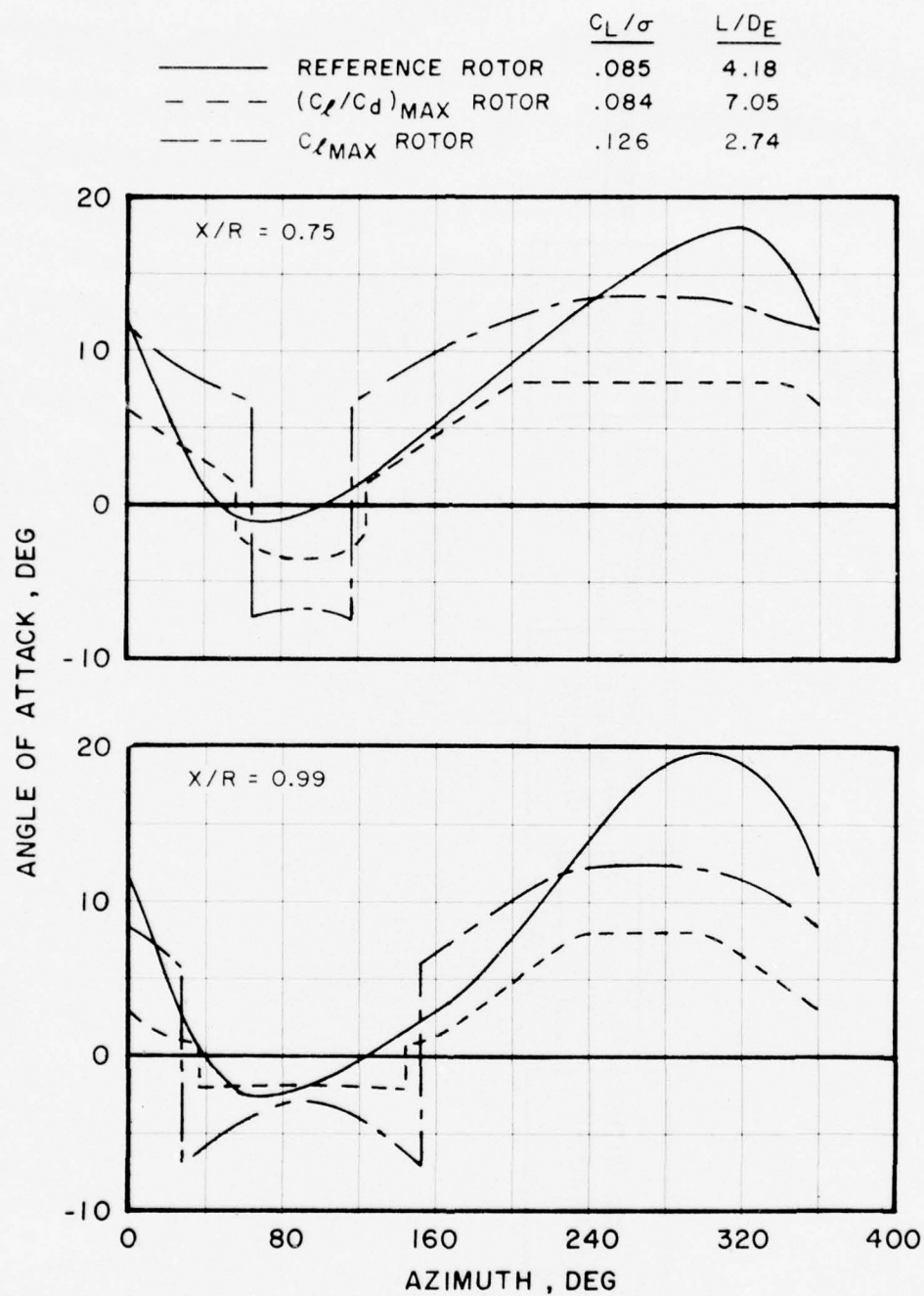


Figure 7. Angle of Attack Distribution of Ideal Rotors at $\mu=0.4$.

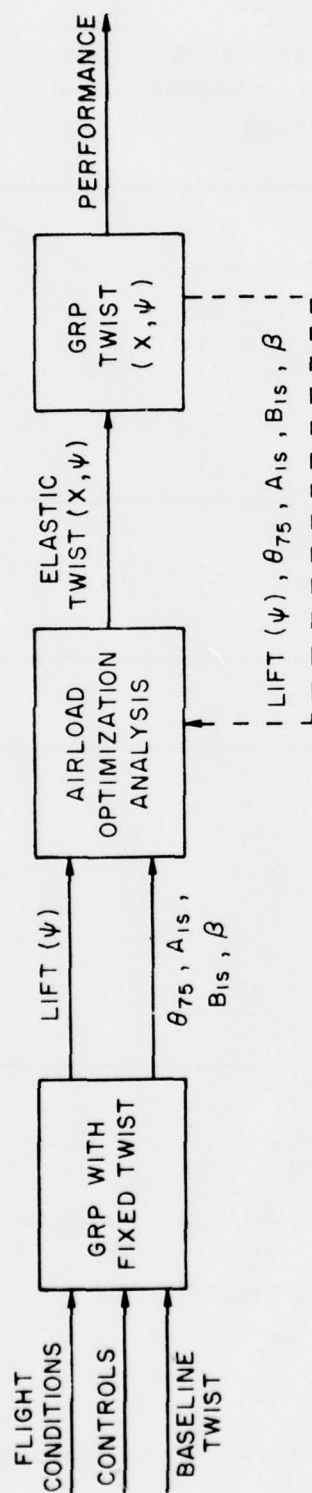


Figure 8. Maximum L/Q_D Rotor Iteration Process.

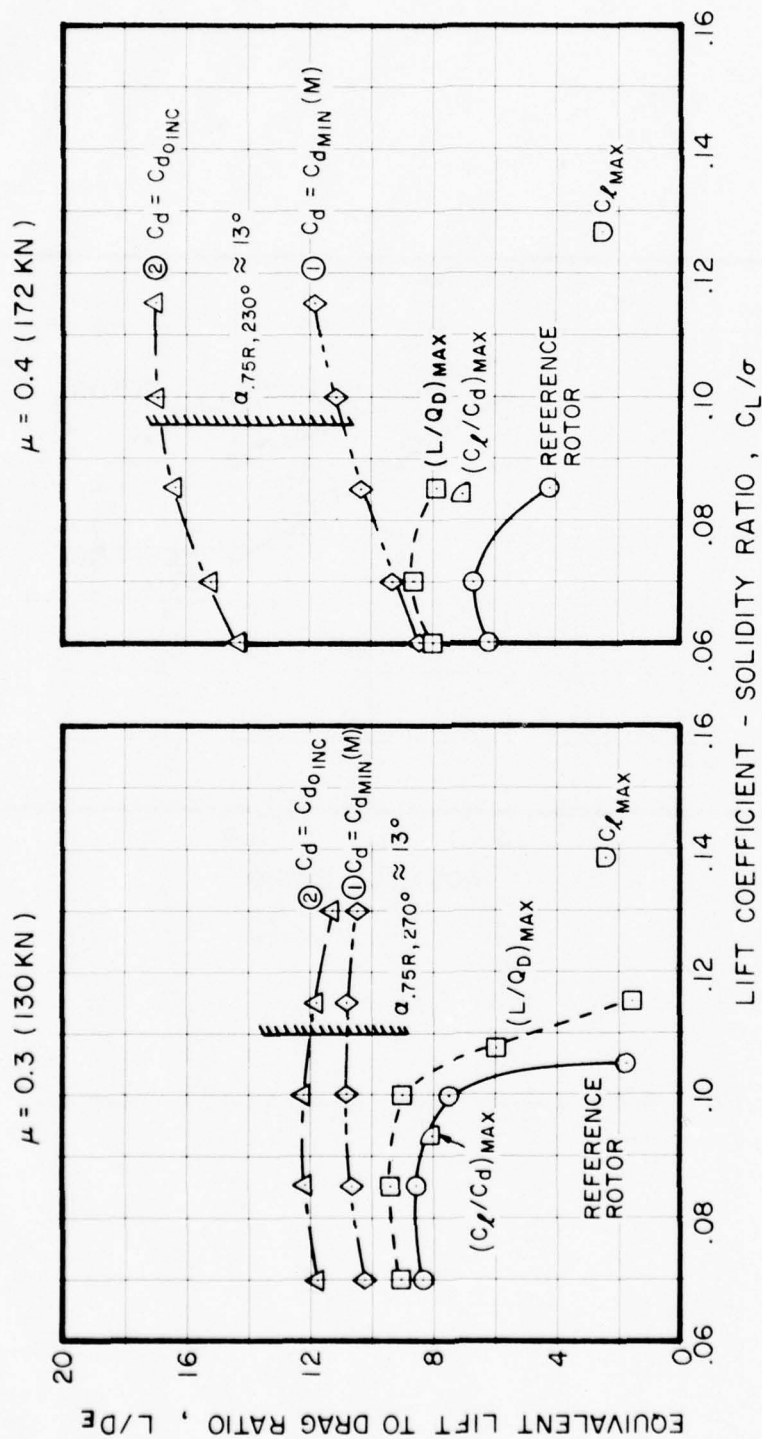


Figure 9. Equivalent Lift-to-Drag Ratios of Reference and Ideal Rotors.

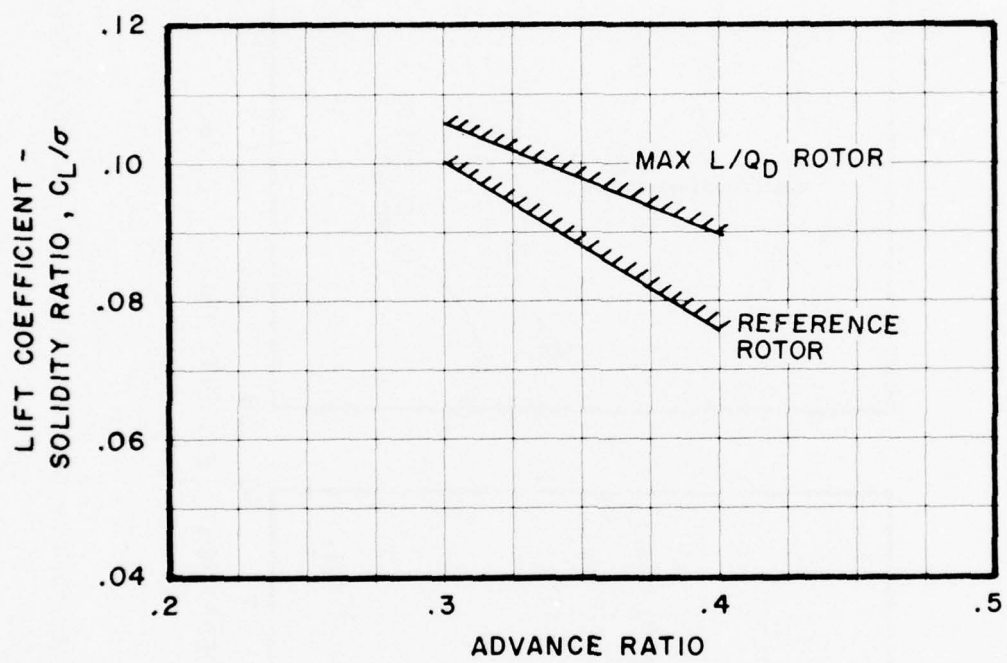


Figure 10. Reference and Ideal Rotor Stall Boundaries.

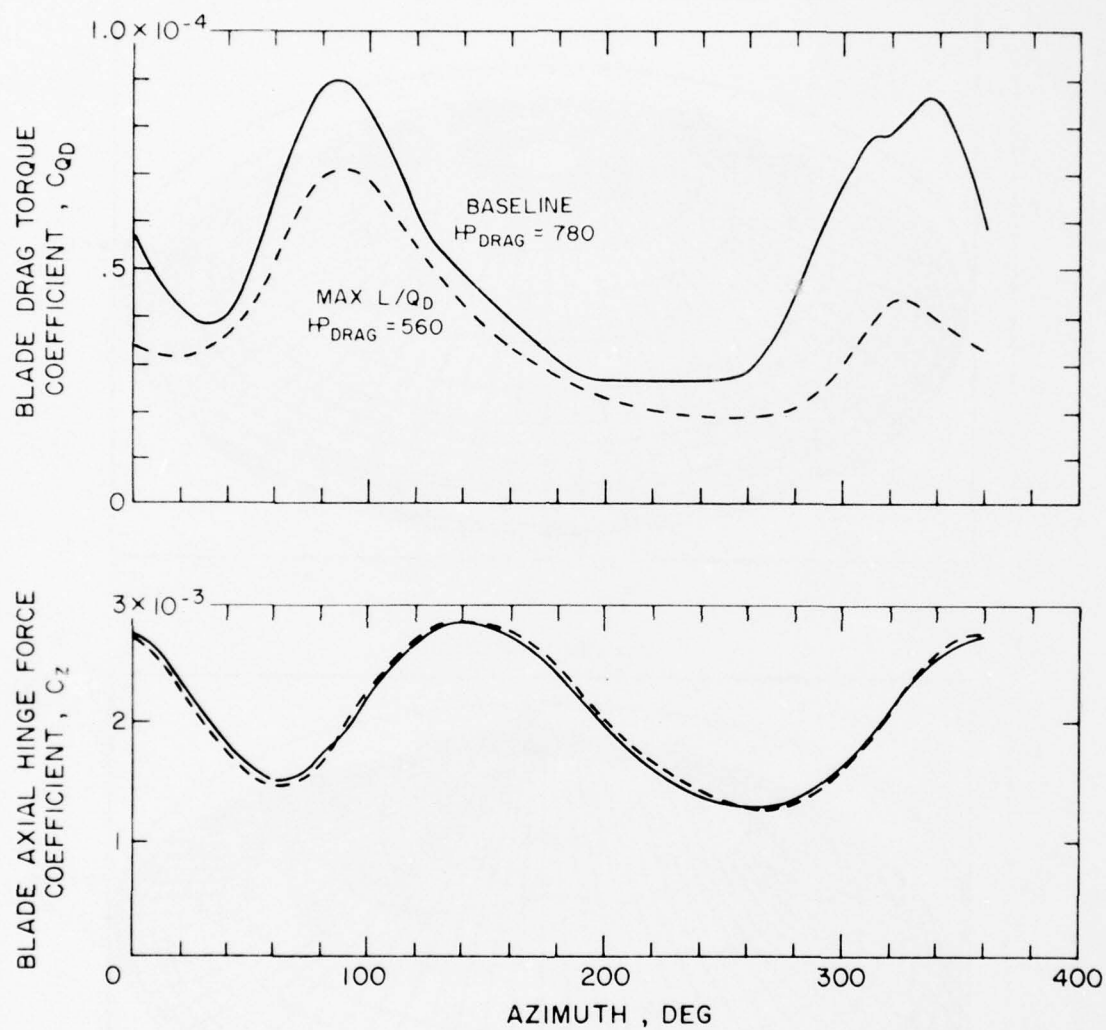


Figure 11. Reduction of Profile Drag Torque With Maximum L/Q_D Rotor.

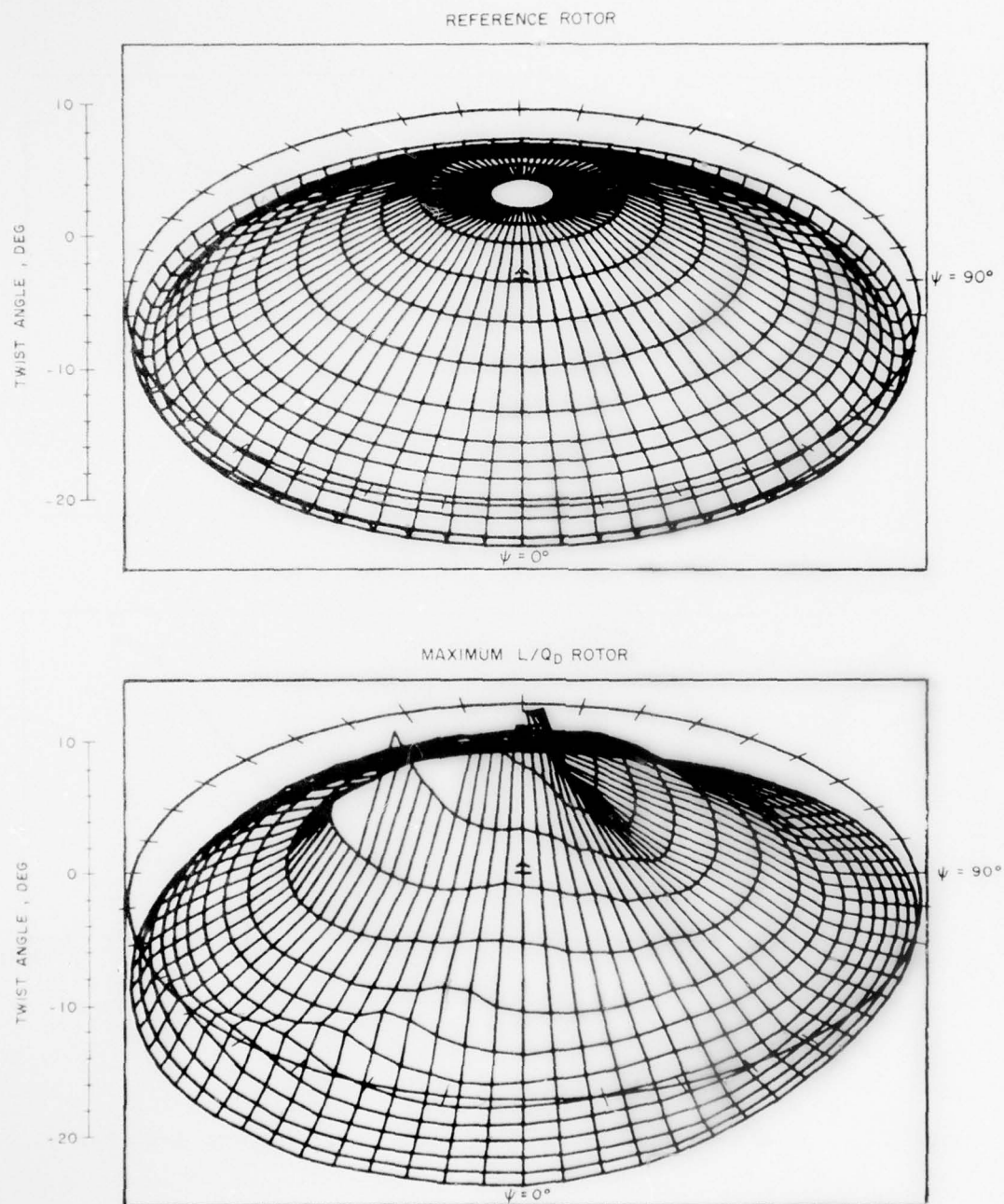


Figure 12. Comparison of Reference and Maximum L/Q_D Rotor Twist Distributions at $\mu=0.3$ and $C_L/C_D=0.10$ (Uniform Inflow).

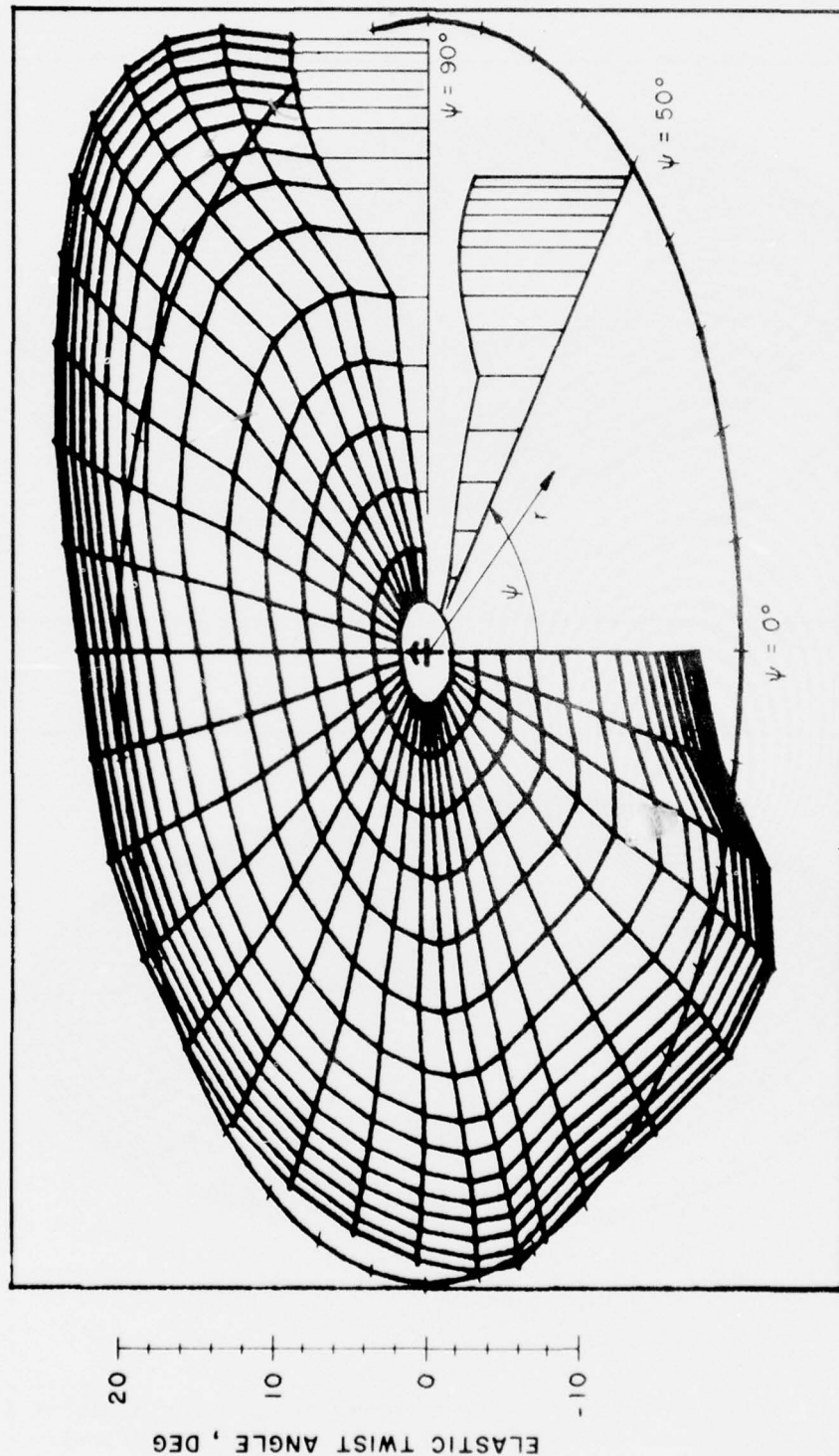


Figure 13. The Use of Compliant Rotor Surface Plots.

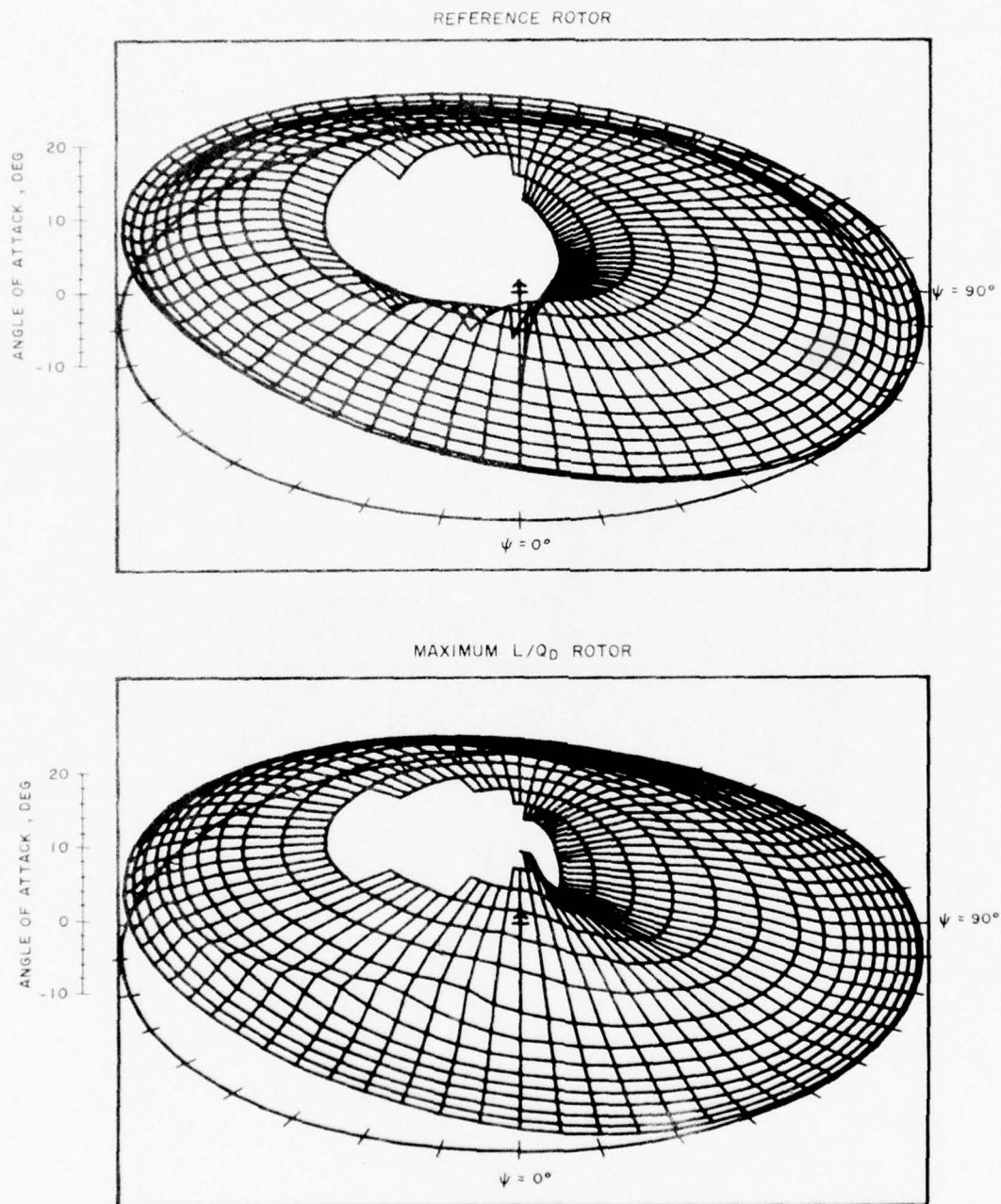


Figure 14. Comparison of Reference and Maximum L/Q_D Rotor Angle of Attack Distributions at $\mu=0.3$ and $C_L/\sigma=0.10$ (Uniform Inflow).

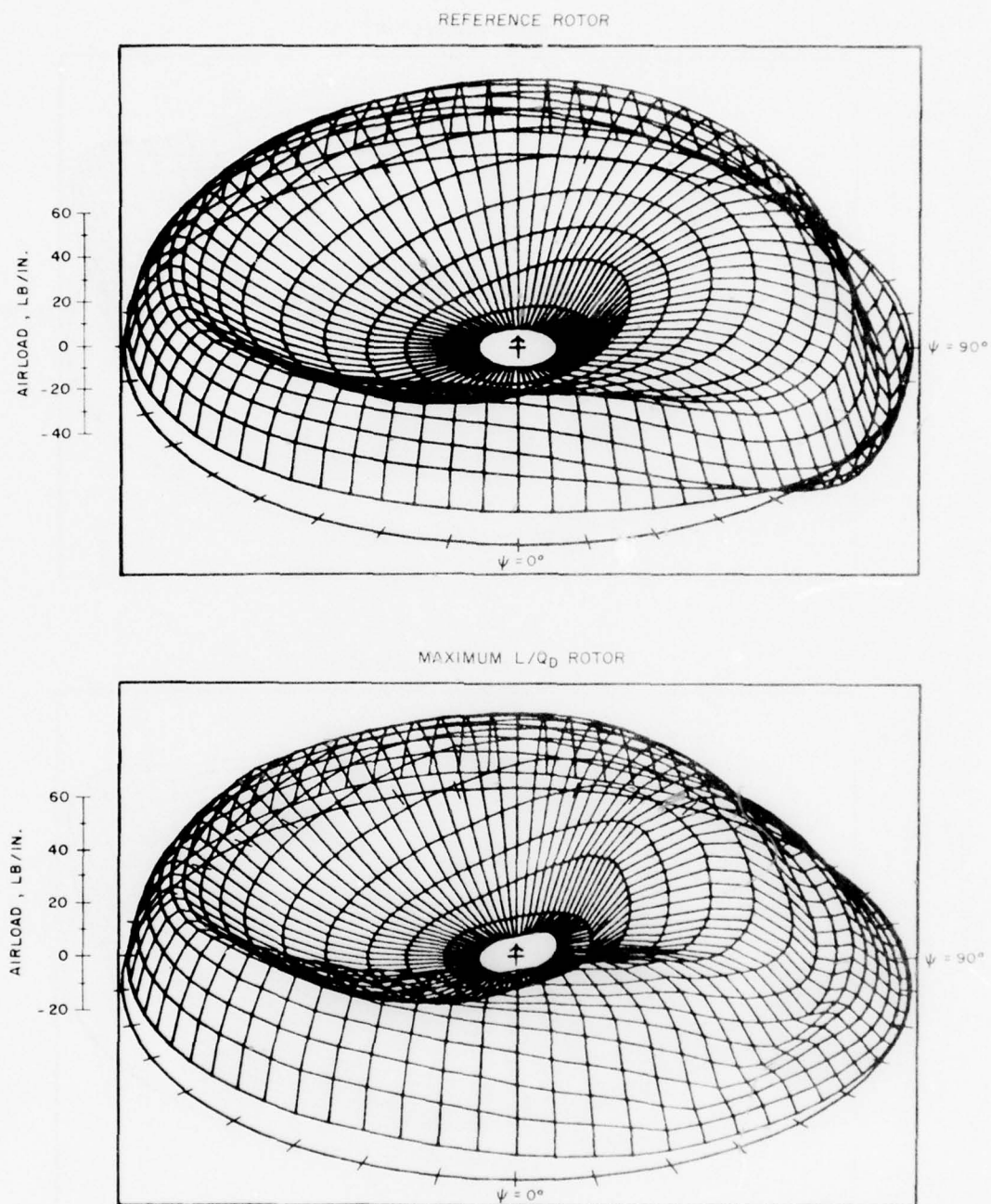


Figure 15. Comparison of Reference and Maximum L/Q_D Rotor Airload Distributions at $\mu=0.3$ and $C_L/\sigma=0.10$ (Uniform Inflow).

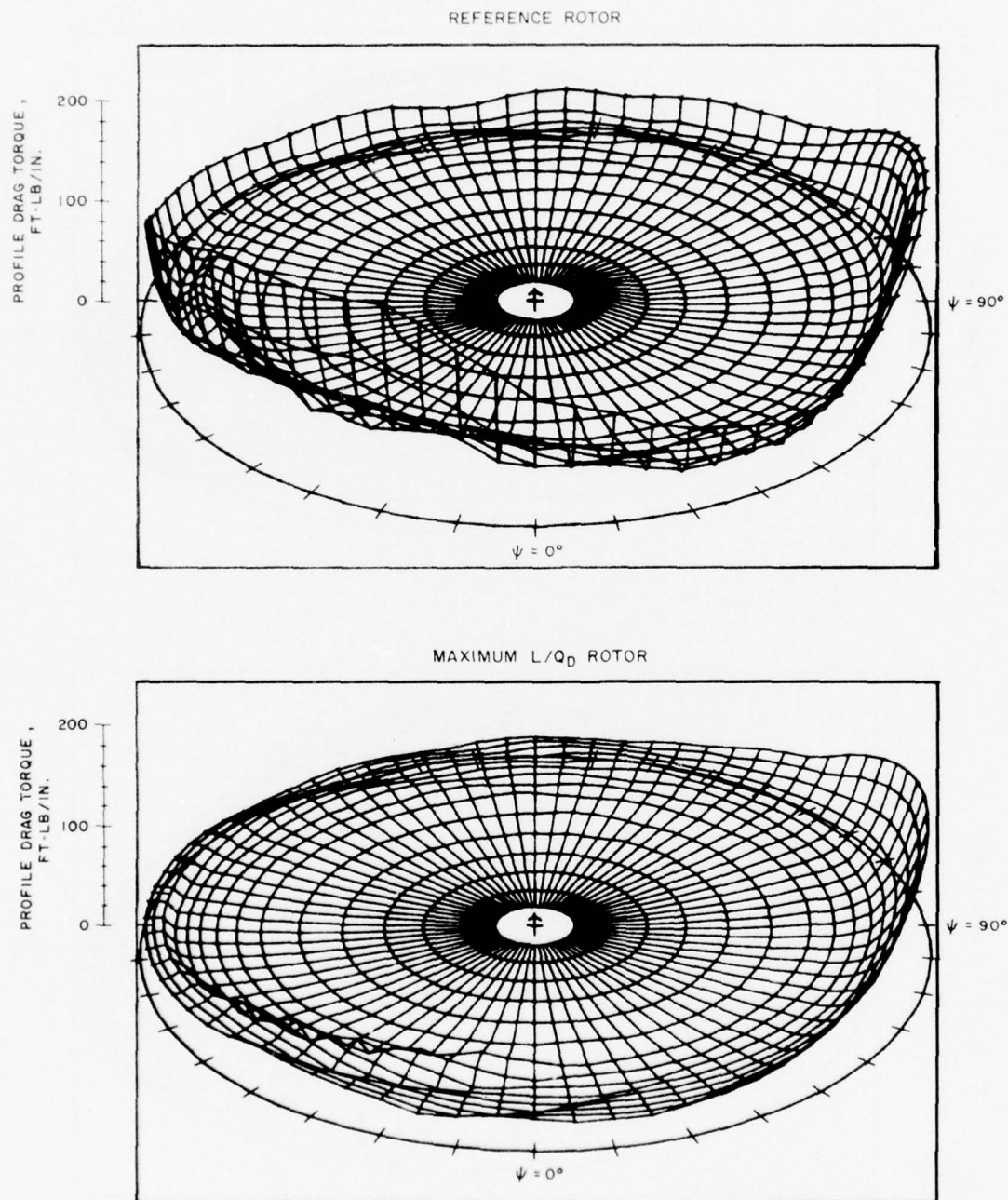


Figure 16. Comparison of Reference and Maximum L/Q_D Rotor Profile Drag Torque Distributions at $\mu=0.3$ and $C_L/\sigma=0.10$ (Uniform Inflow).

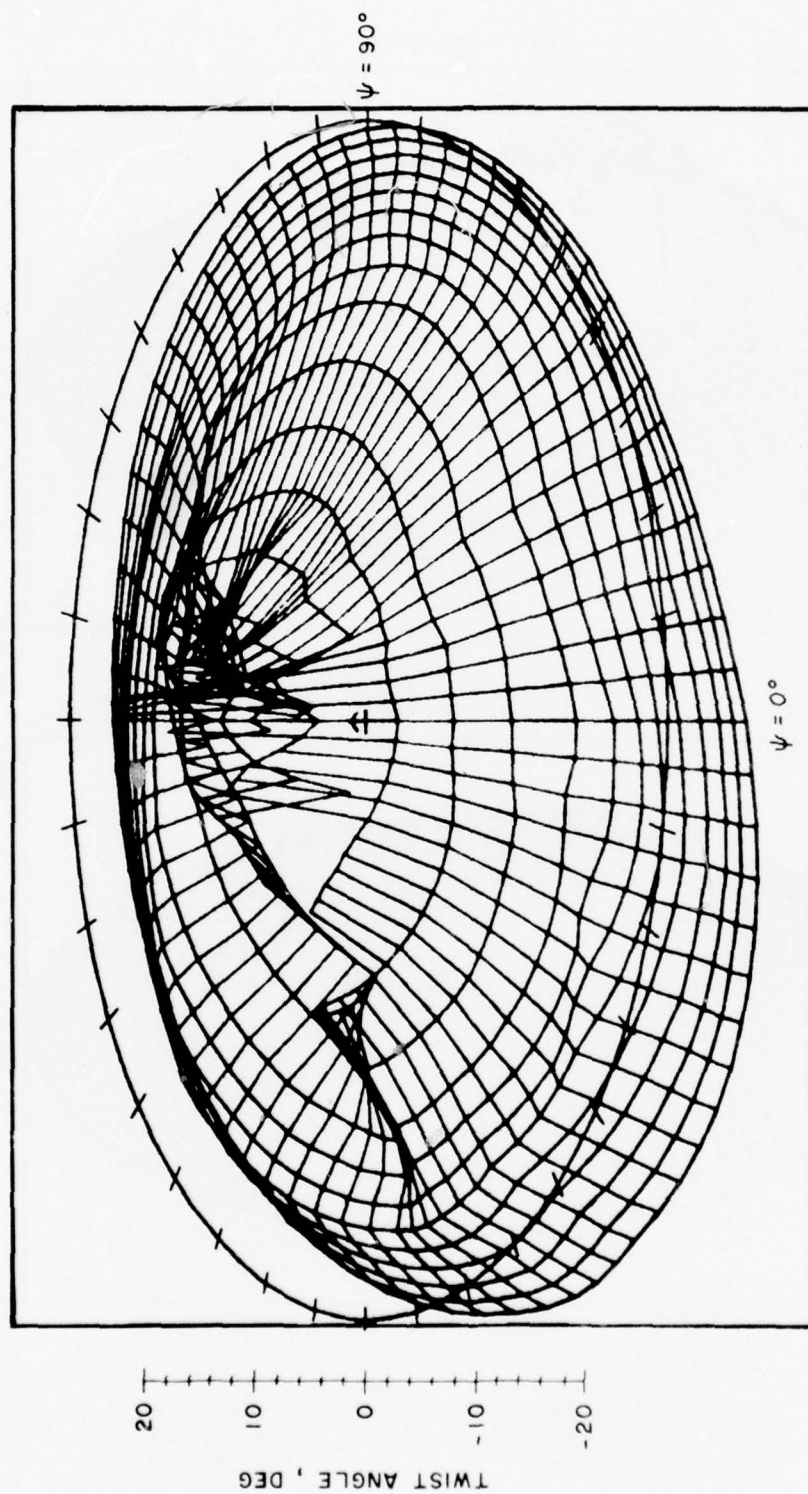


Figure 17. Twist Required to Maximize L/Q_D at $\mu=0.3$ and $C_L/\sigma=0.10$ (Variable Inflow).

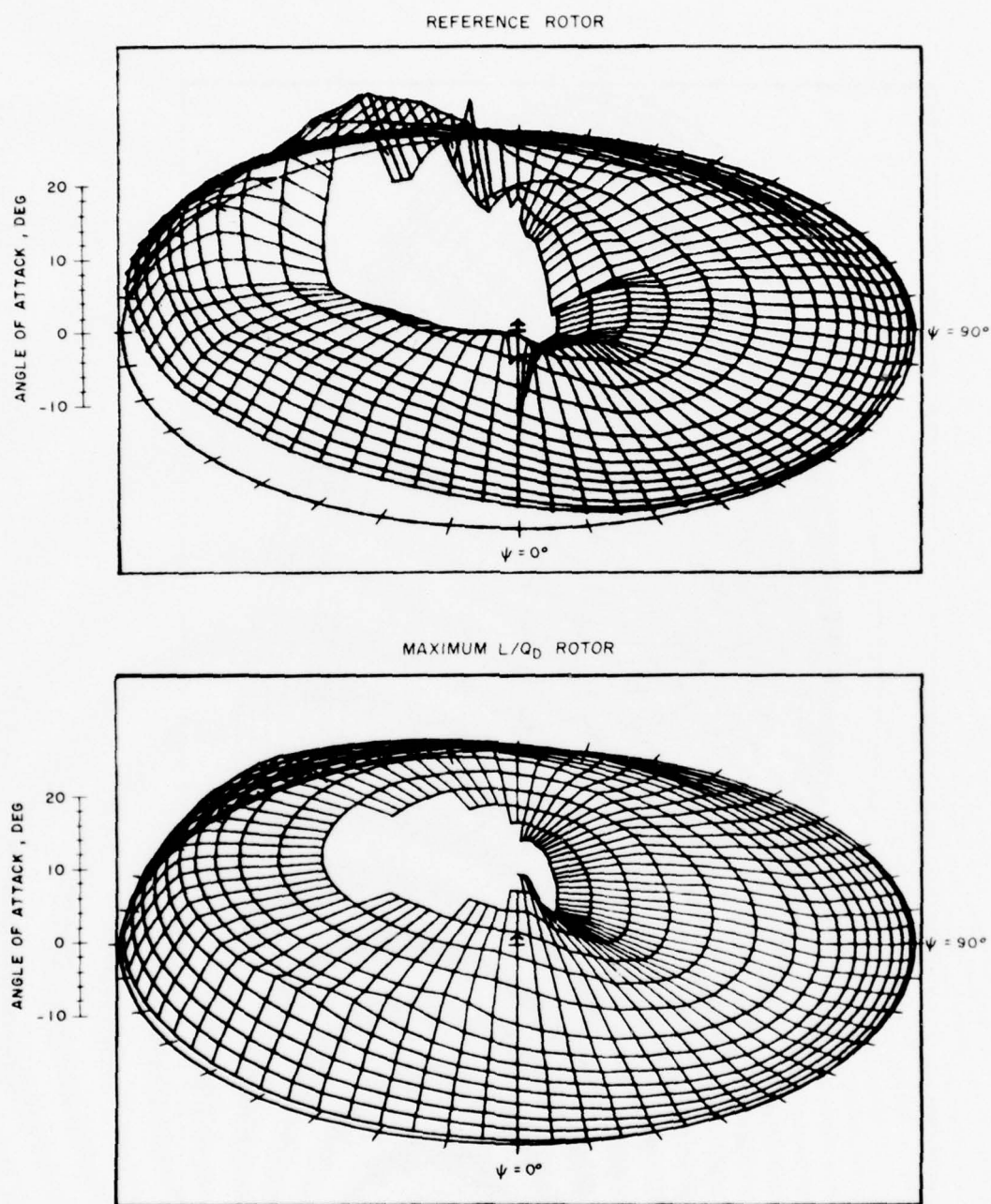


Figure 18. Comparison of Reference and Maximum L/Q_D Rotor Angle of Attack Distributions at $\mu=0.3$ and $C_L/D=0.10$ (Variable Inflow).

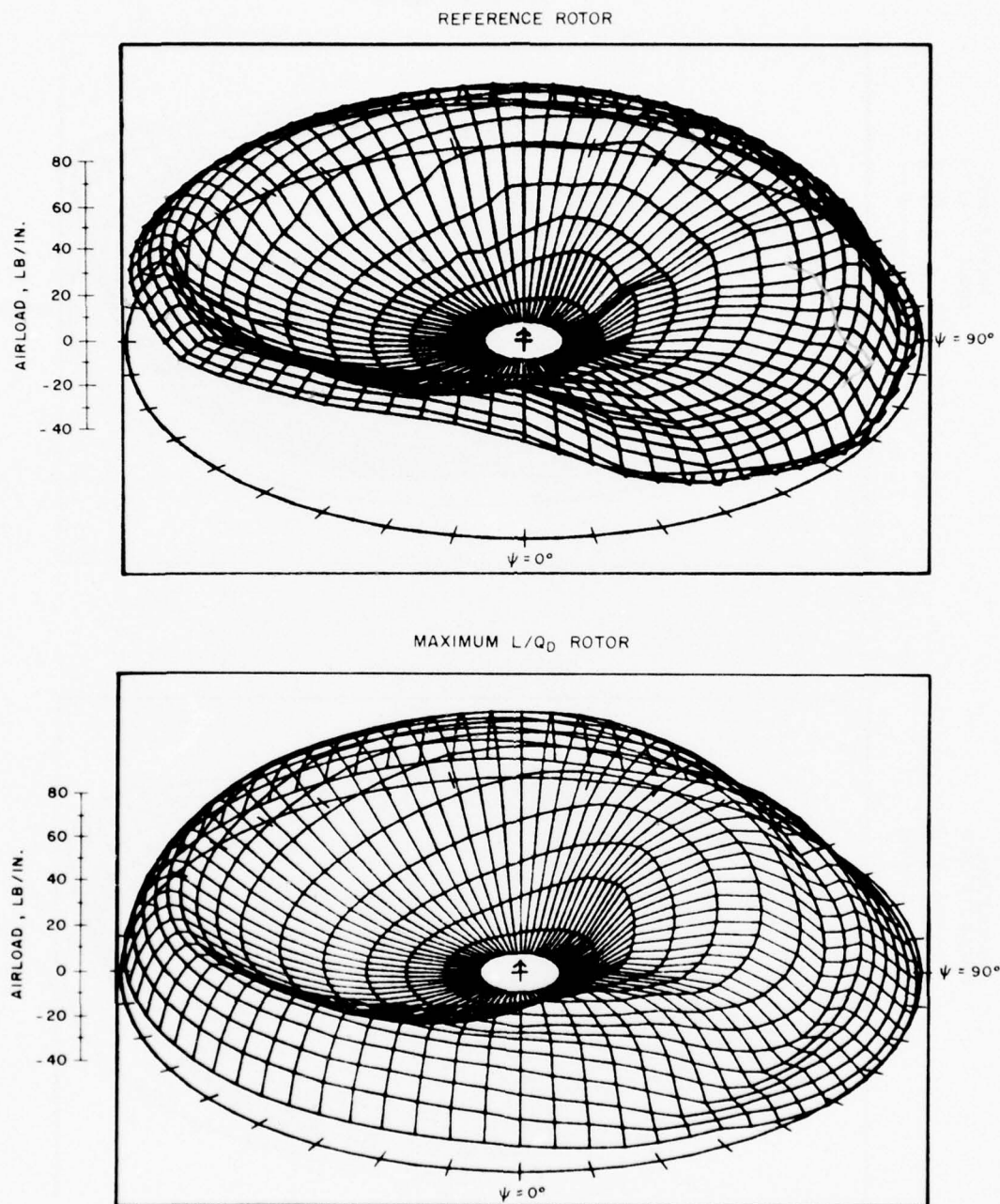


Figure 19. Comparison of Reference and Maximum L/Q_D Rotor Airload Distributions at $\mu=0.3$ and $C_L/\sigma=0.10$ (Variable Inflow).

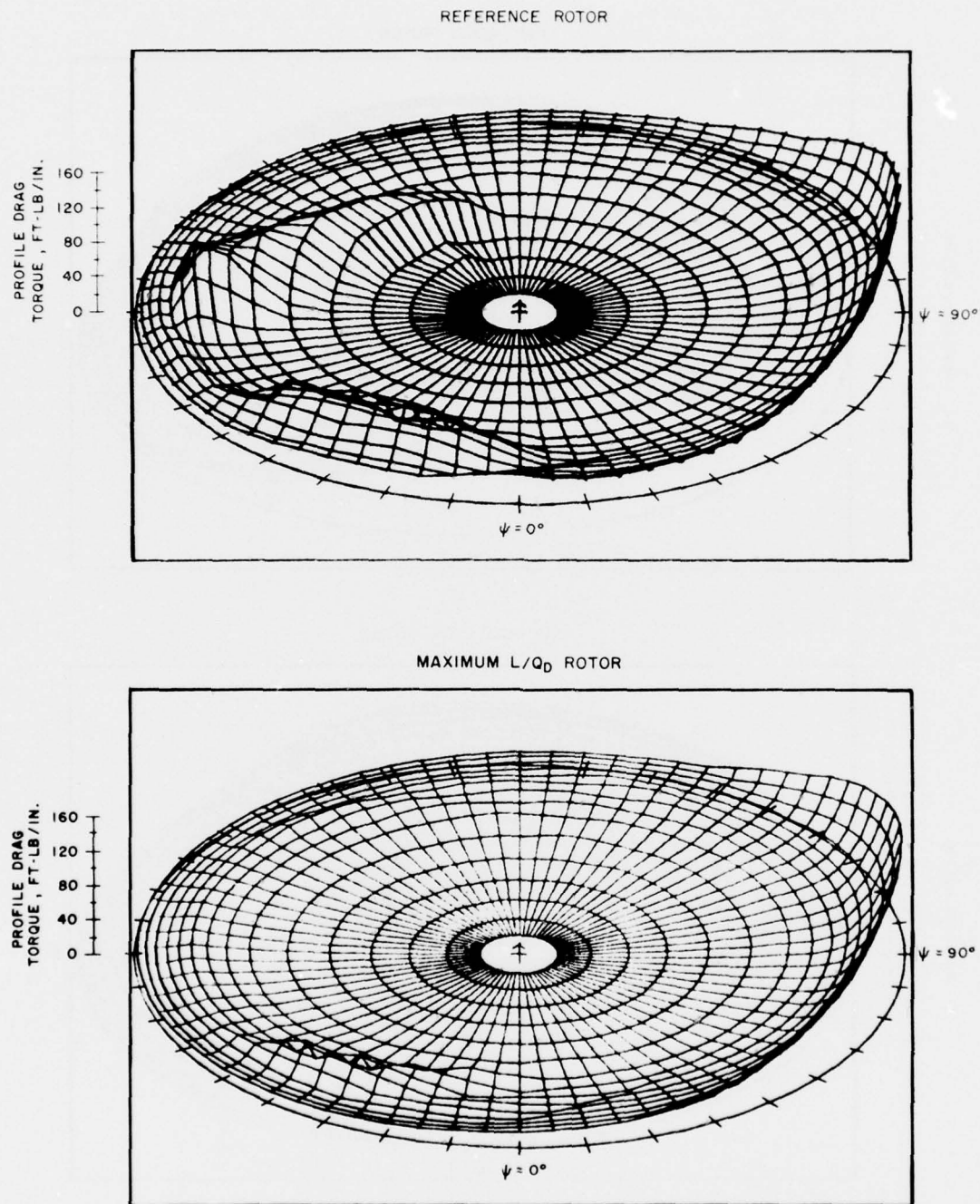


Figure 20. Comparison of Reference and Maximum L/Q_D Rotor Profile Drag Torque Distributions at $\mu=0.3$ and $D_{C_L}/\sigma=0.10$ (Variable Inflow).

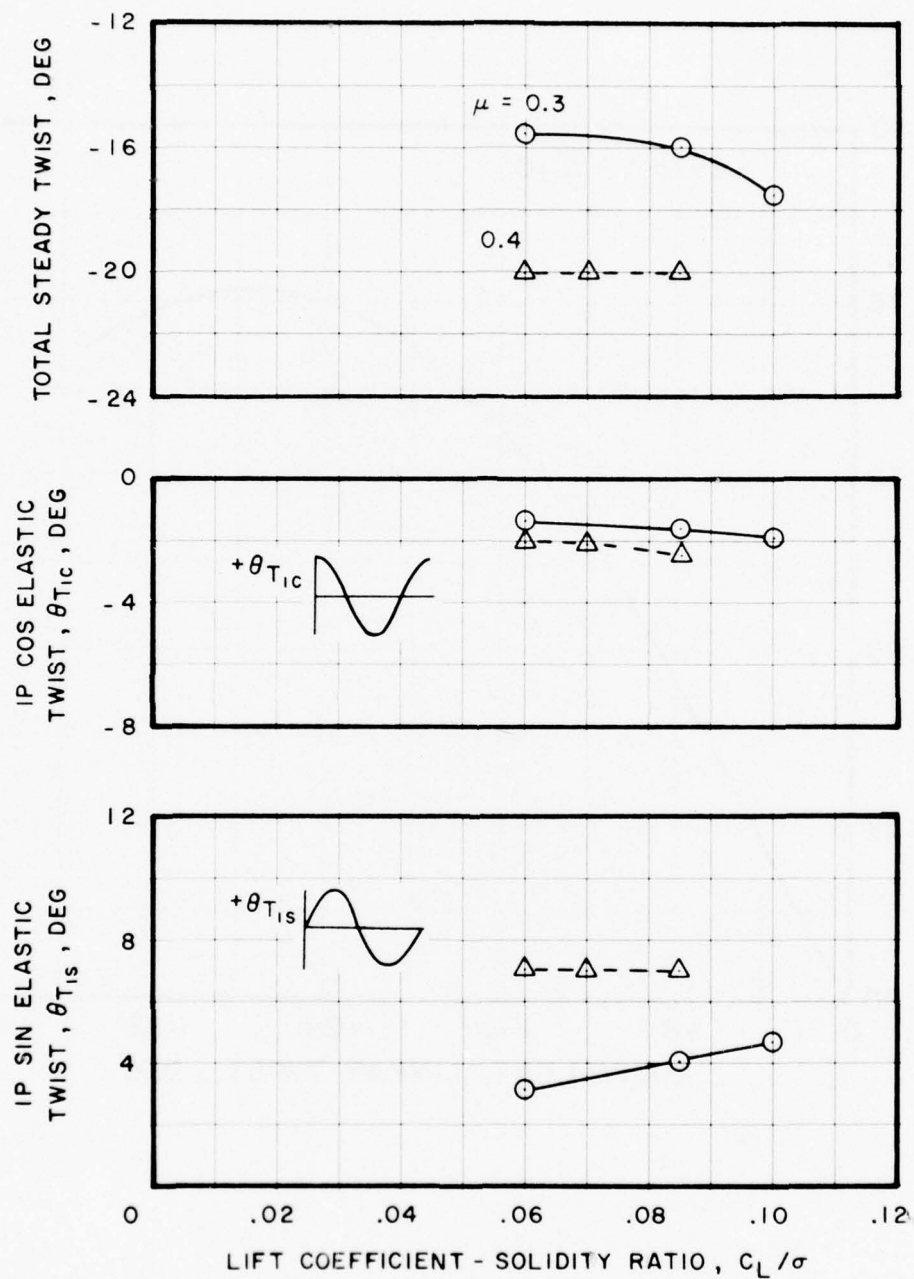


Figure 21. Variation of Ideal Rotor Twist With Advance Ratio and Lift Coefficient.

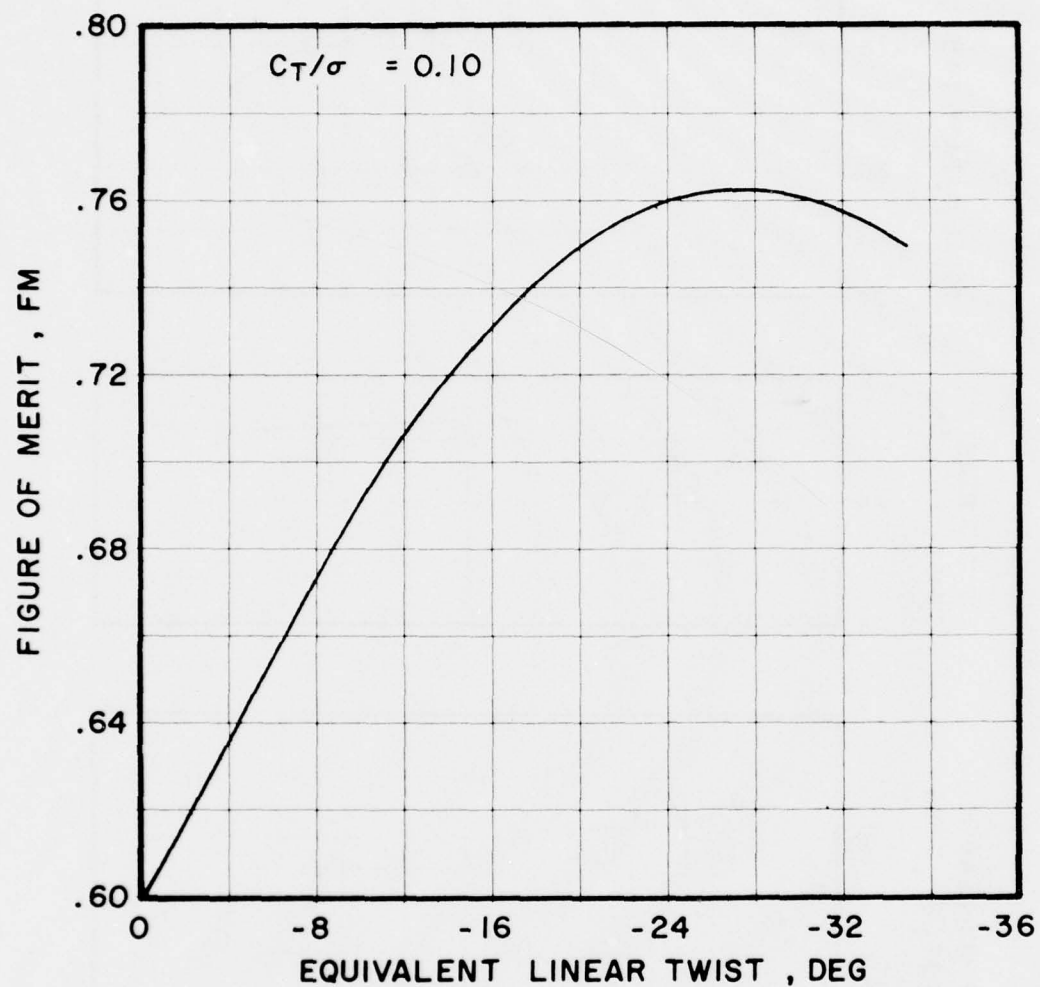


Figure 22. Variation of Hover Figure of Merit With Equivalent Linear Twist Angle at $C_T/\sigma=0.10$.

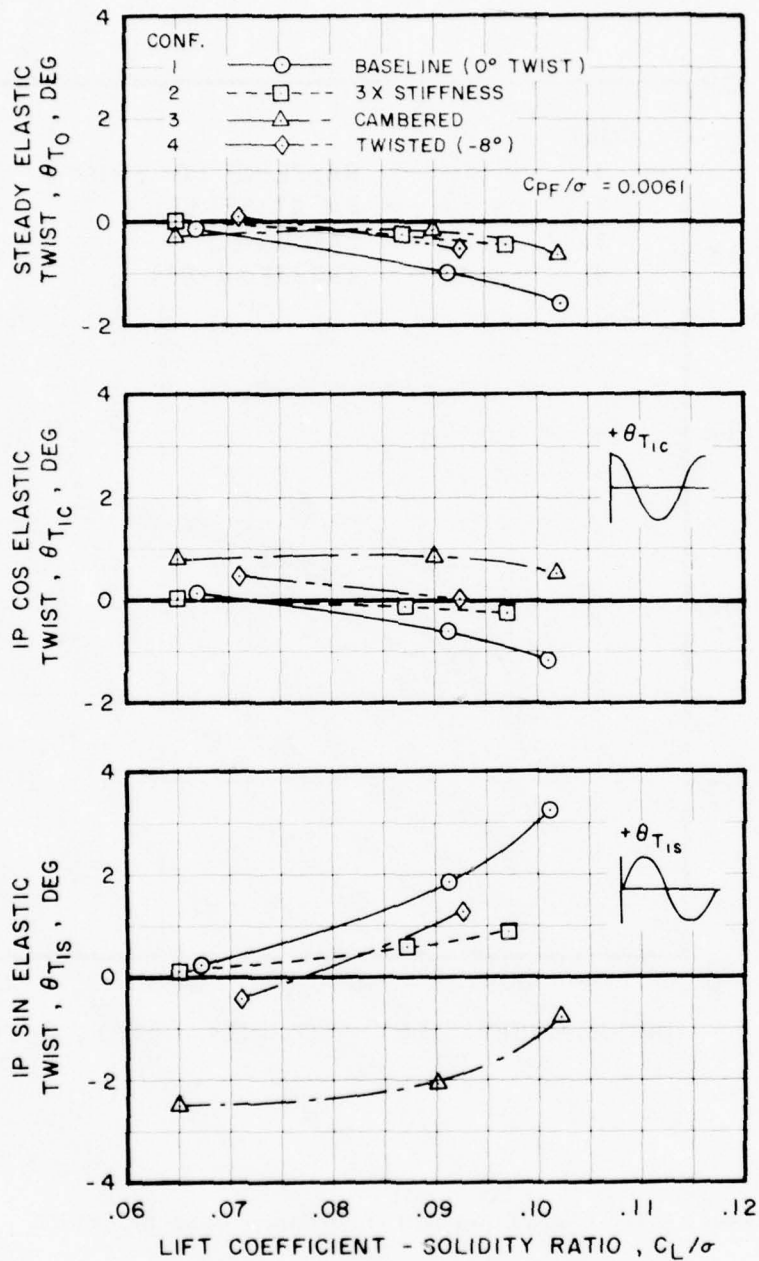


Figure 23. Variation of Model Rotor Elastic Twist With Lift Coefficient at $\mu=0.3$.

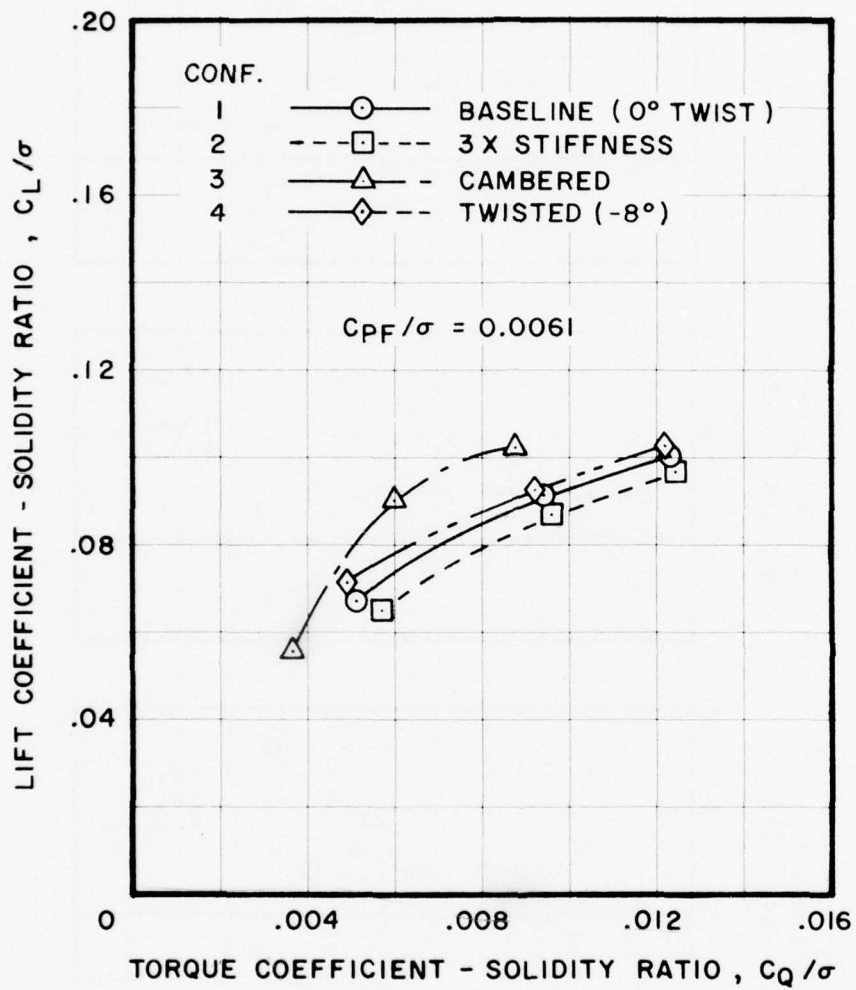


Figure 24. Model Rotor Performance Data at $\mu=0.3$.

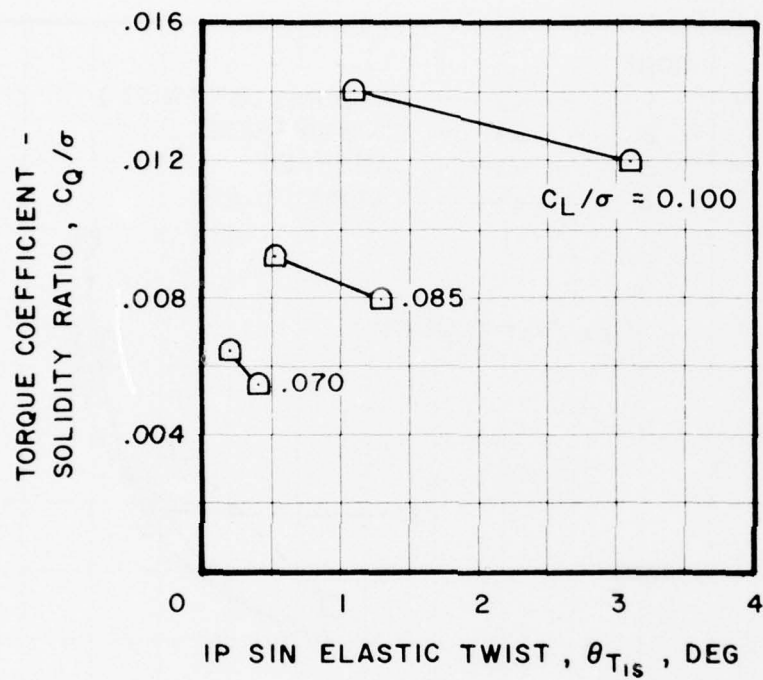


Figure 25. Effect of IP Lateral Twisting on 9-ft-diameter Model Rotor Performance at $\mu=0.3$.

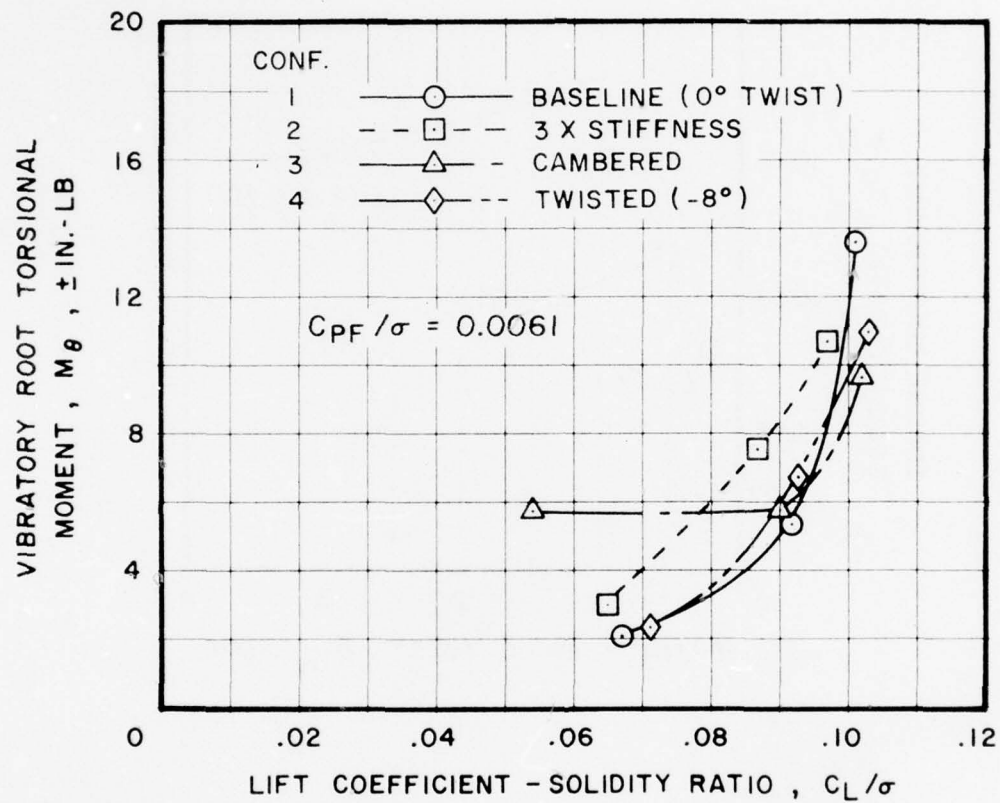


Figure 26. Buildup of Vibratory Blade Root Torsional Moments With Lift Coefficient at $\mu=0.3$.

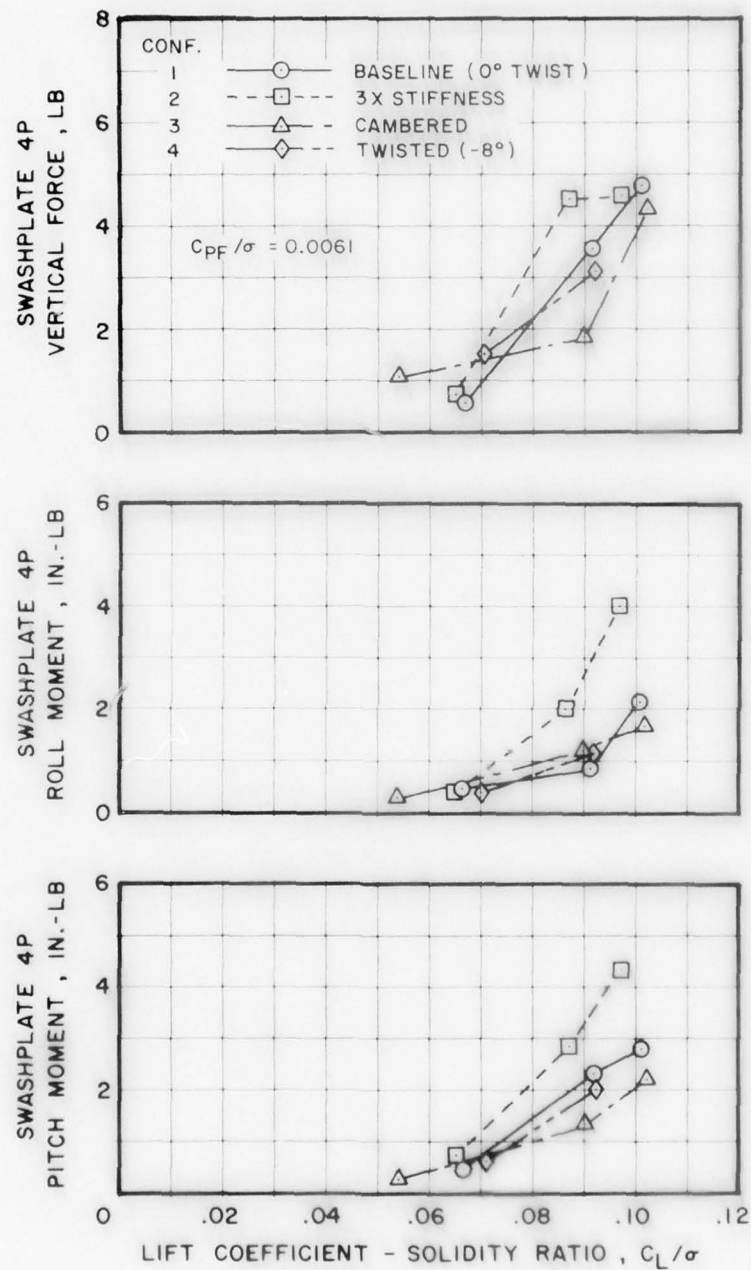


Figure 27. Buildup of Fixed System Control Loads With Lift Coefficient at $\mu=0.3$.

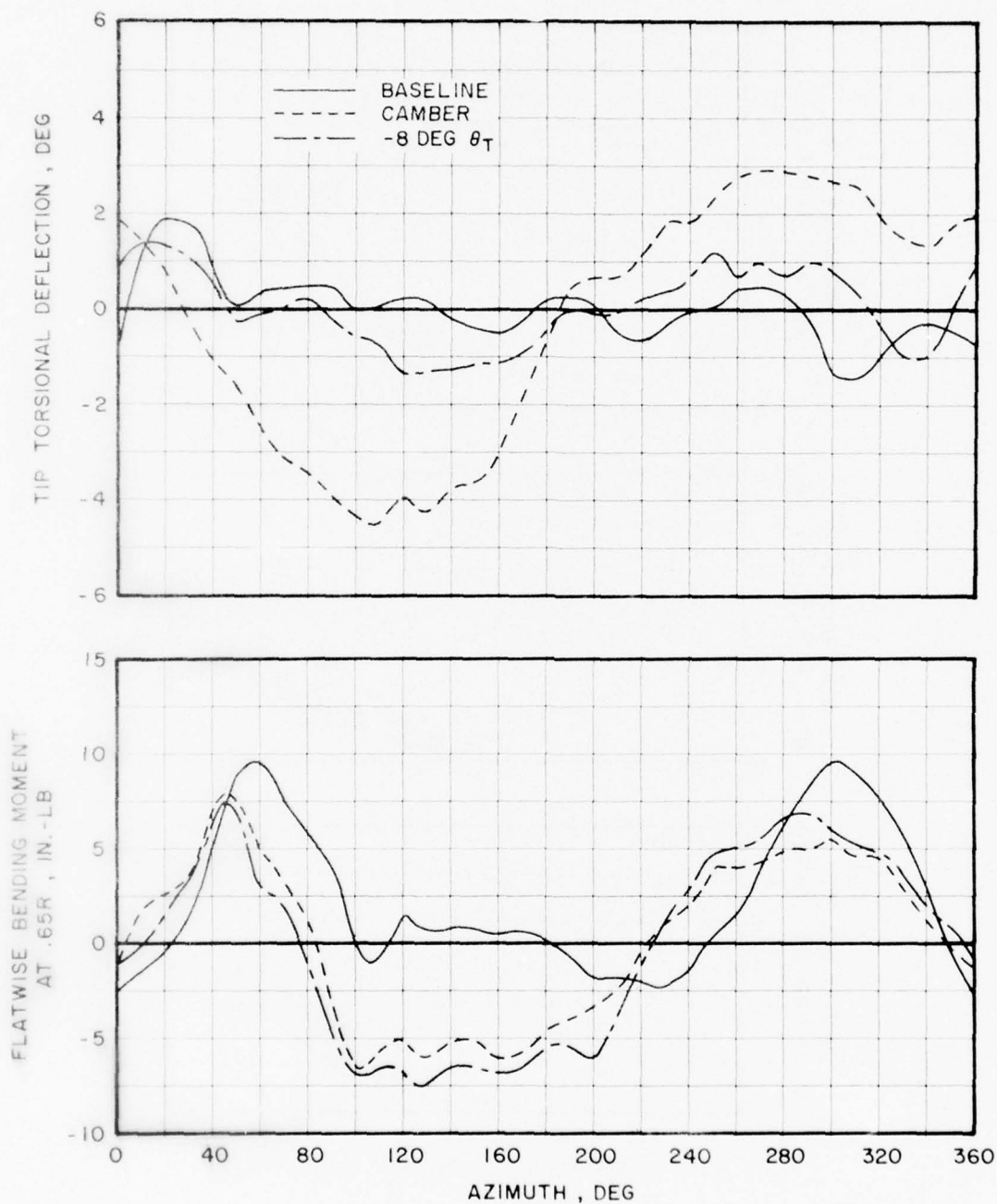
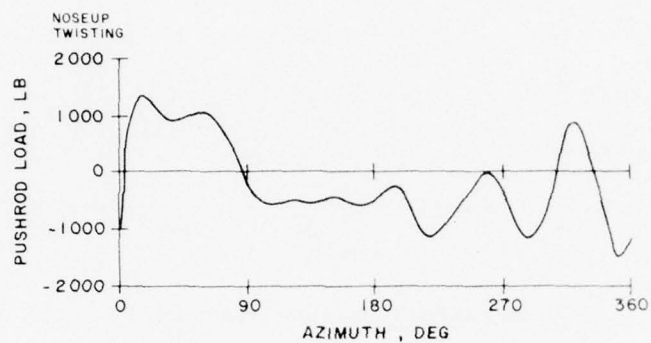
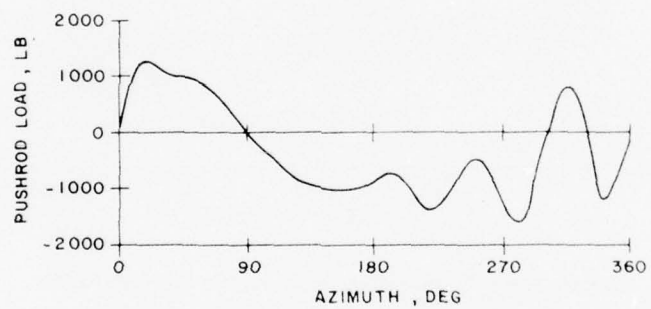


Figure 28. Torsional Deflection and Flatwise Stress of Three 9-ft Diameter Model Rotors at $\mu=0.3$.

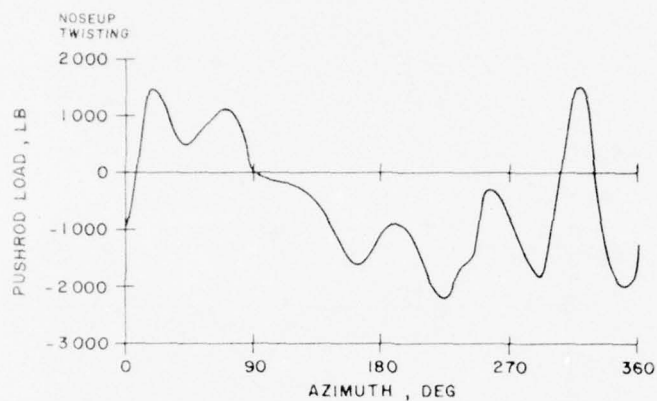


(a) CONFIGURATION 1 H-53 SPAR (-6° TWIST)

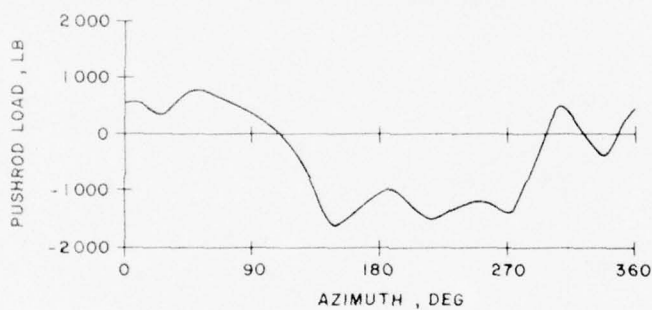


(b) CONFIGURATION 2 H-53 SPAR WITH HIGH-TWIST-SWEPT TIP

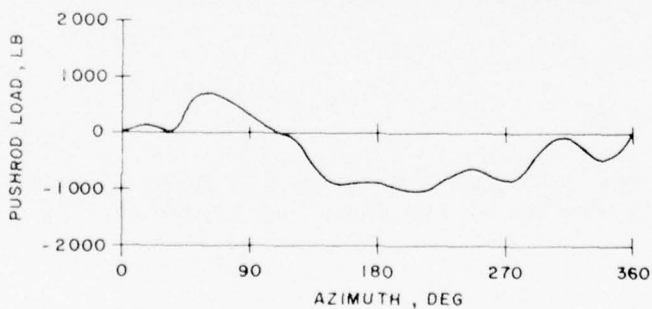
Figure 29. The Effect of H-53 Blade Tip Sweep on Pushrod Load Time Histories at 150 Knots and 42,000 lb Lift.



(a) CONFIGURATION 3 H-54 SPAR (-14° TWIST)

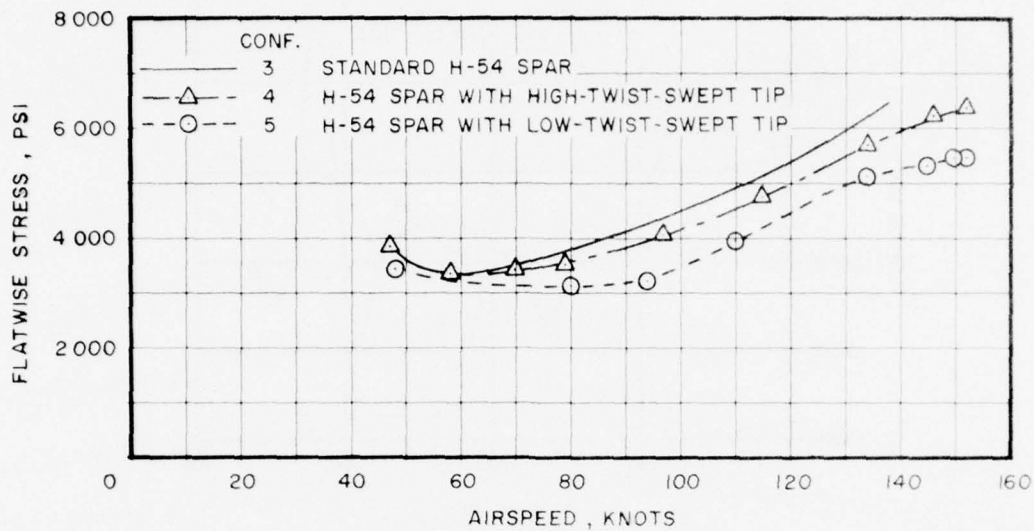


(b) CONFIGURATION 4 H-54 SPAR WITH HIGH-TWIST-SWEPT TIP

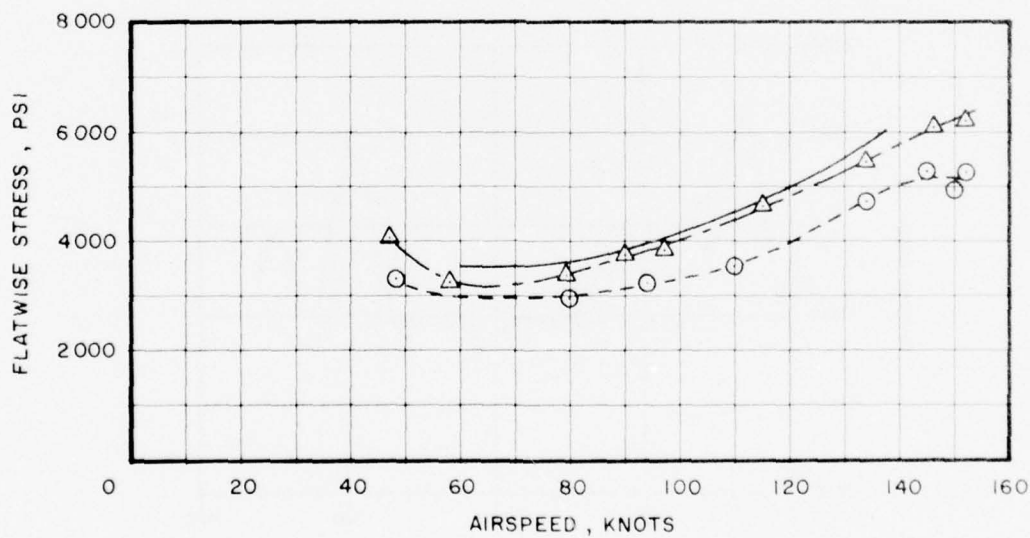


(c) CONFIGURATION 5 H-54 SPAR (-14° TWIST) SWEPT TIP

Figure 30. The Effect of H-54 Blade Tip Sweep on Pushrod Load Time Histories at 150 Knots and 42,000 lb Lift.

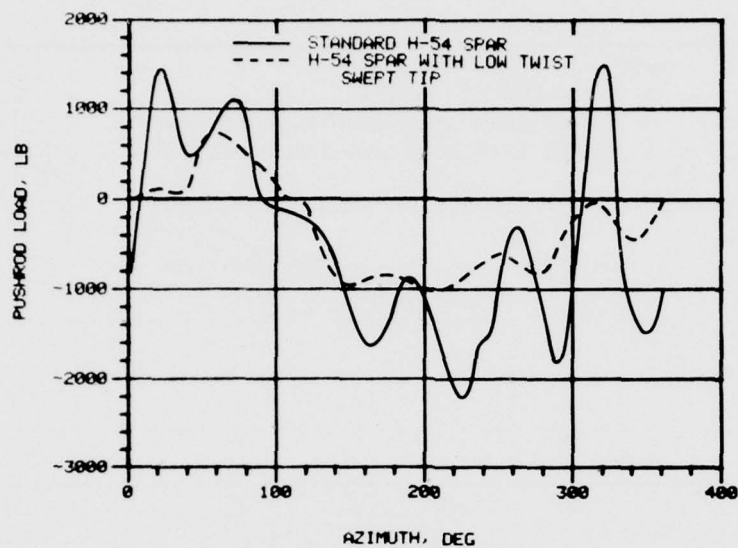


(a) $X/R = 0.6$

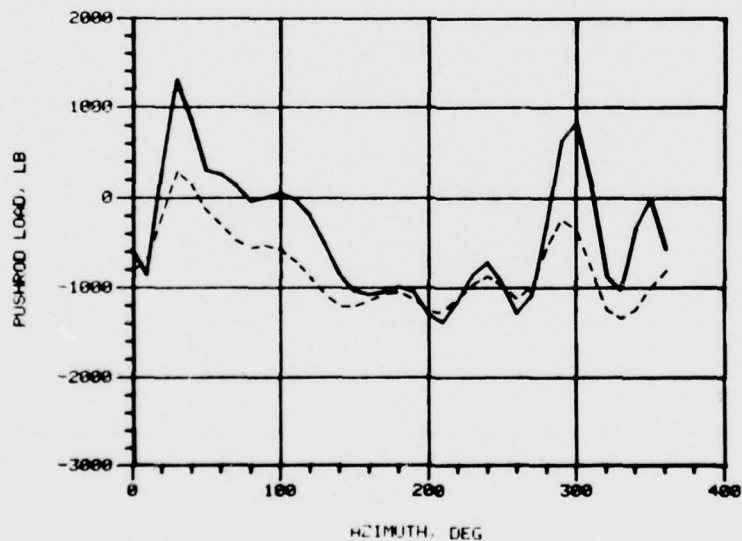


(b) $X/R = 0.7$

Figure 31. The Effect of Tip Sweep on the Buildup of H-54 Blade Flatwise Stress.

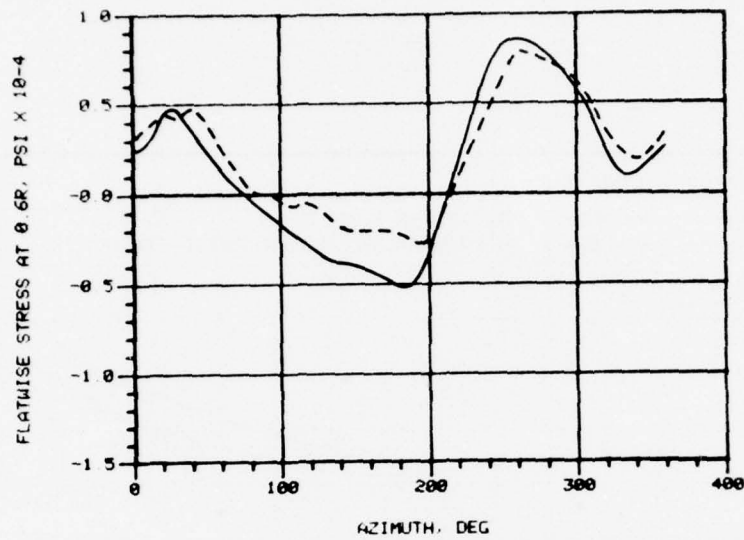


(a) TEST

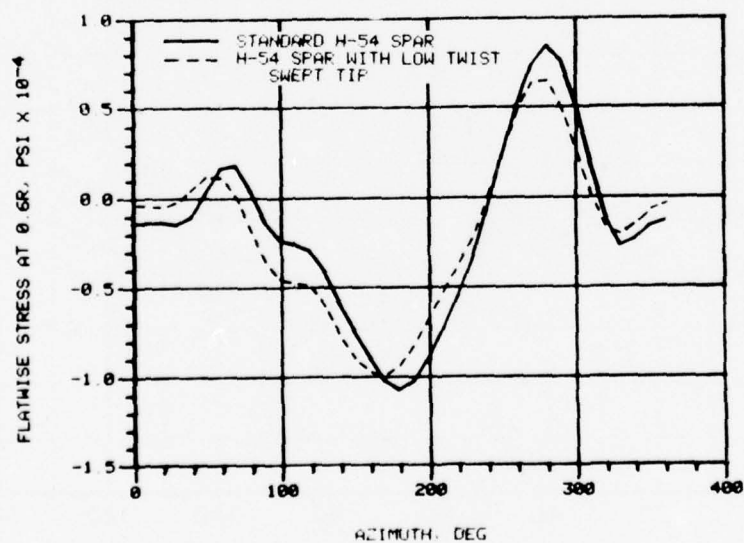


(b) ANALYSIS

Figure 32. Comparison of Measured and Predicted Effects of Tip Sweep on Pushrod Load Time Histories of H-54 Blade at 150 Knots and 42,000 lb Lift.



(a) TEST



(b) ANALYSIS

Figure 33. Comparison of Measured and Predicted Effects of Tip Sweep on Flatwise Stress Time Histories of H-54 Blade at 150 knots and 42,000 lb Lift.

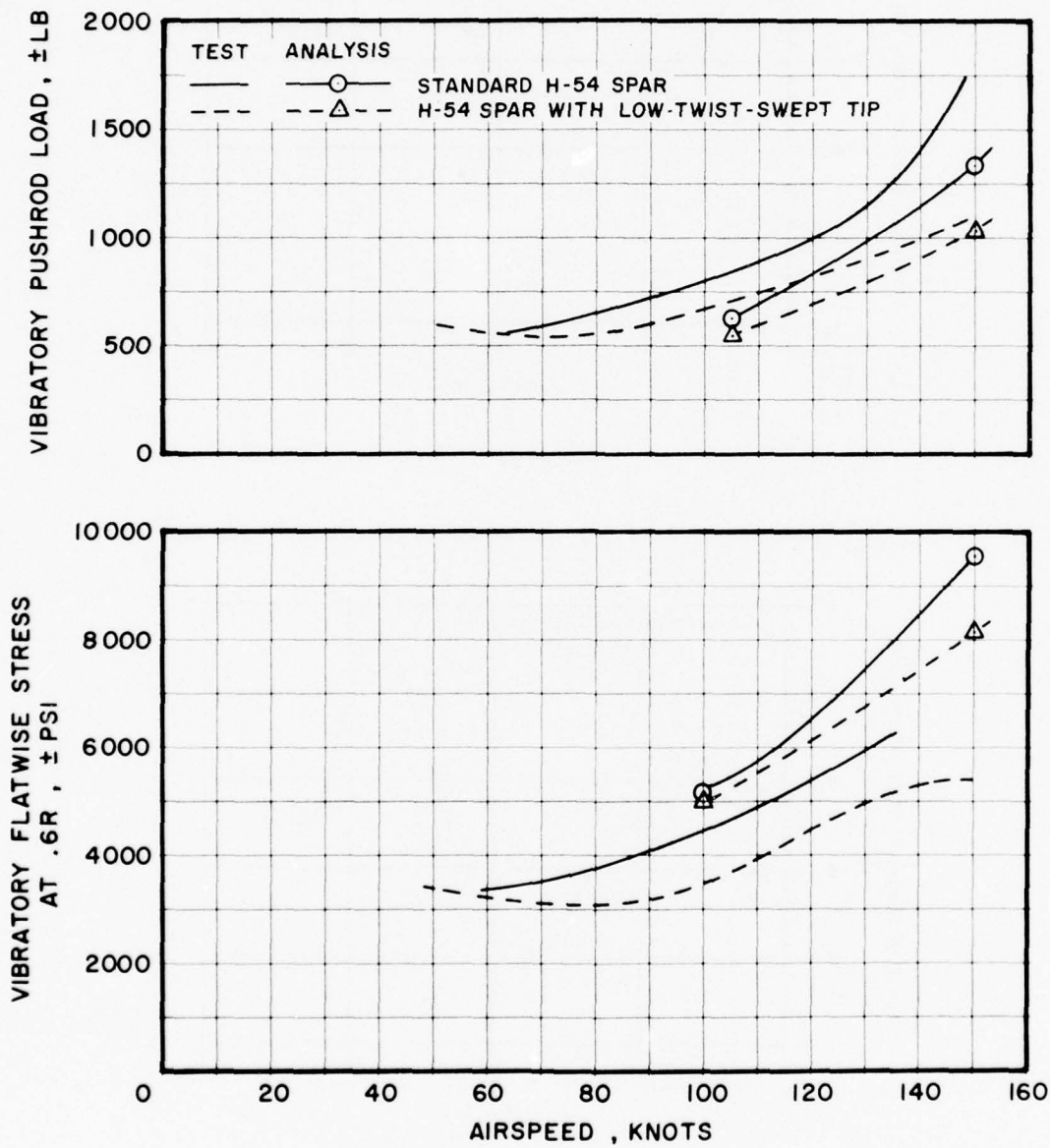


Figure 34. Measured and Calculated Buildup of H-54 Blade Pushrod Loads and Flatwise Stress at 42,000 lb Lift.

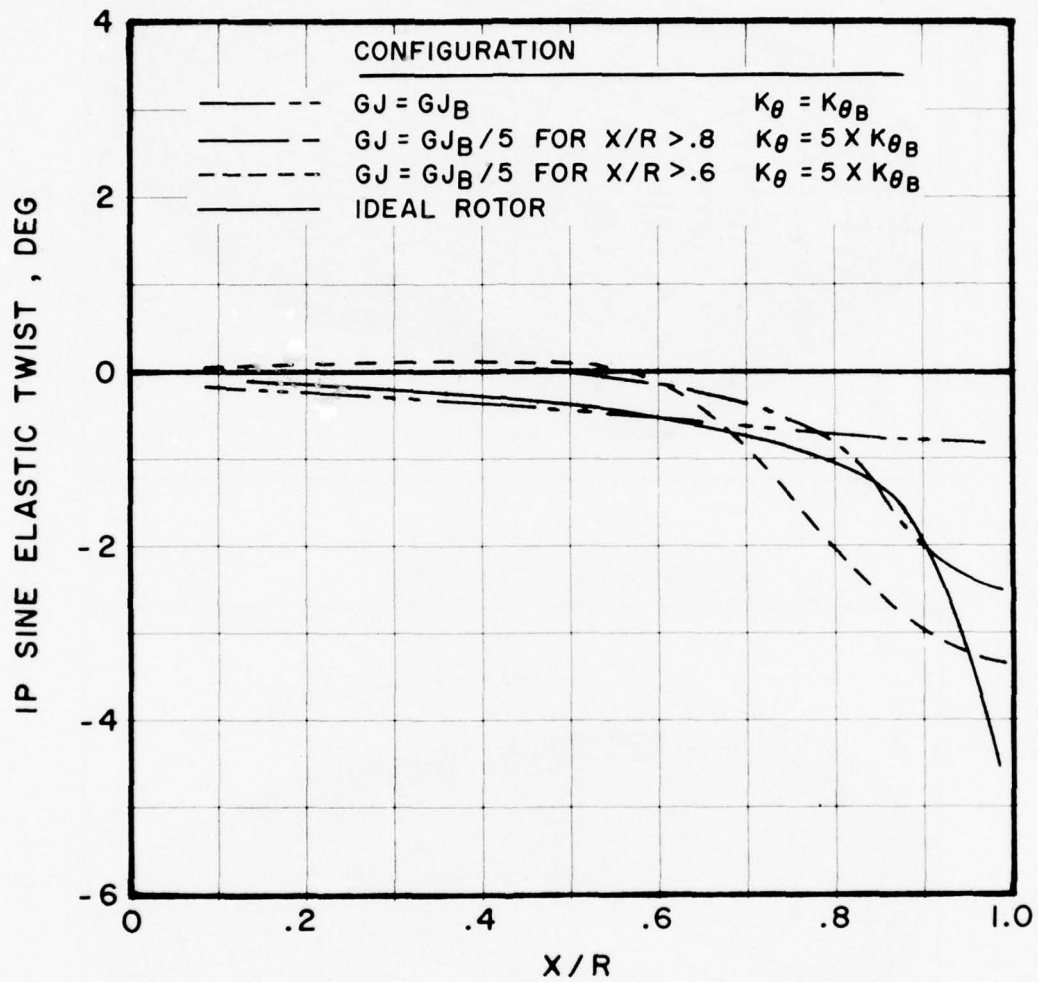


Figure 35. Variation of Blade Torsional Response Amplitude With Torsional Stiffness at $\mu=0.4$ and $C_L/\sigma=0.085$.

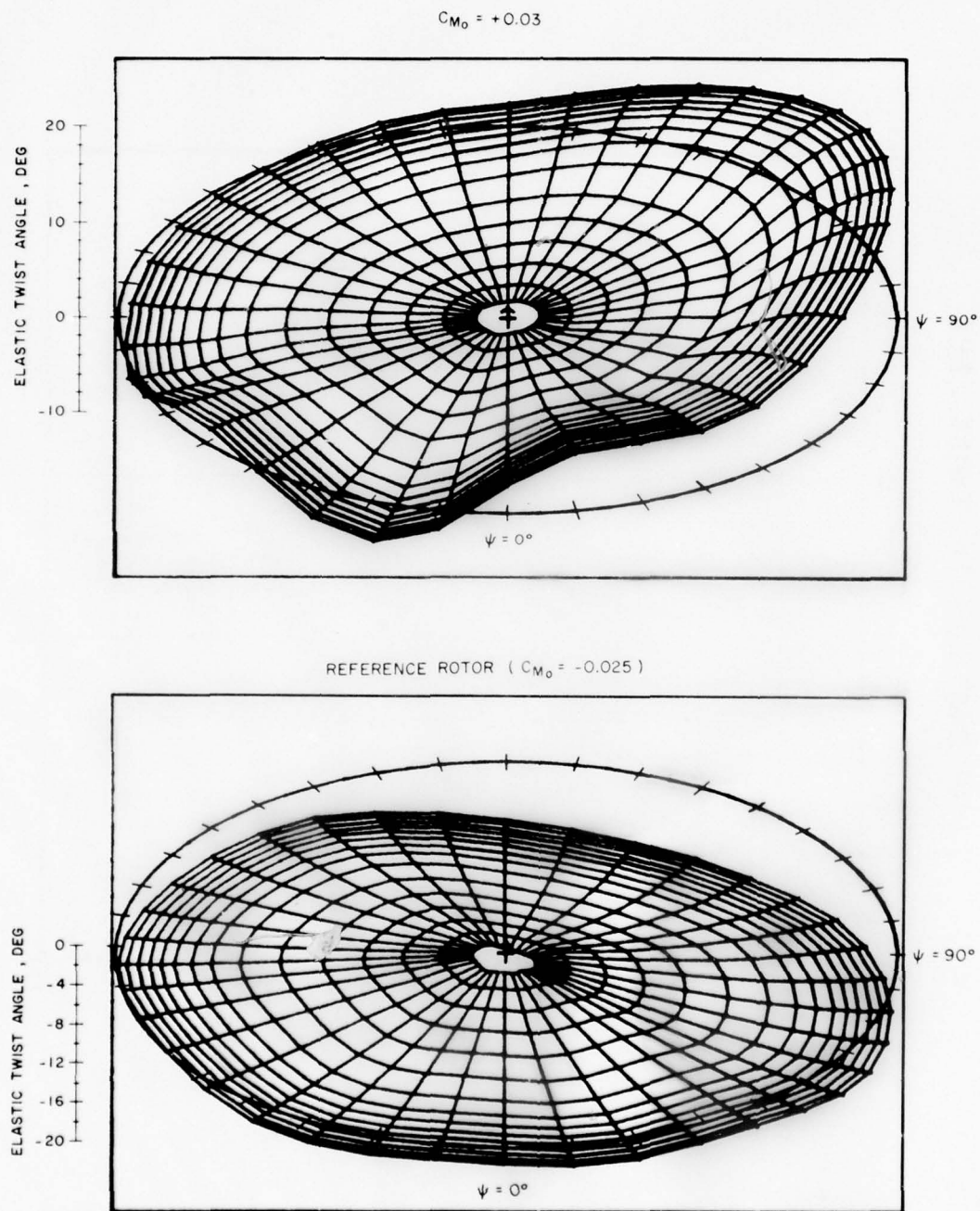


Figure 36. Effect of Negative Camber on the Distribution of Torsional Response at $\mu=0.4$ and $C_L/\sigma=0.085$.

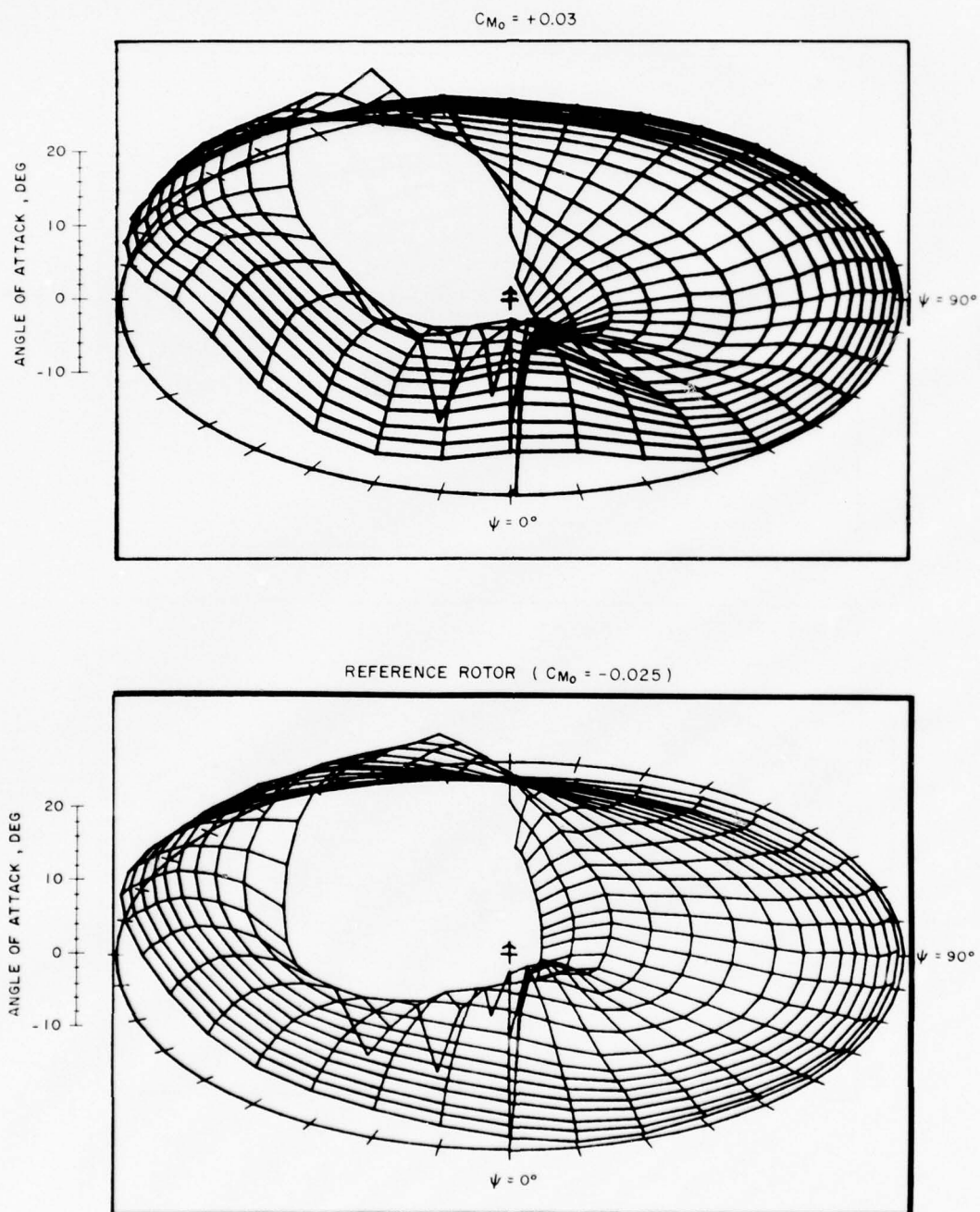


Figure 37. Effect of Negative Camber on the Distribution of Angle of Attack at $\mu=0.4$ and $C_L/C_0=0.085$.

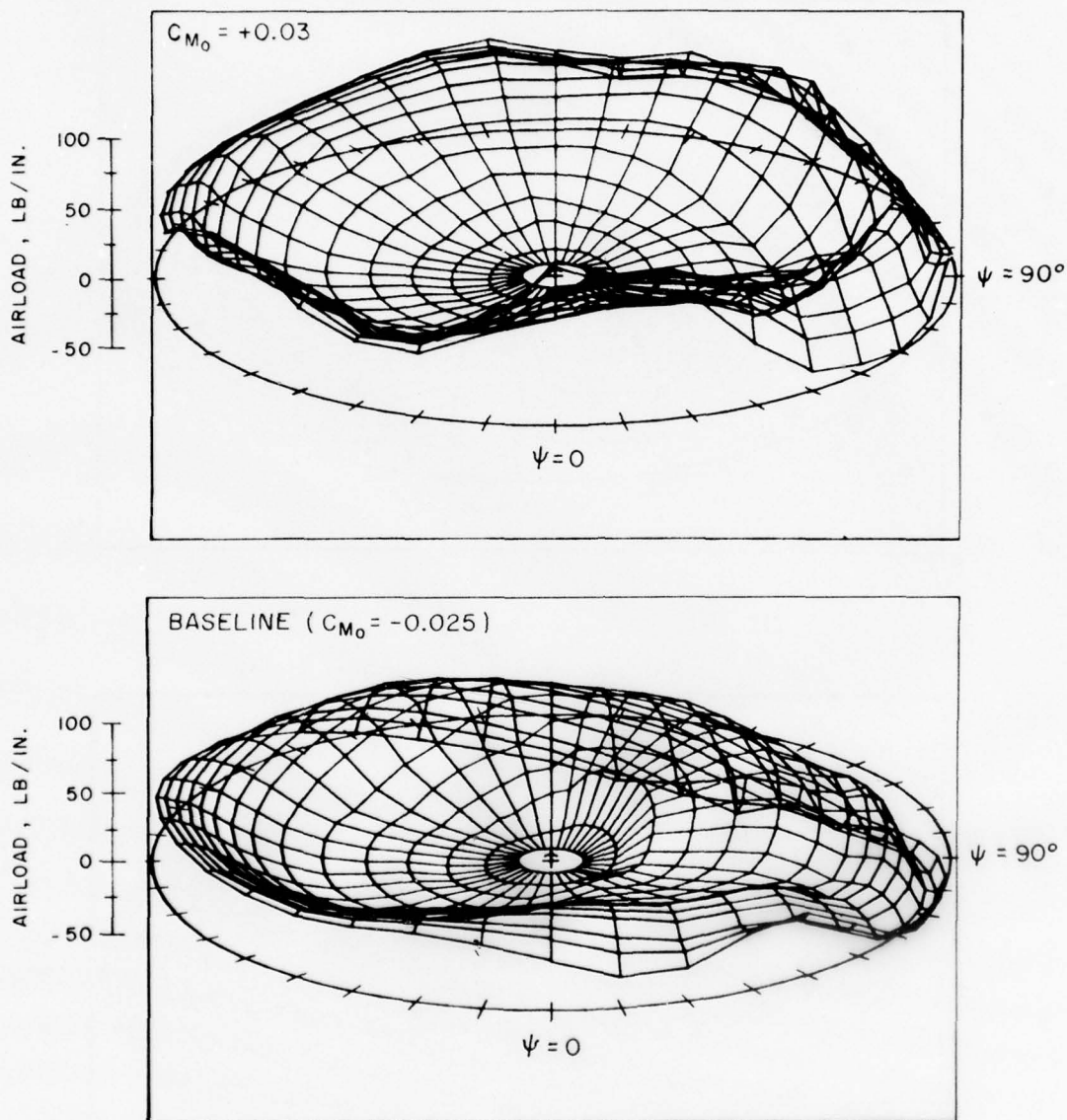
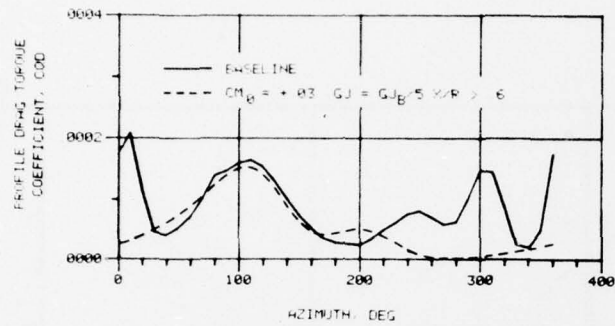
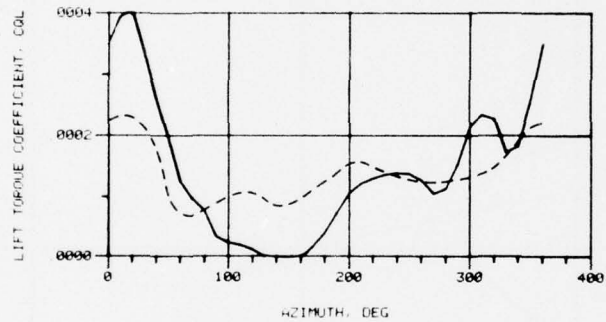


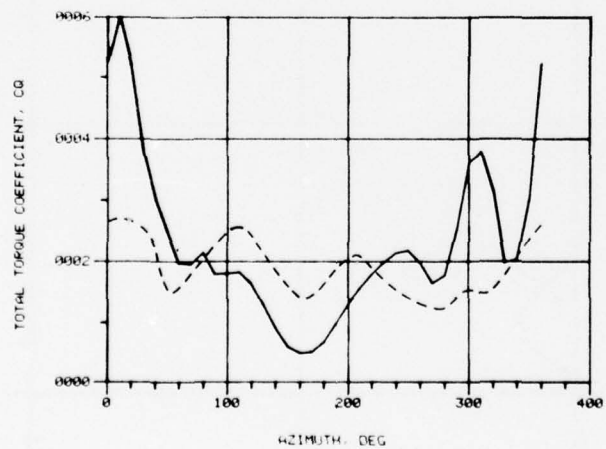
Figure 38. Effect of Negative Camber on the Distribution of Airloads at $\mu=0.4$ and $C_L/\sigma=0.085$.



(a)



(b)



(c)

Figure 39. Effect of Negative Camber on the Distribution of Blade Torque at $\mu=0.4$ and $C_L/\sigma=0.085$.

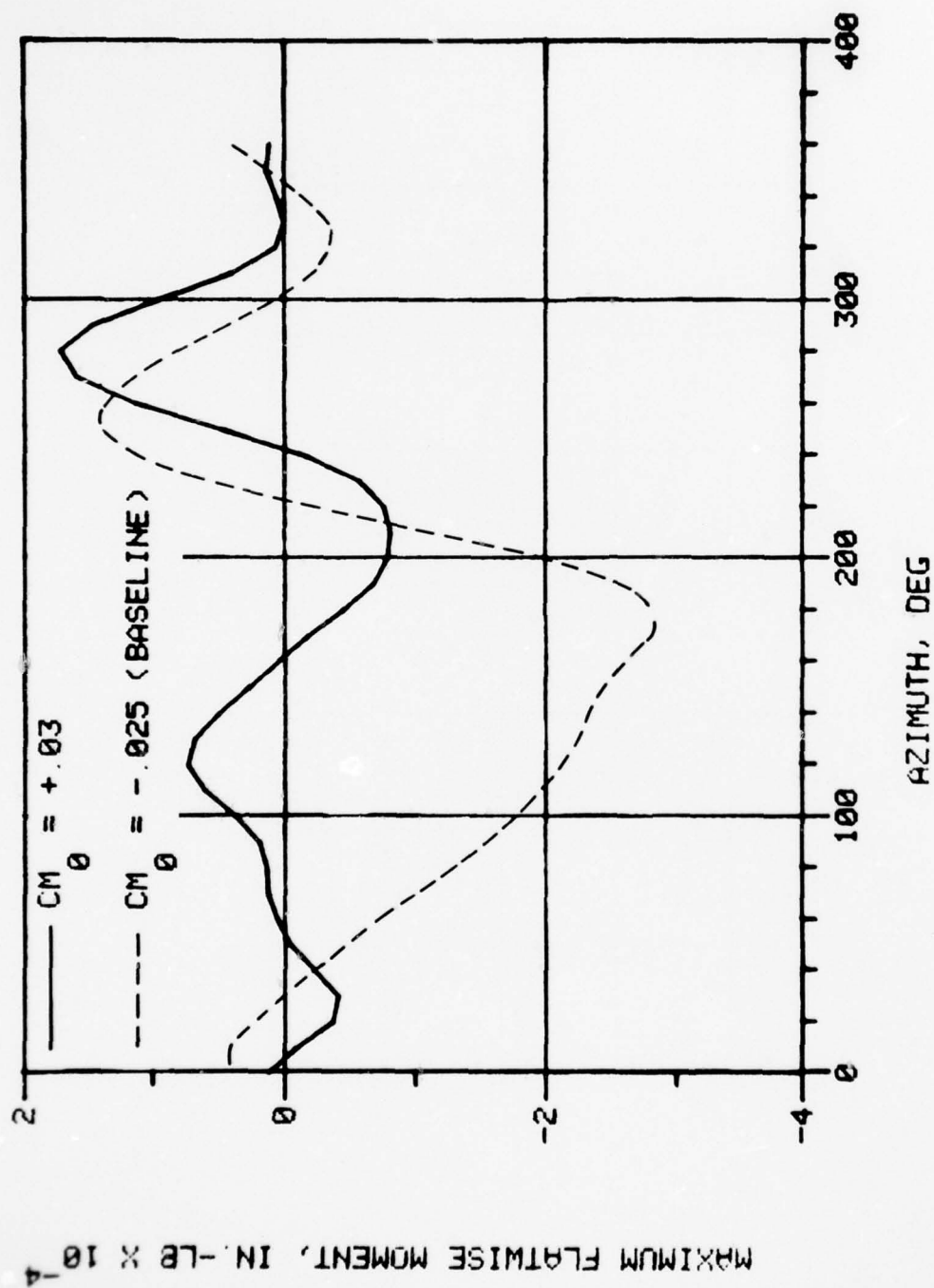
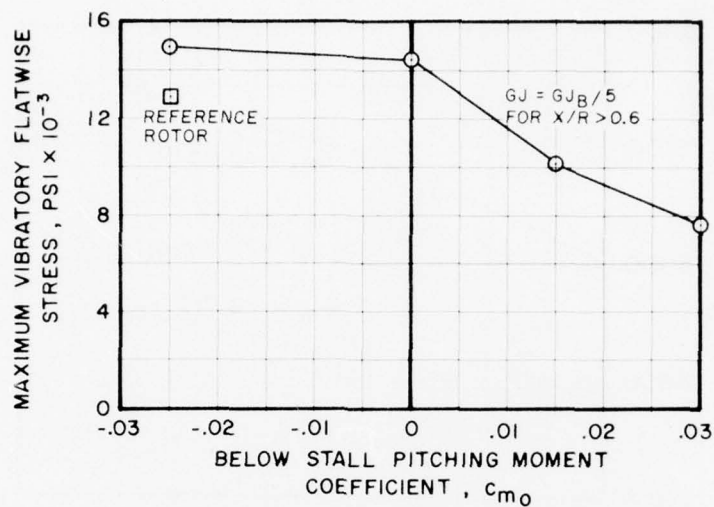
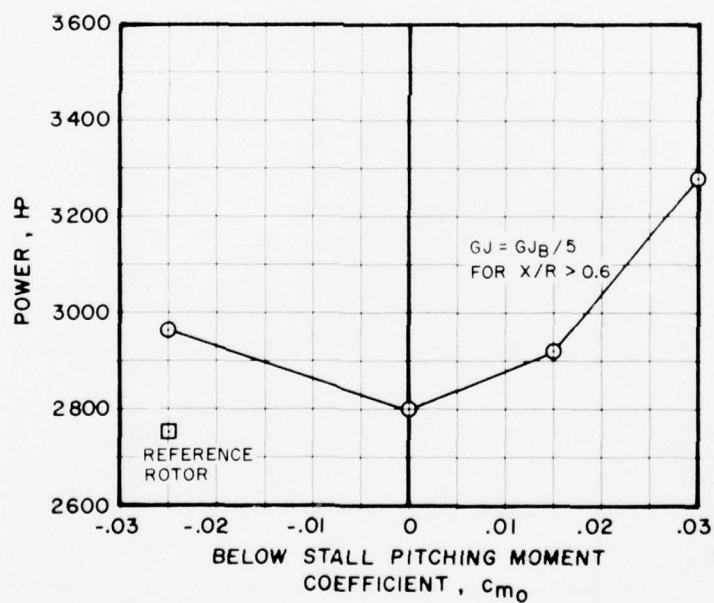


Figure 40. Effect of Negative Camber on Maximum Flatwise Stress at $\mu=0.4$ and $C_L/\sigma=0.085$.

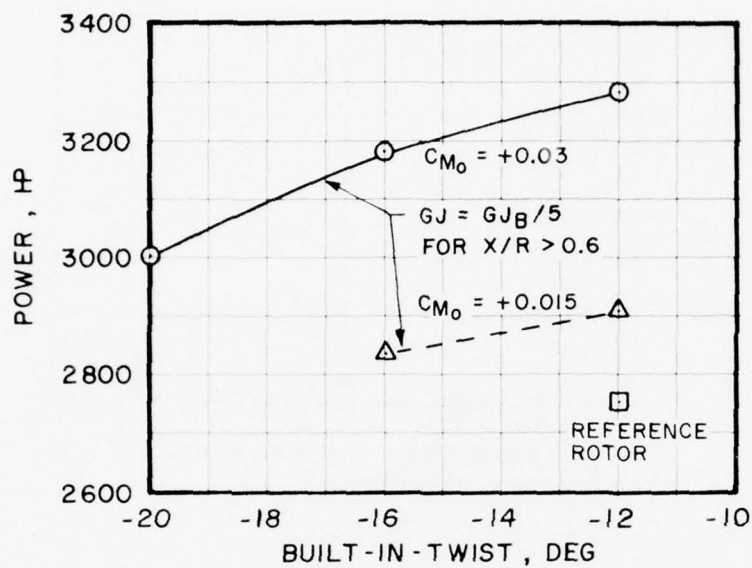


(a)

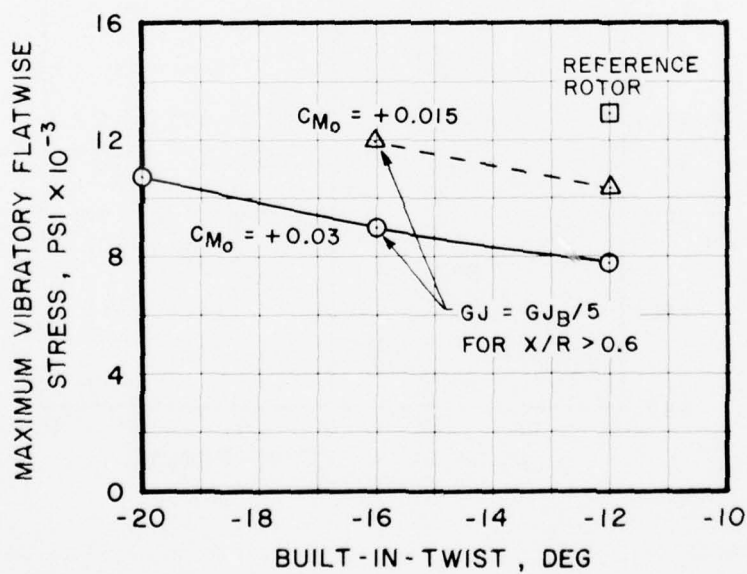


(b)

Figure 41. Variation of Flatwise Stress and Power With Pitching Moment Coefficient at $\mu=0.4$ and $C_L/\sigma=0.085$.



(a)



(b)

Figure 42. Variation of Power and Flatwise Stress With Built-In Twist Angle for $c_{m_0} = +0.015$ and $+0.03$.

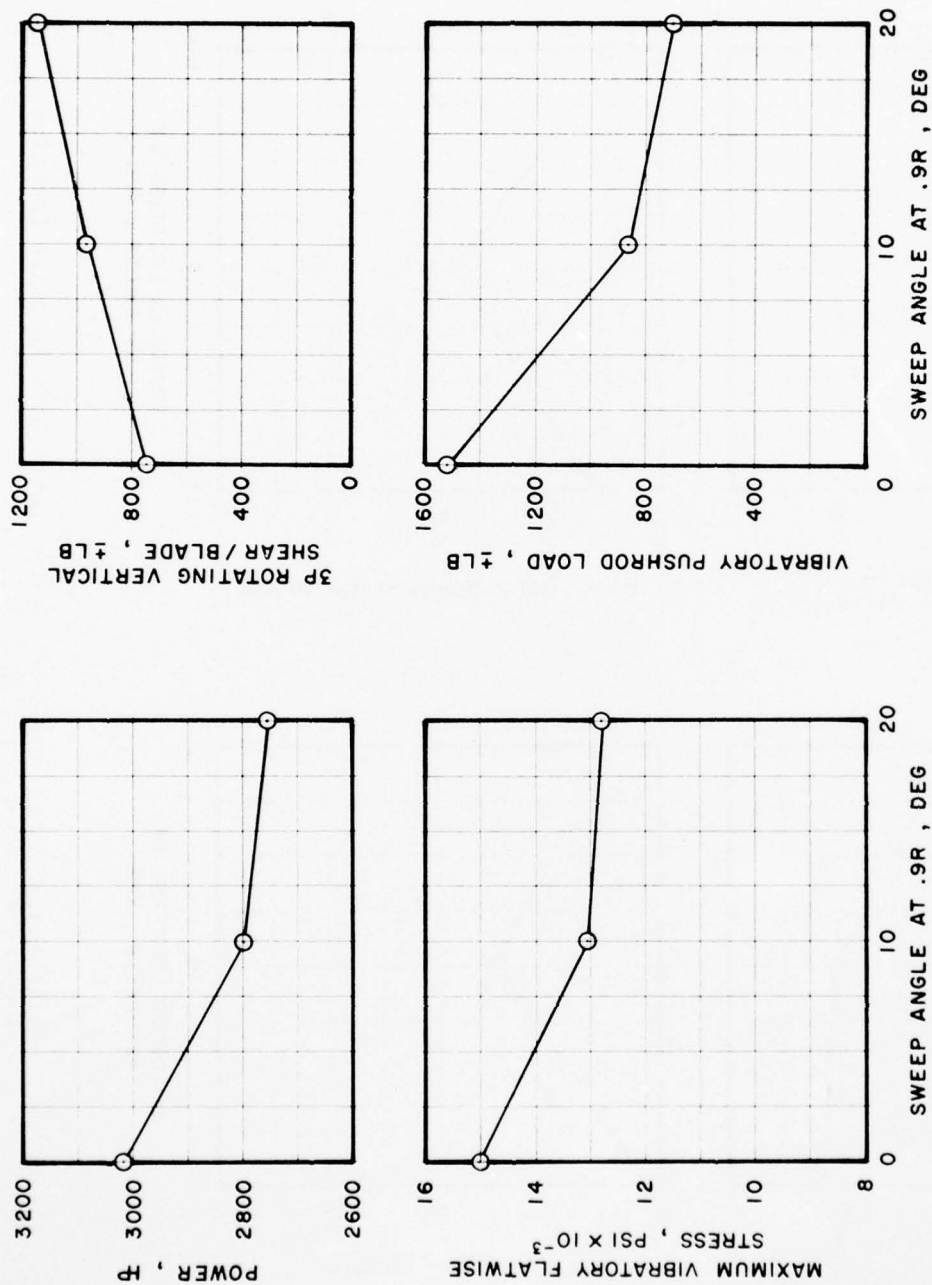


Figure 43. Variation of Power and Rotor System Loads With Sweep Angle at $\mu=0.4$ and $C_L/c=0.085$.

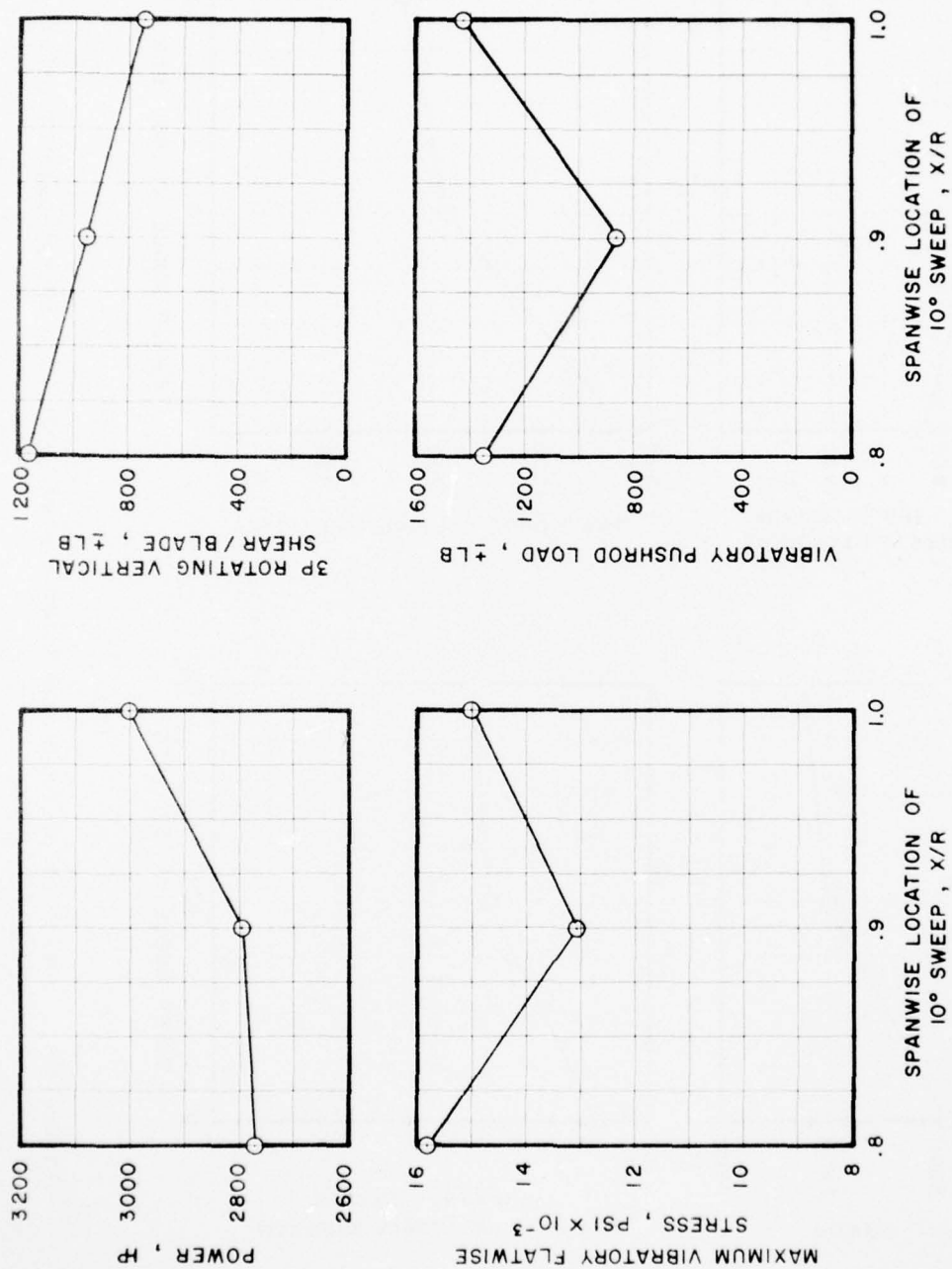
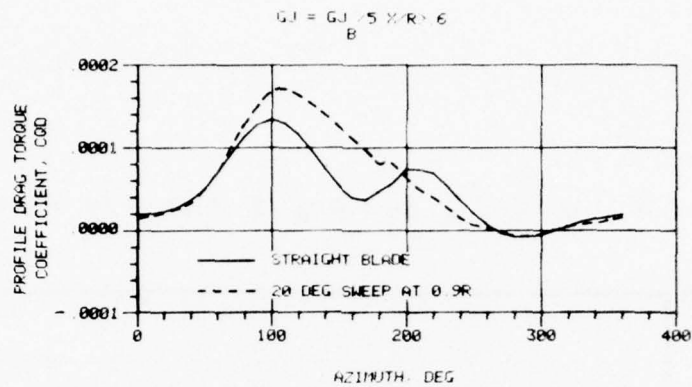
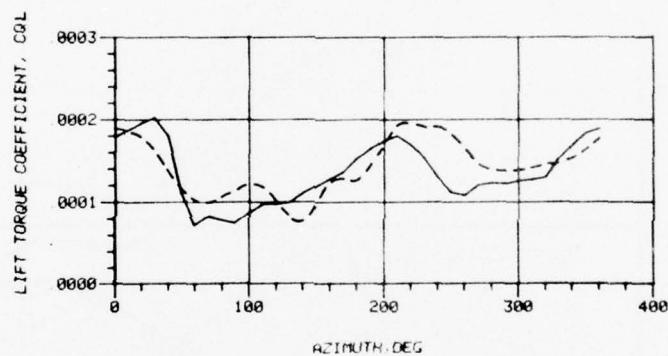


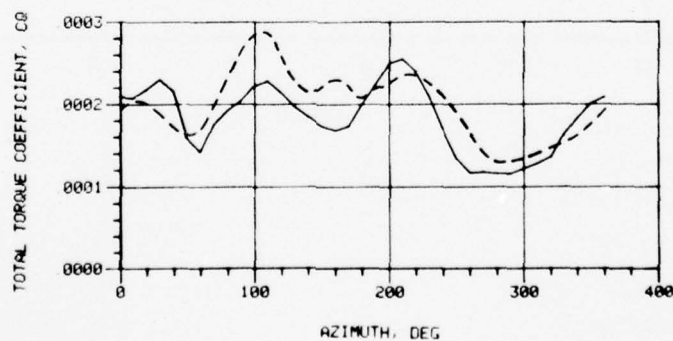
Figure 44. Variation of Power and Rotor System Loads With Spanwise Location of Sweep at $\mu=0.4$ and $C_L/\sigma=0.085$.



(a)



(b)



(c)

Figure 45. Effect of Sweep on the Distribution of Blade Torque at $\mu=0.4$ and $C_L/\sigma=0.085$.

$\mu = 0.4$, $\psi = 90^\circ$, $GJ = GJ_B / 5$ FOR $X/R > 0.6$

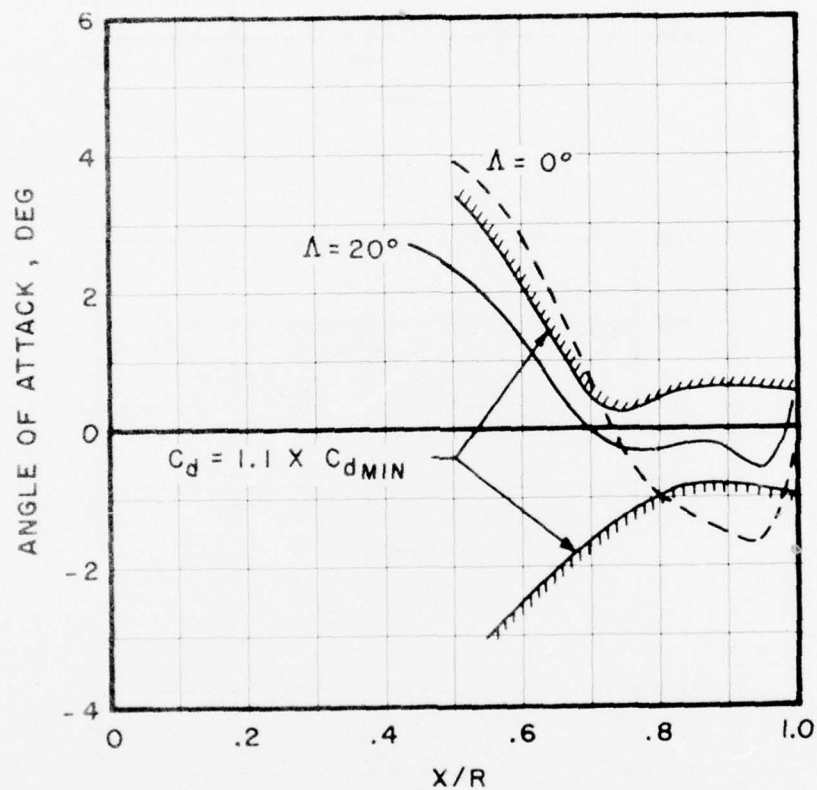


Figure 46. Reduction of Advancing Blade Drag Torque With Swept Tip Compliant Rotor.

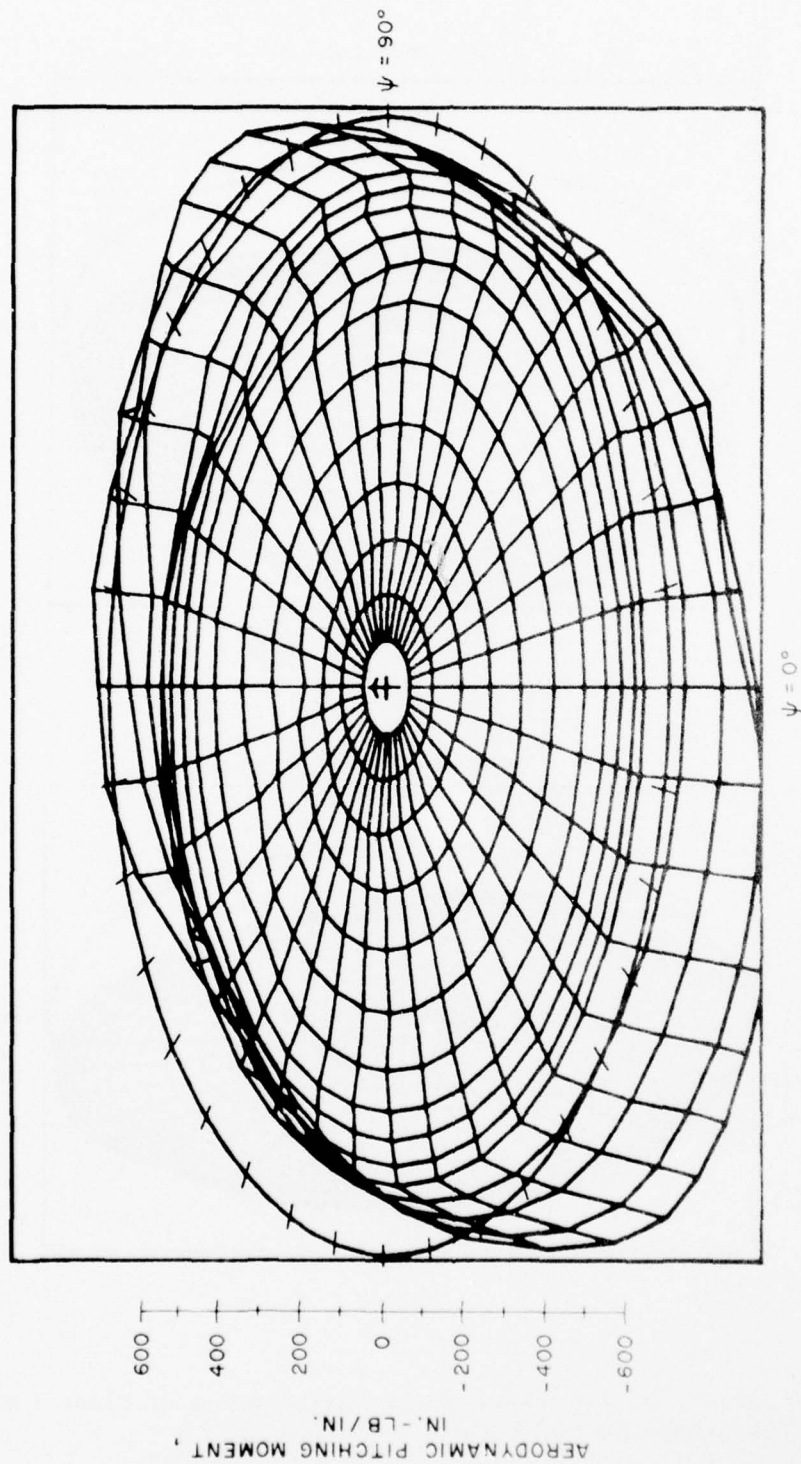


Figure 47. Aerodynamic Pitching Moment of Swept Tip Compliant Rotor at $\mu=0.4$ and $C_L/\sigma=0.085$.

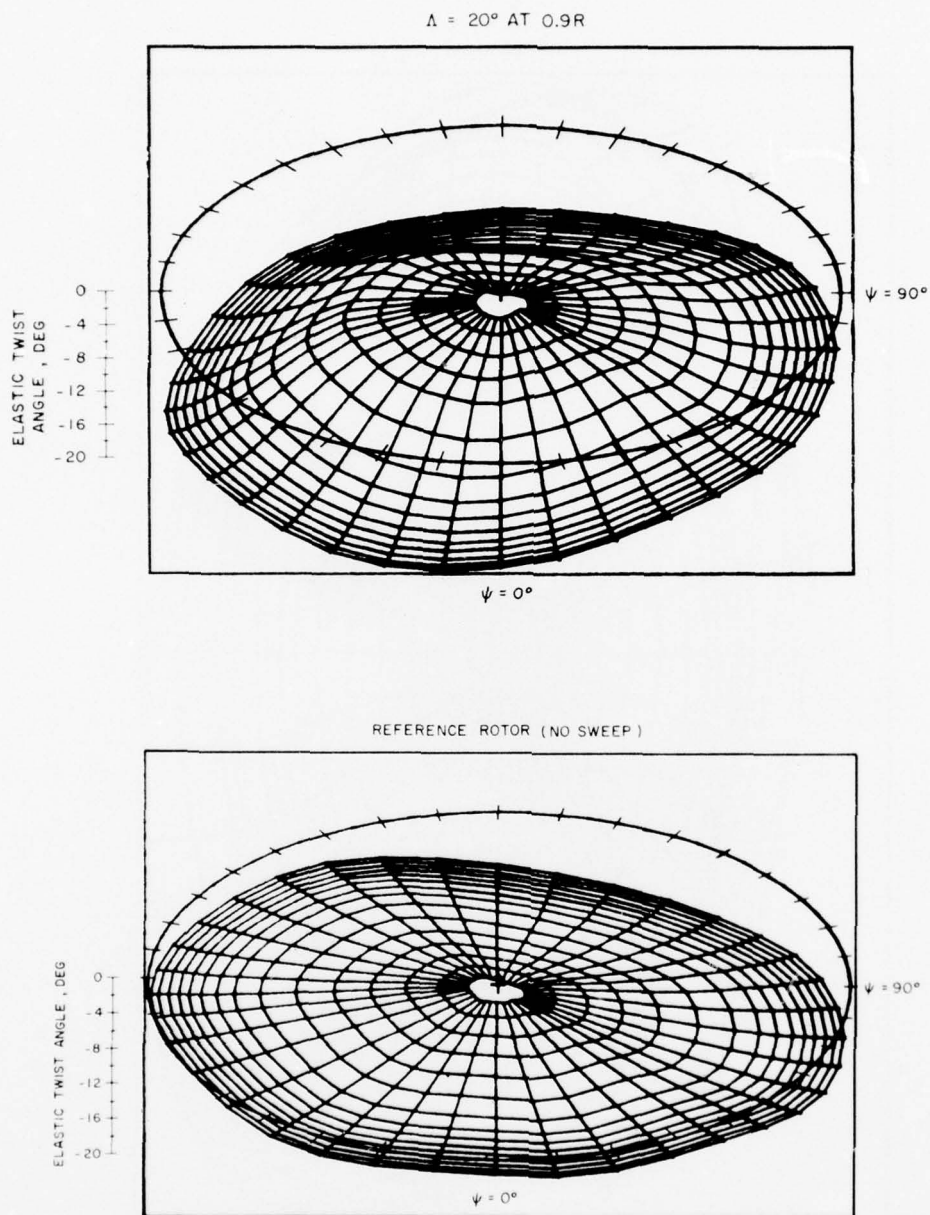


Figure 48. Effect of Tip Sweep on the Distribution of Blade Torsional Response at $\mu=0.4$ and $C_L/\sigma=0.085$.

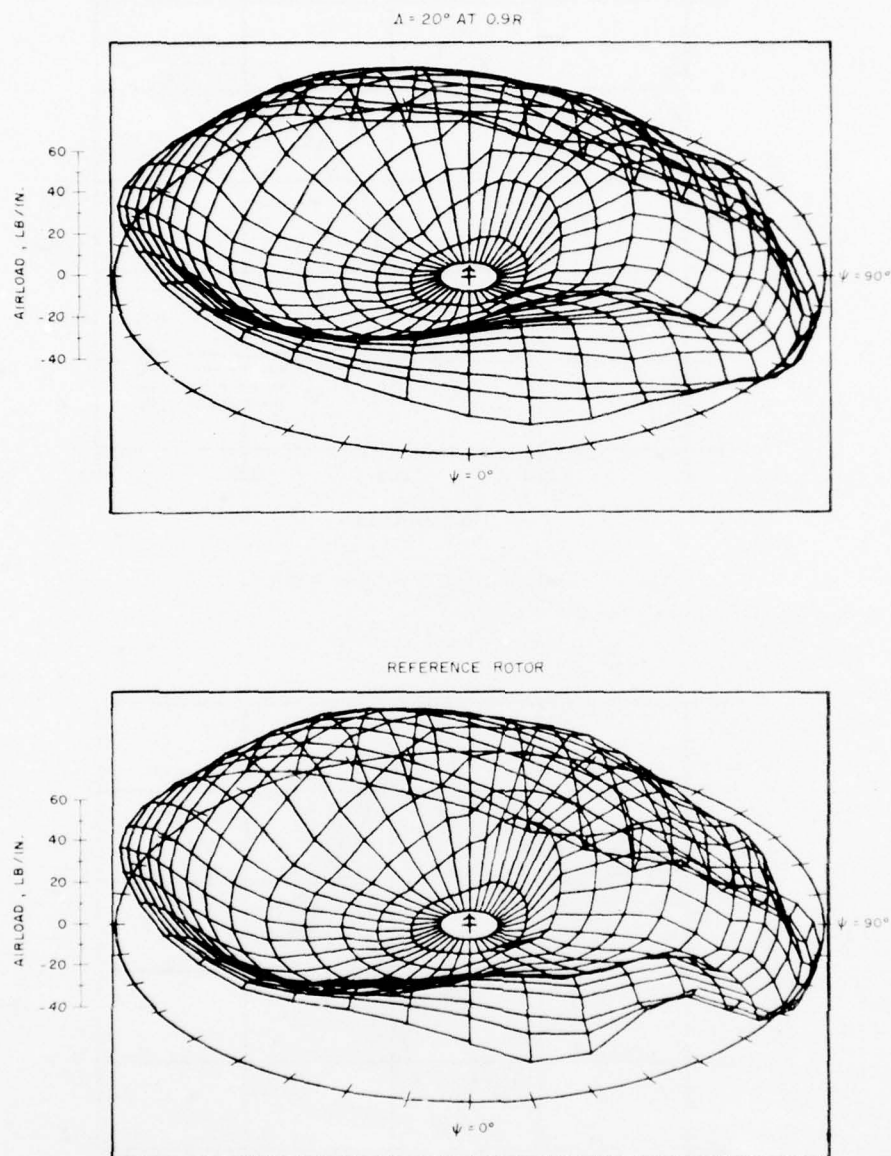
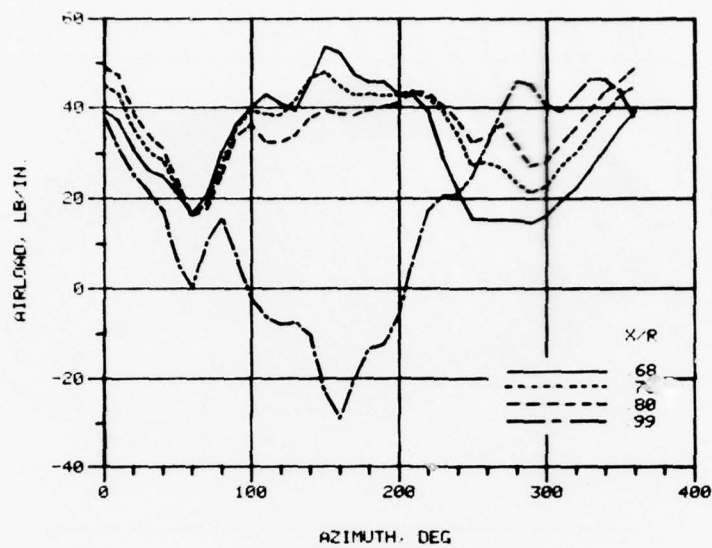
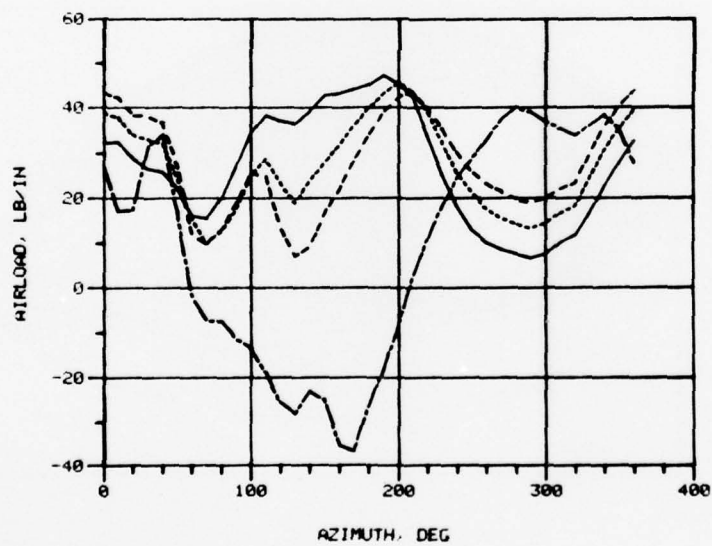


Figure 49. Effect of Tip Sweep on the Distribution of Airloads at $\mu=0.4$ and $C_L/\sigma=0.085$.

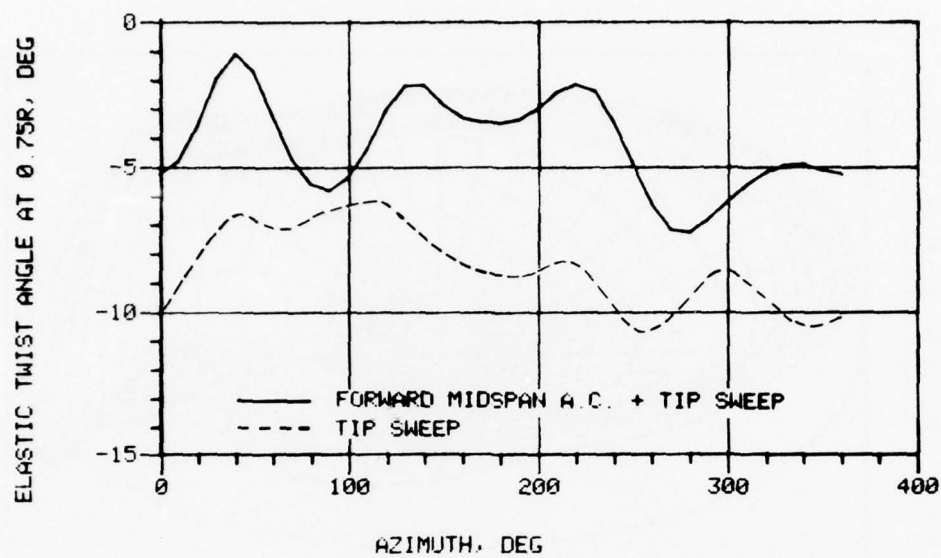


(a) $\mu = 0.3$, $C_L/\sigma = 0.10$

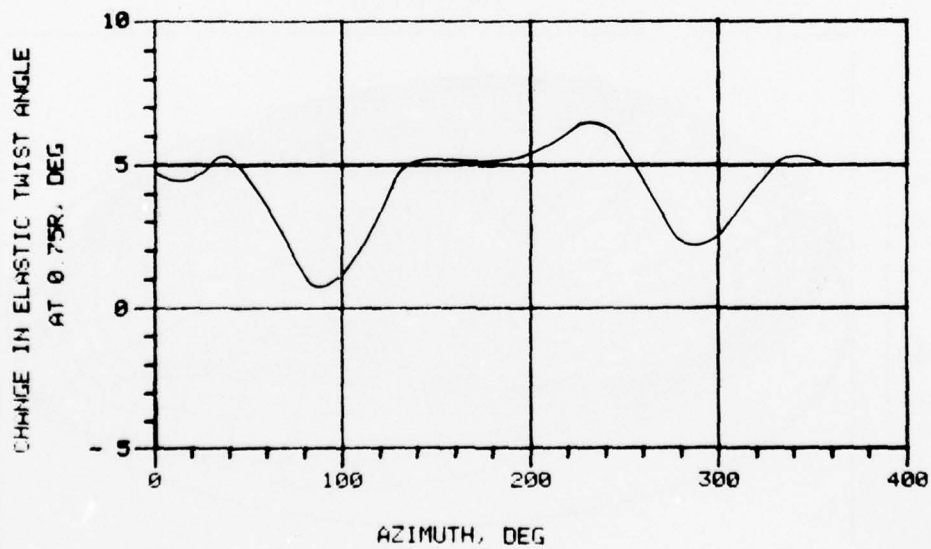


(b) $\mu = 0.4$, $C_L/\sigma = 0.085$

Figure 50. Reference Rotor Airload Time Histories.



(a)



(b)

Figure 51. Effect of Forward Midspan Aerodynamic Center on Elastic Twist at $\mu=0.4$ and $C_L/\sigma=0.085$.

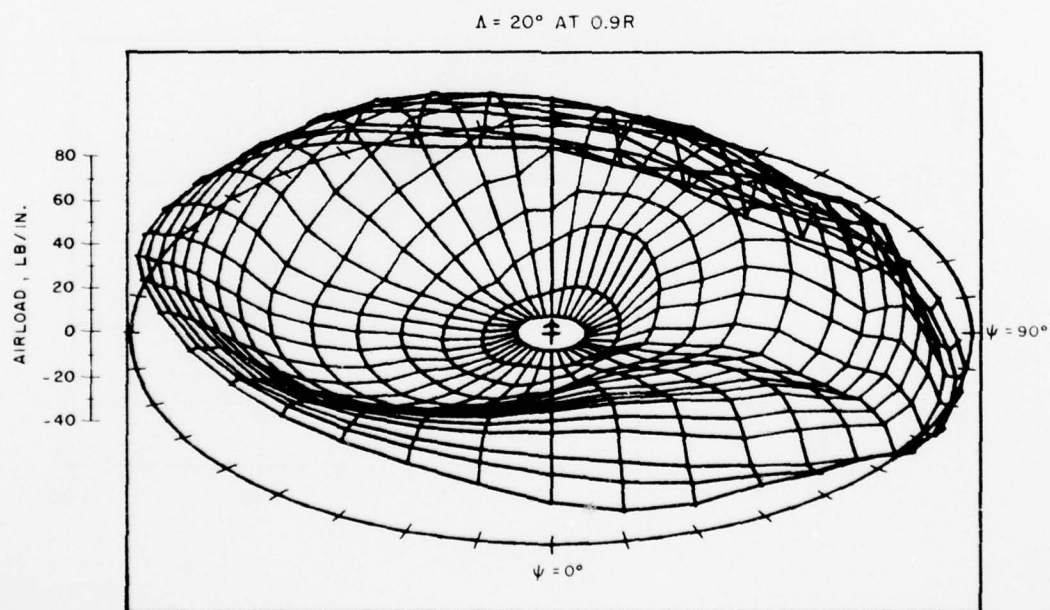
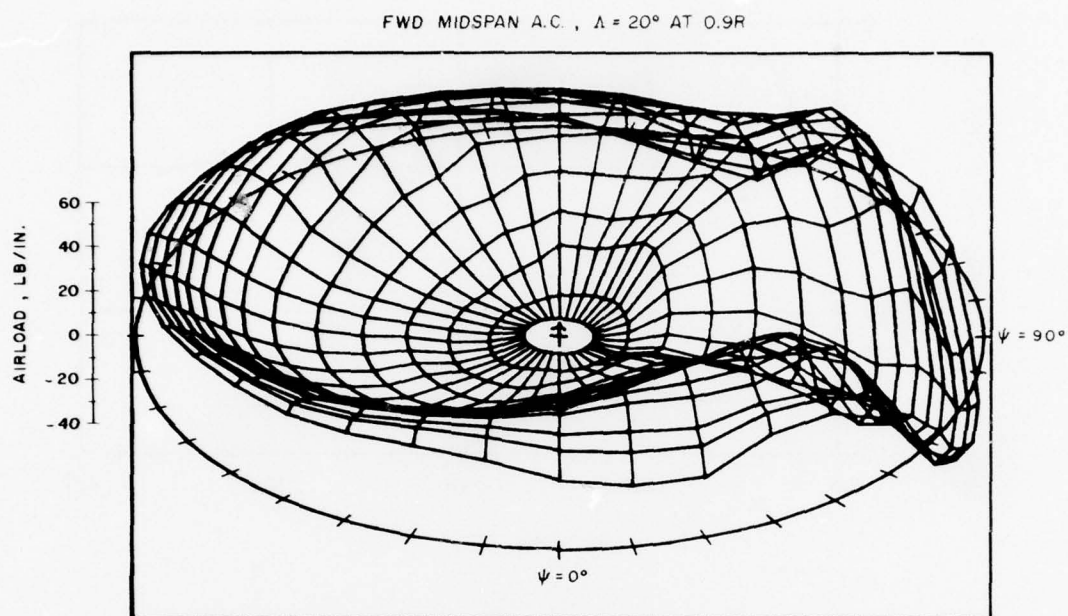
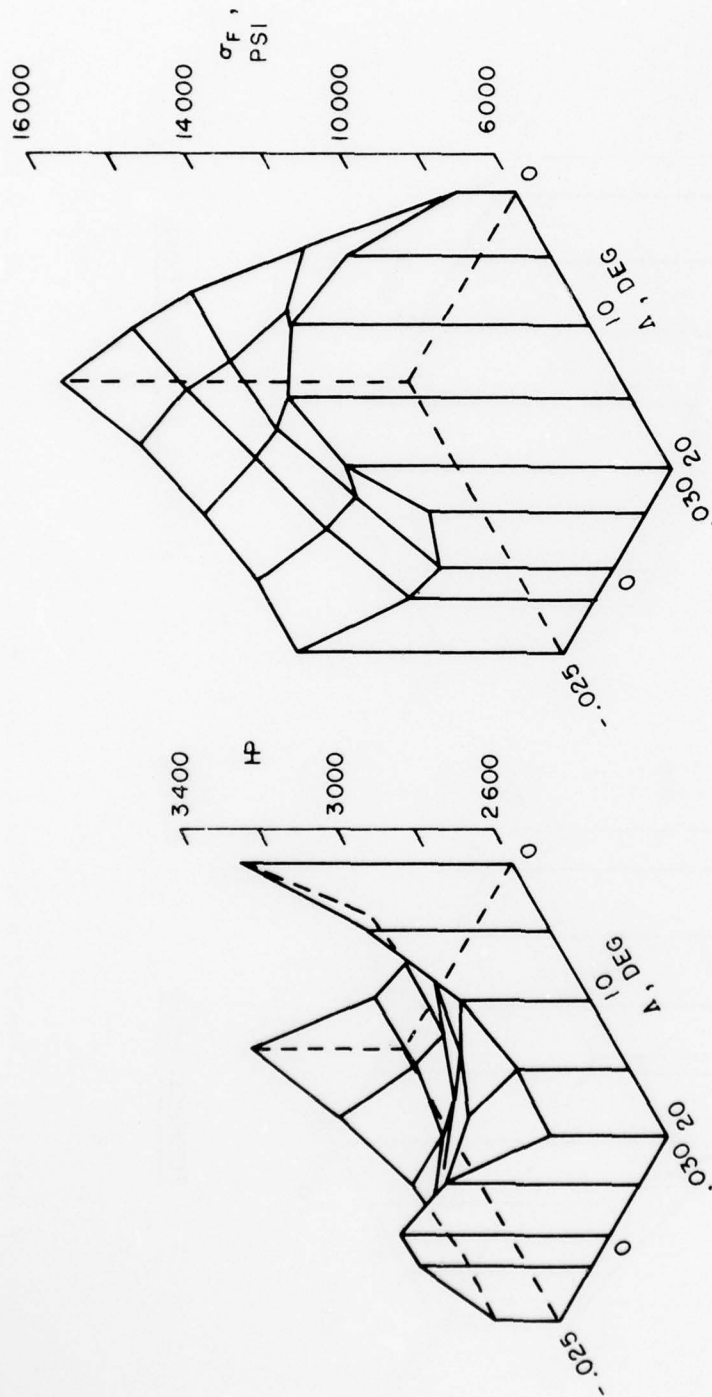


Figure 52. Effect of Forward Midspan Aerodynamic Center on the Distribution of Airload at $\mu=0.4$ and $C_L/\sigma=0.085$.



FLATWISE STRESS

POWER REQUIRED

Figure 53. Variation of Required Power and Flatwise Stress With Tip Sweep and Camber at $\mu=0.4$ and $C_L/\sigma=0.085$.

AD-A042 338

UNITED TECHNOLOGIES CORP STRATFORD CONN SIKORSKY AIR--ETC F/G 1/3
INVESTIGATION OF THE COMPLIANT ROTOR CONCEPT.(U)

JUN 77 R H BLACKWELL

DAAJ02-76-C-0003

UNCLASSIFIED

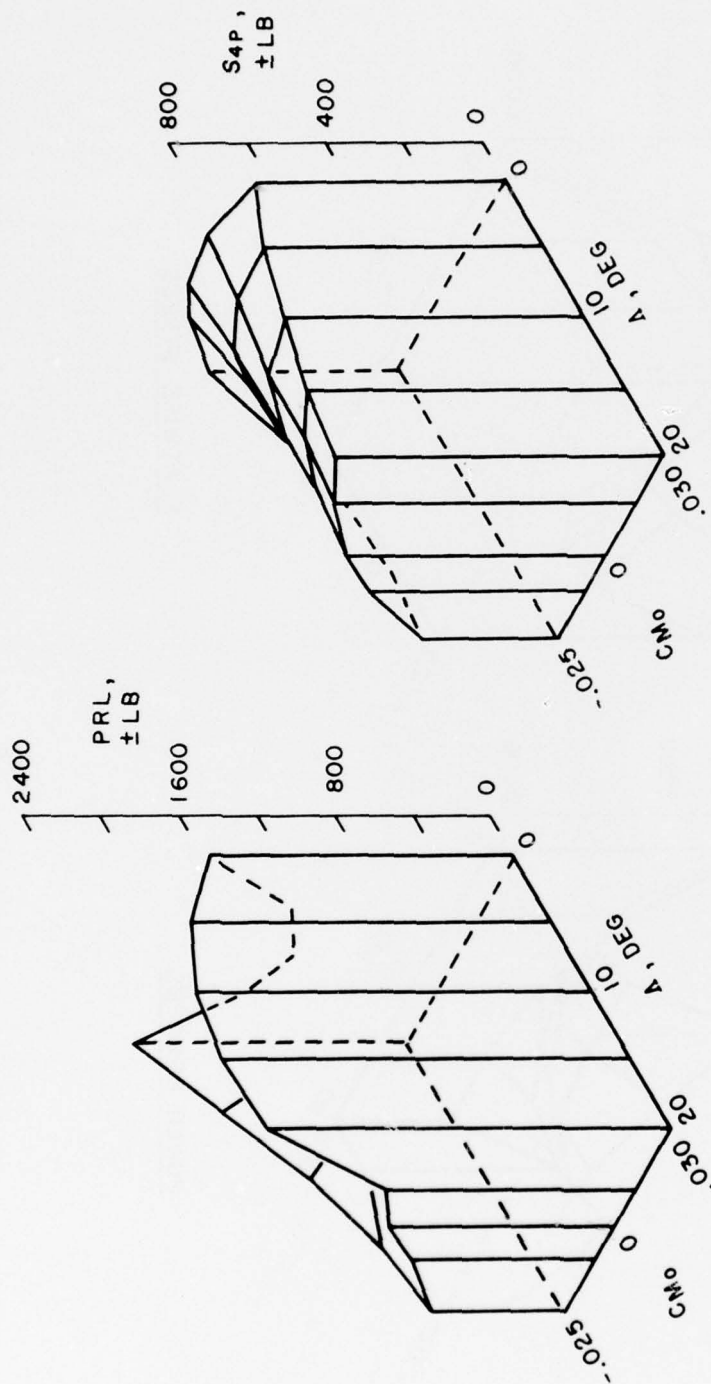
SER-50985

USAAMRDL-TR-77-7

NL

2 OF 2
ADA042338

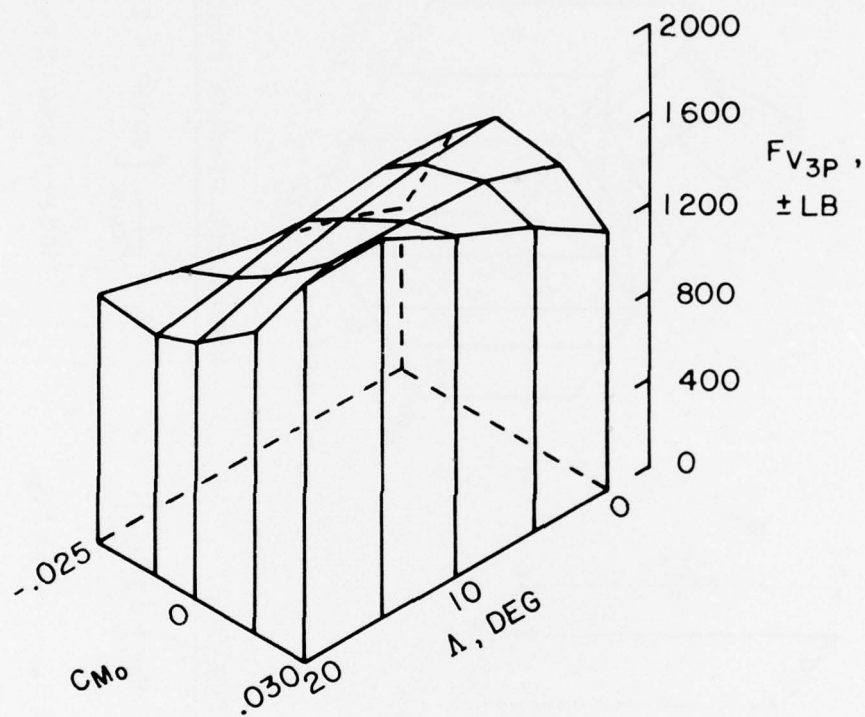




PUSHROD LOAD

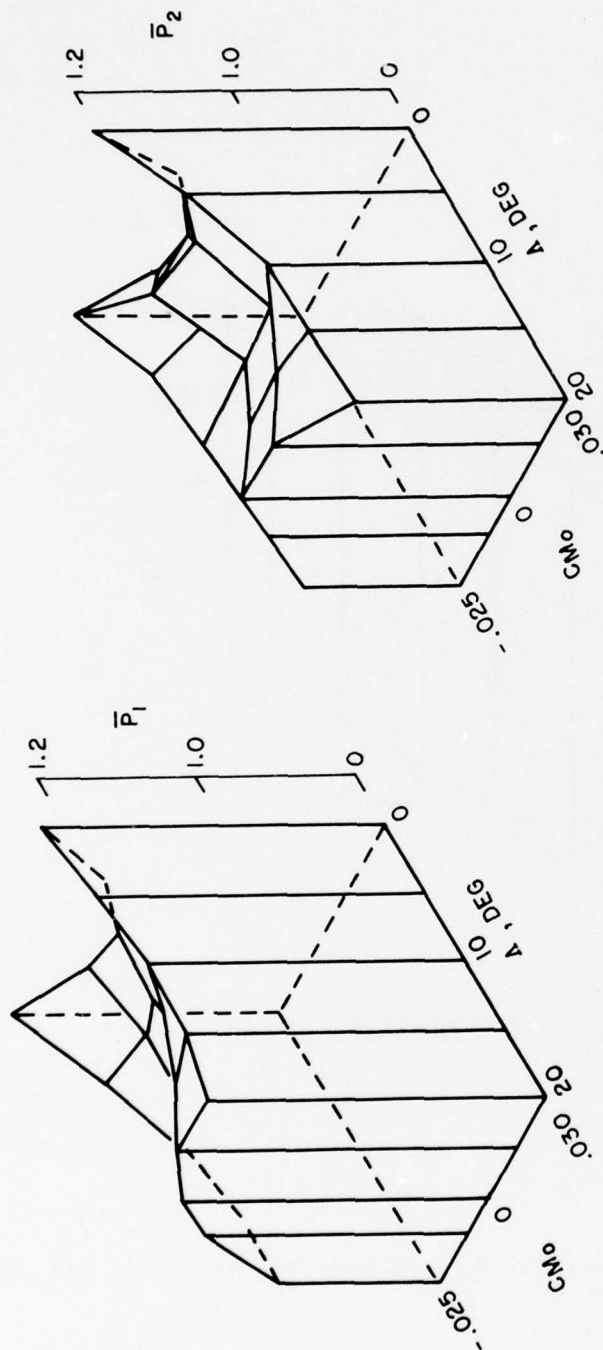
AVERAGE 4P SERVO LOAD

Figure 54. Variation of Control Loads With Tip Sweep and Camber at $\mu=0.4$ and $C_L/\sigma=0.085$.



3P ROTATING VERTICAL SHEAR

Figure 55. Variation of 3P Vertical Hinge Force With Tip Sweep and Camber at $\mu=0.4$ and $C_L/\sigma=0.085$.



NORMALIZED PENALTY FUNCTION \bar{P}_1

$$\bar{P}_1 = \frac{1}{P_{1MIN}} \left[60 \times HP + \sigma_F + 10PRL + 40S_{4P} + 5 \times F_{V3P} \right]$$

100 HP : 6000 PSI σ_F : 600 LB PRL : 150 LB S_{4P} : 1200 LB F_{V3P}

(a)

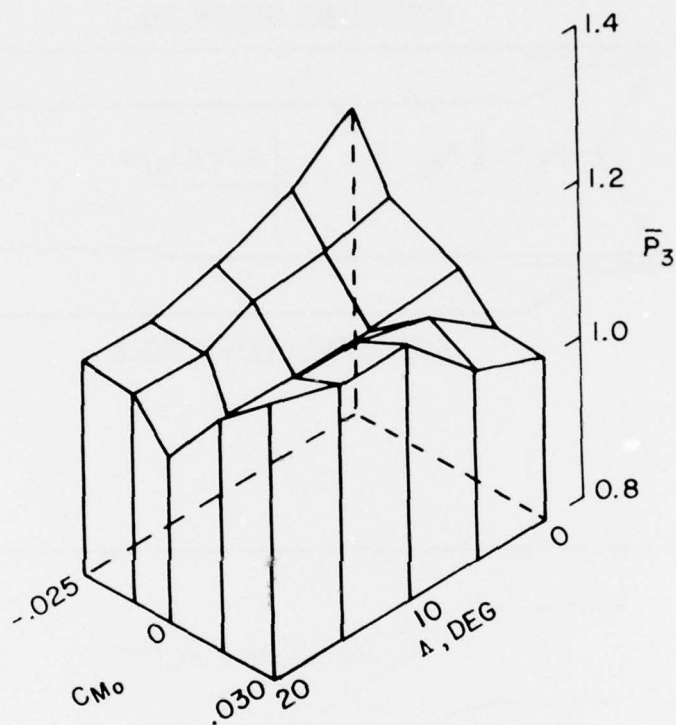
NORMALIZED PENALTY FUNCTION \bar{P}_2

$$\bar{P}_2 = \frac{1}{P_{2MIN}} \left[60 \times HP + 2 \times F_{V3P} \right]$$

100 HP : 3000 LB F_{V3P}

(b)

Figure 56. Penalty Functions Illustrating the Effects of Tip Sweep and Camber.



NORMALIZED PENALTY FUNCTION \bar{P}_3

$$\bar{P}_3 = \frac{1}{P_{3\text{MIN}}} [60 \times \text{HP} + 10 \sigma_F]$$

$$100 \text{ HP} : 600 \text{ PSI } \sigma_F$$

(c)

Figure 56. Concluded.

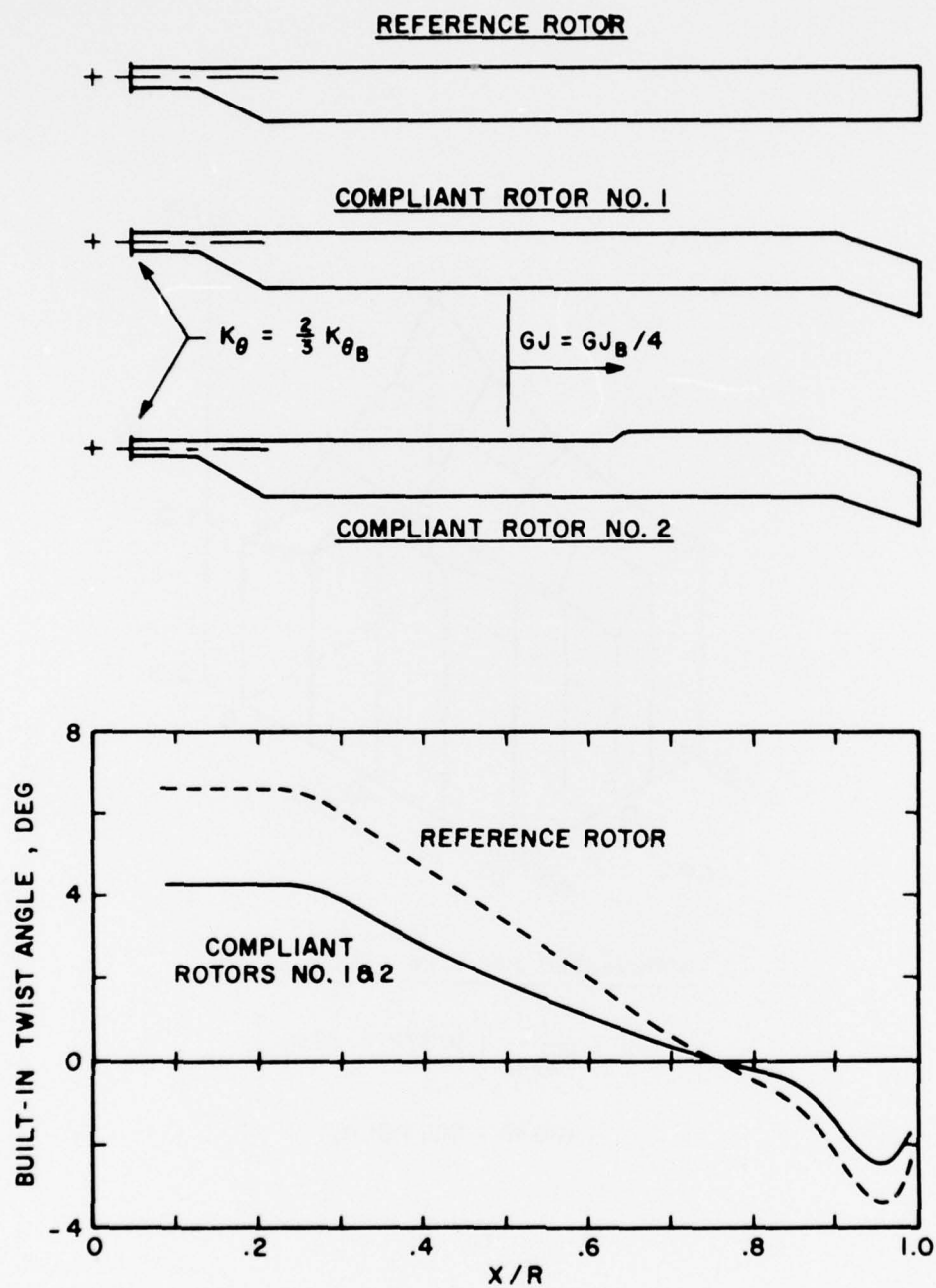


Figure 57. Compliant Rotor Designs.

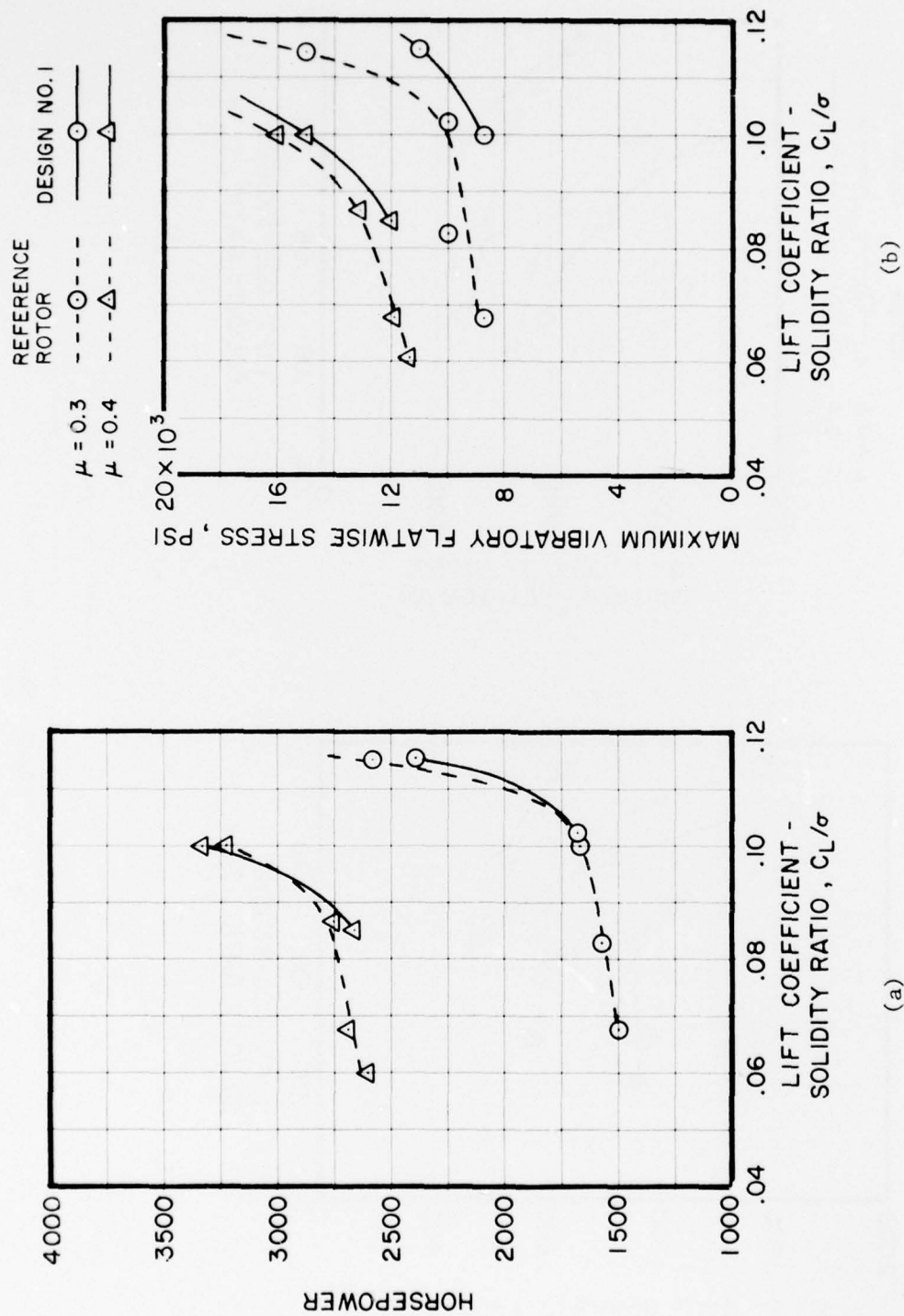


Figure 58. The Buildup of Power, Stress, Control Loads, and Vibratory Shear Force for Compliant Rotor Design #1 and Reference Rotor.

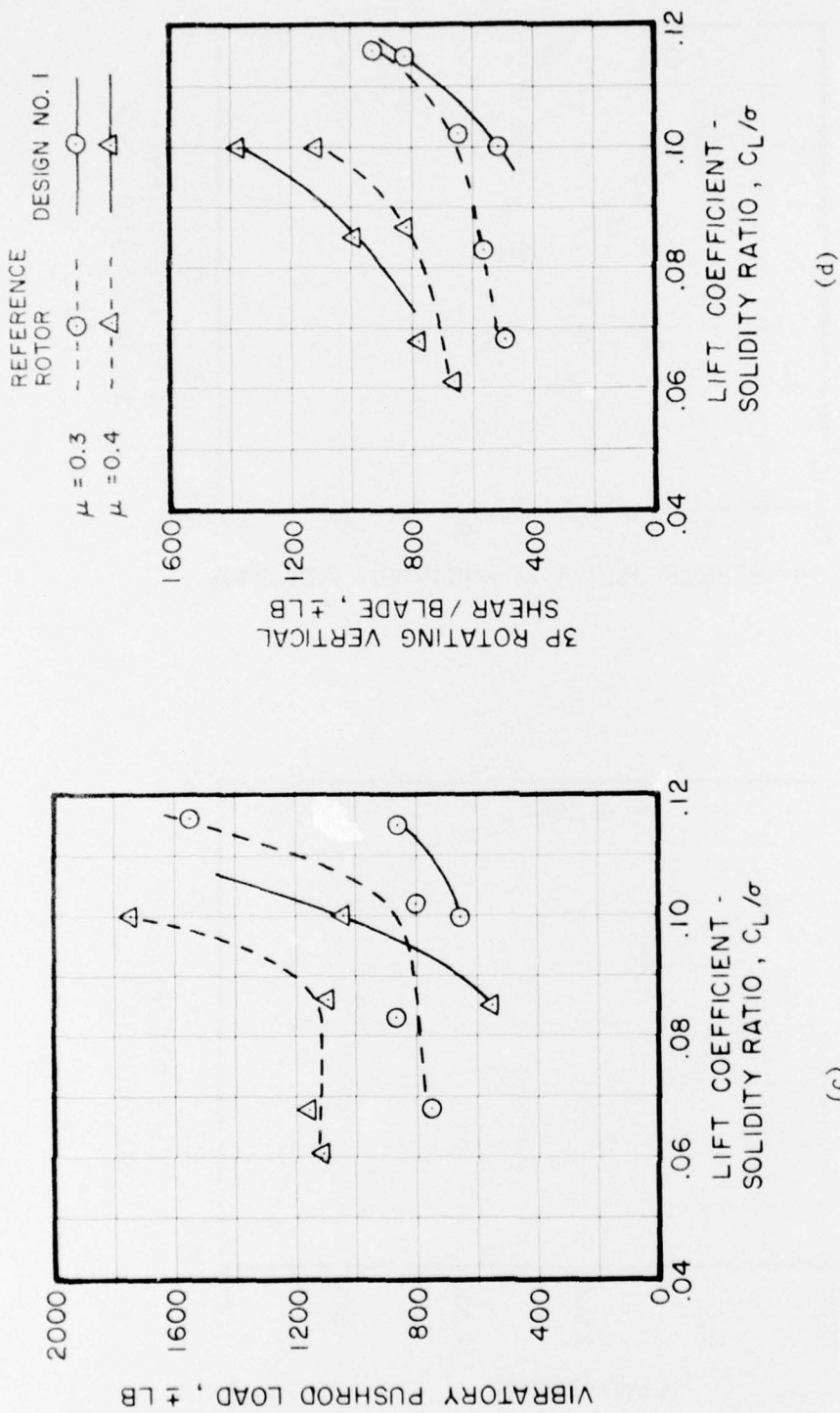


Figure 58. Concluded.

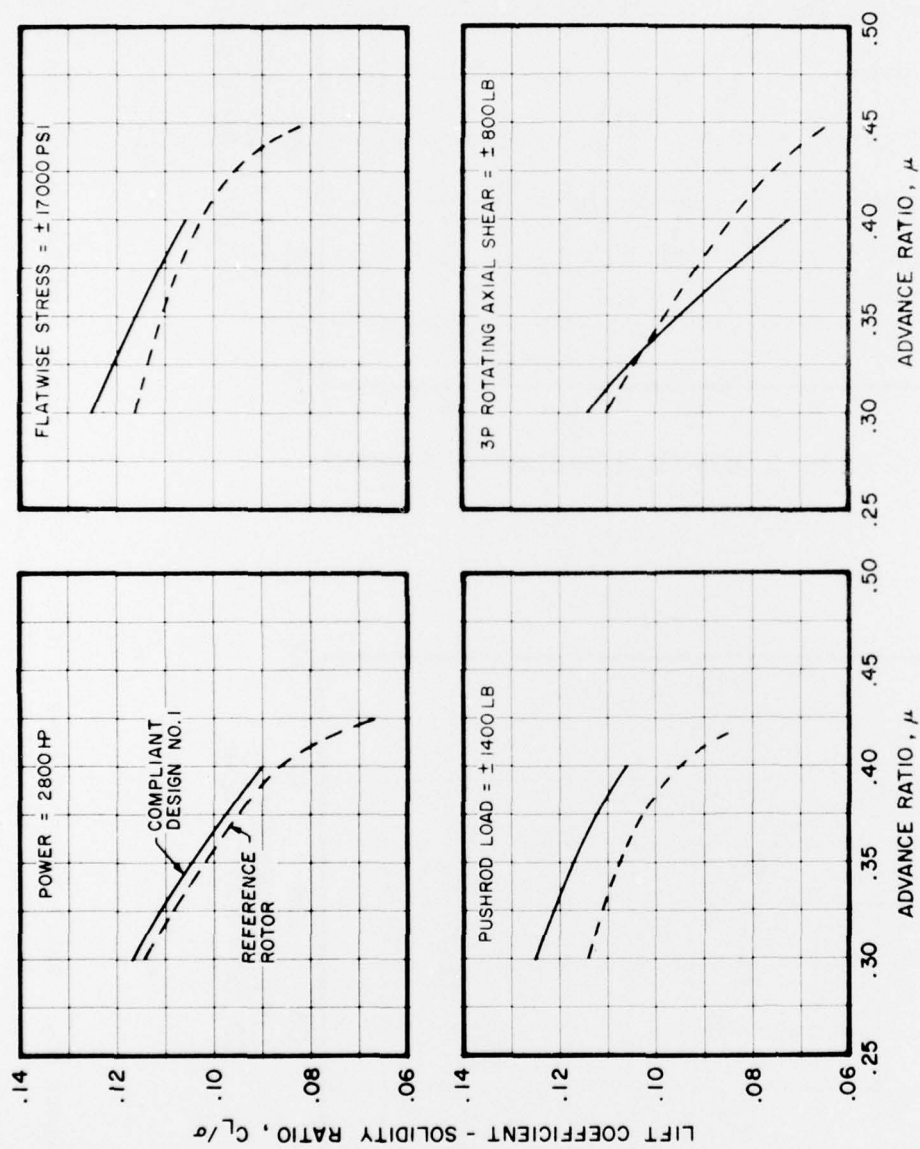


Figure 59. Operating Boundaries of Compliant Rotor Design #1 and Reference Rotor.

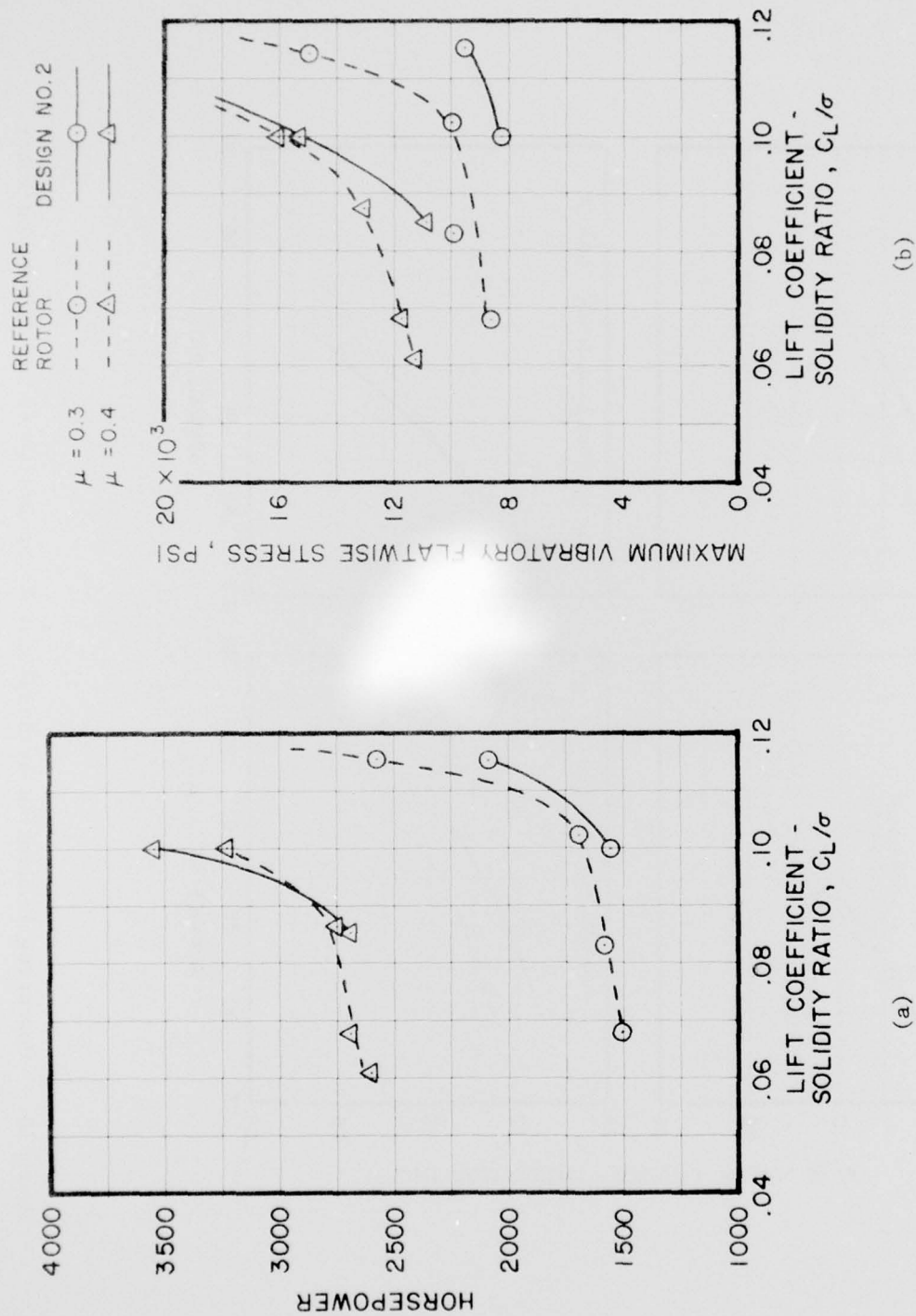


Figure 60. The Buildup of Power, Stress, Control Loads, and Vibratory Shear Force for Compliant Rotor Design #2 and Reference Rotor.

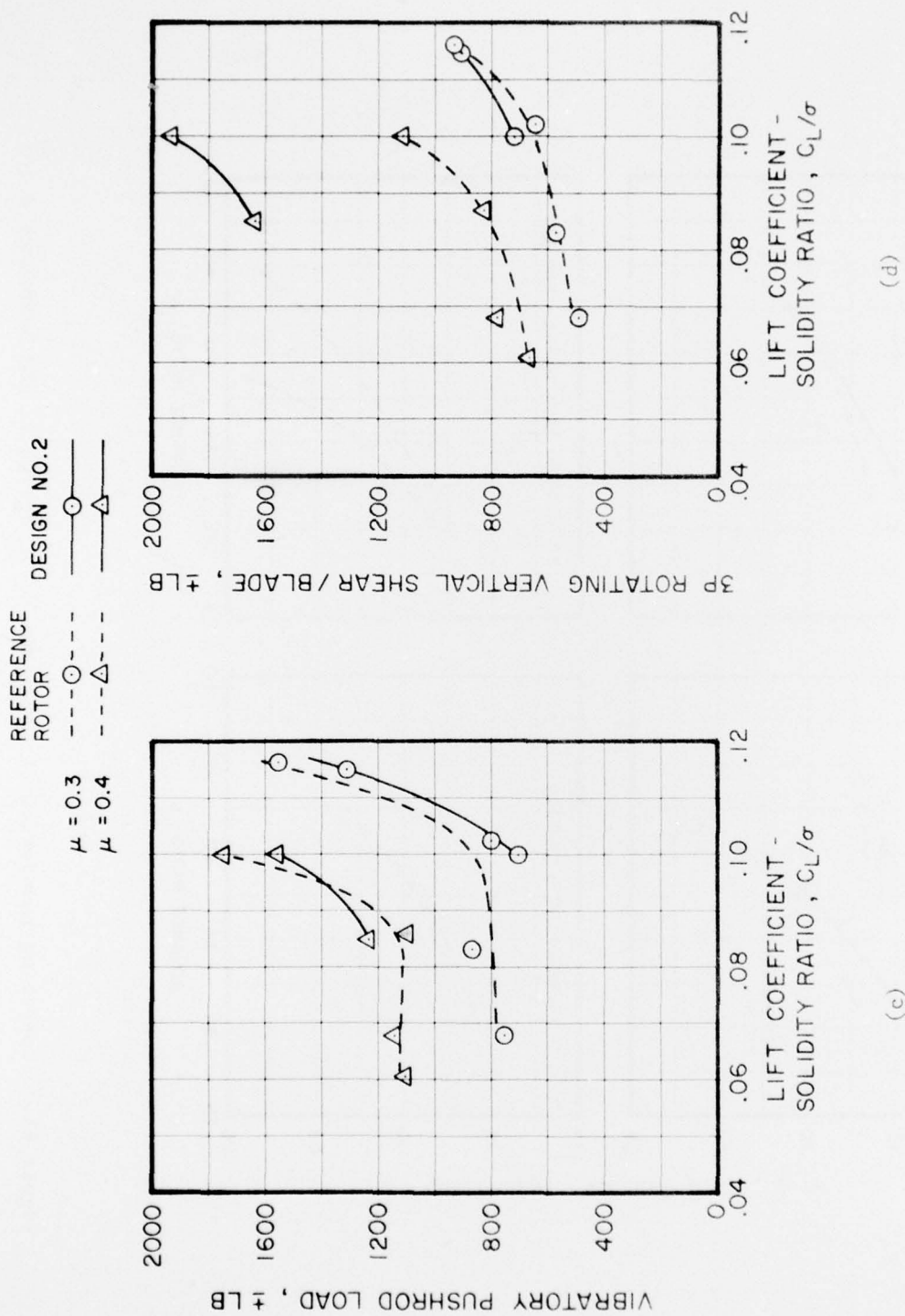


Figure 60. Concluded.

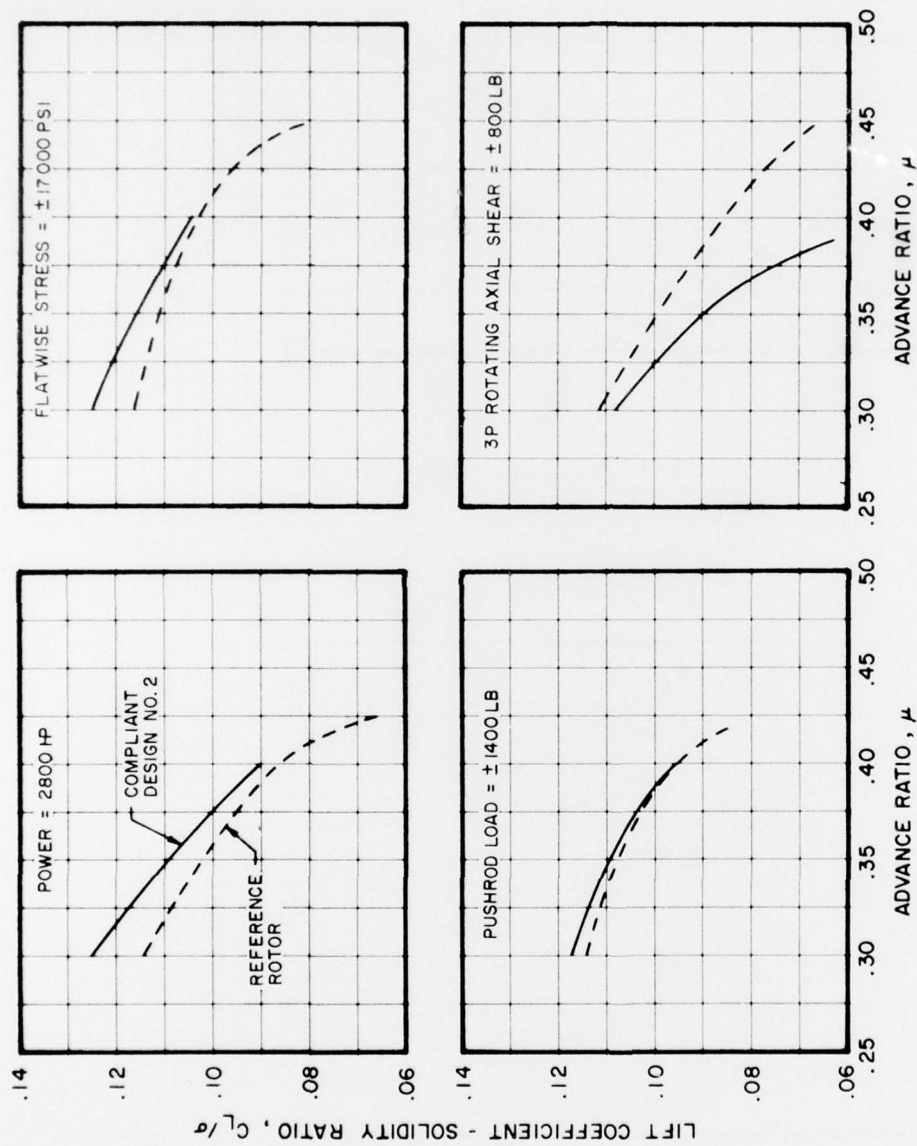


Figure 61. Operating Boundaries of Compliant Rotor Design #2 and Reference Rotor.

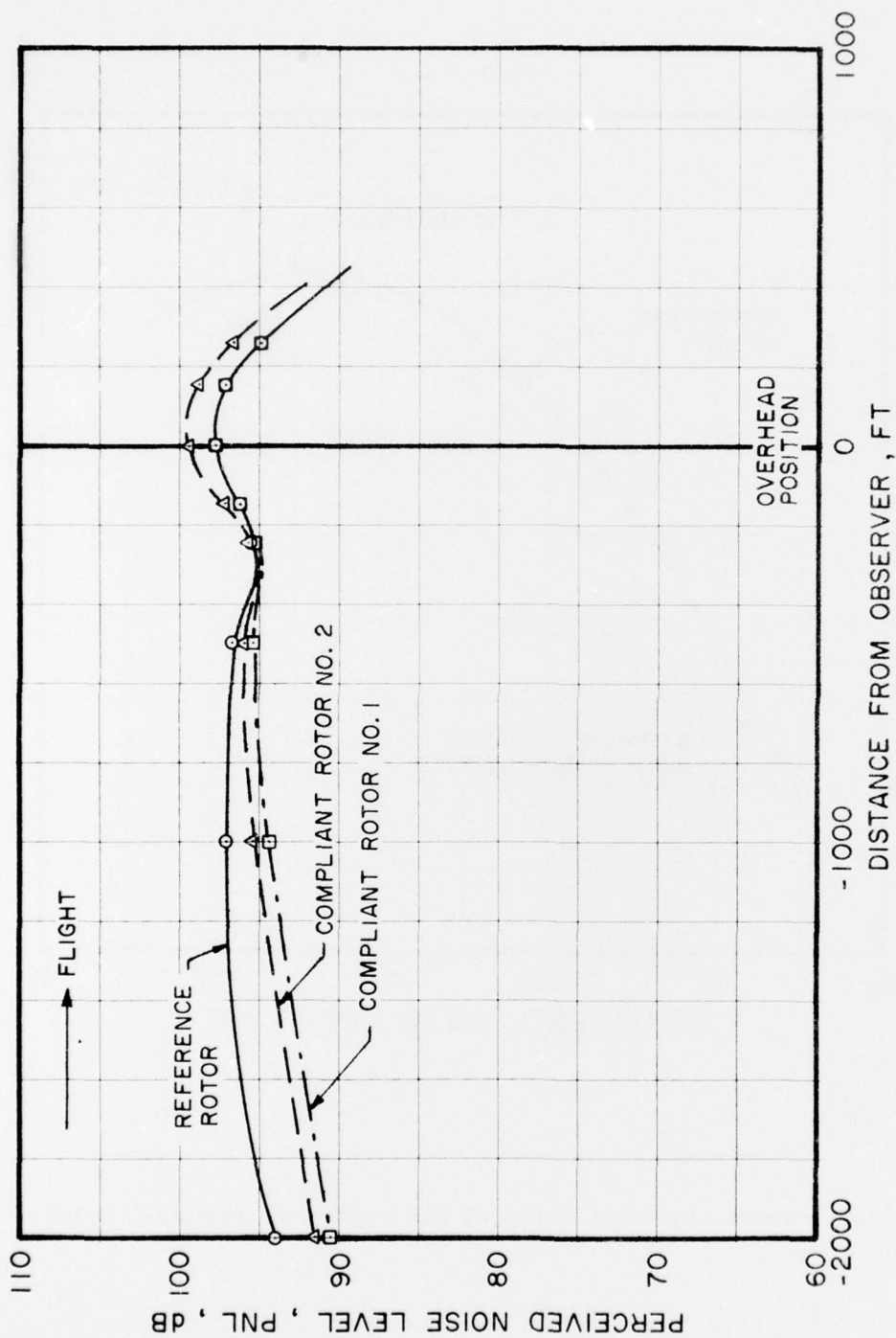


Figure 62. Flyover Perceived Noise Levels of Compliant Rotor Designs and Reference Rotor at $\mu=0.4$ and $C_L/\sigma=0.085$.

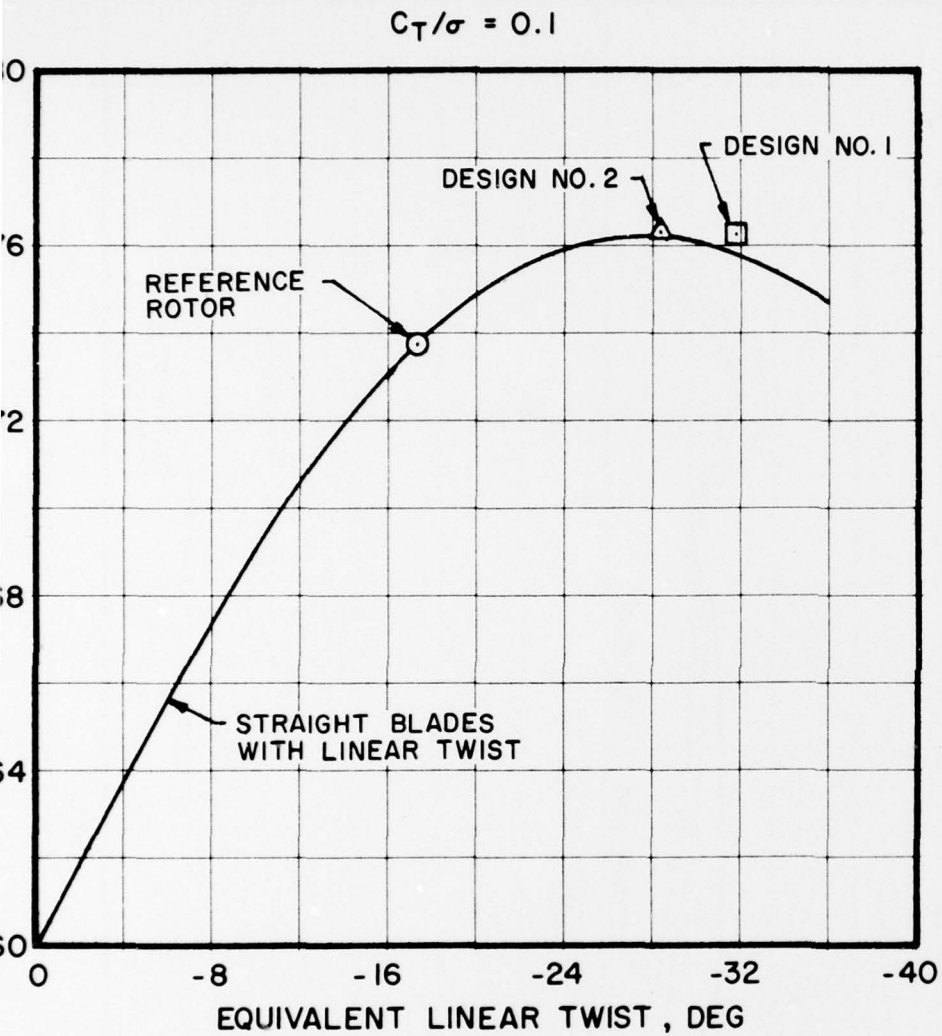


Figure 63. Hover Figure of Merit of Reference and Compliant Rotors.

T
on the
The an
refiner
studies
analyse
accurac
are des

General

Th
method
describ
flappin
equatio
dynamic
tation
stall,
lation
present
elastic
dimensi
ance tr
inflow
desired
automat

Prescrib

The
the dist
Section
angle da
analysis

14. Tan
Rep
Cor
15. Lan
GEO
No.

APPENDIX A

ANALYTIC METHODS

The accuracy of the results and conclusions presented herein hinges on the accuracy of the various analytic models used in the investigation. The analyses used in this study, although they are undergoing continual refinement, reflect the state of the art, and based on past correlation studies, are judged to be reliable. Specific assumptions implicit in the analyses must, however, be borne in mind in assessing the quantitative accuracy of predicted results. The principal analyses used in this study are described below.

Generalized Rotor Performance Analysis (GRP)

The Generalized Rotor Performance Analysis is Sikorsky's standard method for predicting rotor forward-flight performance. Reference 14 describes the analysis in detail. This analysis calculates rigid blade deflection and lead-lag response through timewise integration of the blade equations of motion. Blade torsional response is not modeled. Aeroelastic loading is calculated, based on a segmented lifting line representation of the blade. The analysis uses tabulated airfoil data and treats compressibility, and three-dimensional flow effects in the calculation of rotor performance. Two-dimensional flow was assumed in the application to be consistent with the Normal Modes Blade Aeroelastic Analysis and the Airload Optimization Analysis, which use two-dimensional aerodynamic representations. When used to establish performance trends in preliminary design studies, GRP is run with a uniform inflow determined from momentum considerations. When detailed results are required, the analysis is performed using variable inflow, obtained through an iterative interaction with the Prescribed Wake Inflow Analysis.

Prescribed Wake Inflow Analysis

The UTRC Prescribed Wake Inflow Analysis (Reference 15) calculates the distribution of rotor inflow, based on a prescribed wake model. The operating conditions are prescribed from blade motion and pitch rates, determined either by GRP or the normal modes blade response analysis. This program can be run separately or automatically coupled

Werner, W. H., GENERALIZED ROTOR PERFORMANCE METHOD, Engineering Report SER-50304, Sikorsky Aircraft Division, United Technologies Corporation, May 1964

Ulgrebe, A. J., AN ANALYTICAL METHOD FOR PREDICTING ROTOR WAKE GEOMETRY, Journal of the American Helicopter Society, Vol. 14, No. 4, October 1969, pp. 20-32

with either the GRP or normal modes programs. The analysis represents each blade by a segmented lifting line and the helical wake of the rotor by discrete segmented trailing vortex filaments. Blade loading and circulation distributions are calculated based on section operating conditions and section lift coefficient data. The strengths of the trailing vortex elements are then determined, based on the spanwise variation in bound circulation. The contributions of each of the trailing vortex segments to induced velocity at each blade position is calculated, using the Biot-Savart law. The solution proceeds until the bound circulation distribution, the strength of the trailing vortex elements, and the induced velocity distribution are compatible. A feature recently added to the analysis which is valuable in analyzing compliant rotor behavior is the inclusion of all harmonics of blade torsional response calculated by the normal modes analysis in the calculations of induced velocities. The treatment of exact torsional response in calculating blade circulation and induced velocities increases the reliability of compliant rotor performance, blade stress, and control load predictions.

Normal Modes Blade Aeroelastic Analysis

This computer analysis, which is described in Reference 16, solves the fully coupled blade equations of motion by expanding them in terms of uncoupled flatwise edgewise and torsional blade modes. The modal technique facilitates the numerical integration of blade equations by minimizing dynamic coupling terms. Up to five flatwise, three edgewise, and two torsional modes are considered, in addition to rigid body flap and lag. Blade aerodynamics are based on a lifting line representation. A result of this assumption is the prediction of large fluctuations in blade loading for close blade-vortex passage. Steady and unsteady two-dimensional or steady three-dimensional aerodynamic models are available. The unsteady two-dimensional model described in Reference 9 was used throughout. According to this method, section lift and pitching moment coefficients are assumed to be single-valued functions of angle of attack and its first two time derivatives. Unsteady data measured on an oscillating NACA 0012 airfoil were used to generate tables of c_l and c_m as functions of α , $\dot{\alpha}$, and $\ddot{\alpha}$.

Procedures described in Reference 8 were used to scale the NACA 0012 data to represent SC 1095 effects. Steady drag data were assumed throughout. All cases used variable inflow, calculated with the Prescribed Wake

-
16. Arcidiacono, P. J., PREDICTION OF ROTOR INSTABILITY AT HIGH FORWARD SPEEDS, VOL. I, STEADY FLIGHT DIFFERENTIAL EQUATIONS OF MOTION FOR A FLEXIBLE HELICOPTER BLADE WITH CHORDWISE MASS UNBALANCE, Sikorsky Aircraft Division, United Technologies Corporation; USAAVLABS Technical Report 68-18A, U.S. Army Aviation Materiel Laboratories, Fort Eustis Virginia, February 1969, AD 685860

Inflow Analysis. Iteration between the inflow and response analyses was conducted to establish compatible loading and inflow distributions.

Airload Optimization Analysis

The Sikorsky Airload Optimization Analysis determines distributions of rotor airloads which satisfy specified criteria. The pitch and twist distributions needed to satisfy these criteria are computed. Criteria include minimization of specified harmonics of blade bending moments or root shear forces and minimization of rotor torque. In minimizing harmonics of blade or hub loads, the analysis represents harmonics of structural loading in terms of known modal properties and unknown harmonics of airload at the various radial positions. Airload harmonics are computed which drive stated harmonics of shear or moment to zero, subject to constraints on rotor lift, propulsive force, and trim moments. In seeking optimal performance, the airload analysis determines the radial distribution of angle of attack which minimizes drag torque for fixed blade lift. The analysis is executed iteratively, with GRP in the case of performance optimization and with the normal modes blade response analysis in the case of loads. Based on a selected angle of attack distribution and control and inflow angles calculated with the appropriate response analysis, required time-varying twist is determined and then impressed into the response solutions. Airload optimization and response calculations proceed until consistent twist, airload, and inflow distributions are achieved which satisfy the stated criteria. The optimization analysis uses steady two-dimensional aerodynamics. Either a uniform or variable inflow model can be assumed.

Circulation Coupled Hover Analysis

The Circulation Coupled Hover Analysis Program (CCHAP), described in Reference 17, is the method by which hover performance is calculated at Sikorsky Aircraft. The capability to predict the performance of a wide variety of rotor configurations within 2 percent has been demonstrated. This analysis calculates rotor hover performance using prescribed wake lifting line theory. Rotor load and inflow distributions are determined simultaneously by solving a Kutta-Joukowski matrix consisting of the wake influence coefficients and the local lift curve slopes. The wake influence coefficients used in the matrix solution are obtained from a previous calculation which sums the Biot-Savart influence of each wake segment used to represent a trailing filament.

-
17. Landgrebe, A. J., et al., AERODYNAMIC TECHNOLOGY FOR ADVANCED ROTOR-CRAFT, American Helicopter Society, Symposium on Rotor Technology, August 1976

As with all prescribed wake hover analyses, the accuracy of the calculated performance is dependent on the accuracy of the input wake geometry. Since experimental wake geometries are not available for most rotor geometries, a procedure must be established for specifying the rotor wake geometries for arbitrary rotor designs. CCHAP employs a coupling between the rotor load (or circulation) distribution and the rotor wake geometry which permits an iterative solution for both the rotor loading and the wake. The wake coupling expression was derived by applying a momentum constraint to a simplified, uncontracted wake model and then matching the resulting equation to the experimental wake geometry data described in Reference 15.

LIST OF SYMBOLS

A_{ls}	lateral cyclic pitch, positive for increased pitch at 180 deg azimuth, deg
b	number of blades
B_{ls}	longitudinal cyclic pitch, positive for increased pitch at 270 deg azimuth, deg
bC_{QD}/σ	blade profile drag torque parameter
c_d	section drag coefficient
$c_{d_{min}}$	minimum section drag coefficient
$c_{d_{o_{inc}}}$	minimum incompressible section drag coefficient
c_l	section lift coefficient
$c_{l_{max}}$	maximum section lift coefficient
C_L	rotor lift coefficient, $L/\pi R^2 \rho (\Omega R)^2$
c_m	section pitching moment coefficient
c_{m_0}	below stall section pitching moment coefficient
C_{PF}	rotor propulsive force coefficient, $PF/\pi R^2 \rho (\Omega R)^2$
C_Q	rotor torque coefficient $Q/\pi R^2 \rho (\Omega R)^2 R$
c_Q'	blade torque coefficient, $Q'/\pi R^2 \rho (\Omega R)^2 R$
c_{QD}	blade profile drag torque coefficient, $Q_d/\pi R^2 \rho (\Omega R)^2 R$
c_{QL}	blade lift torque coefficient, $Q_l/\pi R^2 \rho (\Omega R)^2 R$
C_T	rotor thrust coefficient, $T/\pi R^2 \rho (\Omega R)^2$
c_z	blade axial hinge force coefficient, $z/\pi R^2 \rho (\Omega R)^2$
D_E	rotor equivalent drag, $\frac{550}{V}(H_p - H_{p_{PAR}})$, lb
f	aircraft equivalent flat plate area, ft^2
FM	figure of merit, $\frac{1}{2} \frac{C_T}{C_Q}$

FV_{3P}	3P rotating system axial hinge shear force, lb
GJ	blade torsional stiffness, lb-in ²
GJ_B	baseline blade torsional stiffness, lb-in ²
HP	horsepower
HP_{DRAG}	profile drag horsepower
HP_{PAR}	parasite horsepower
K_θ	root torsional stiffness, in-lb/rad
$K_{\theta B}$	baseline root torsional stiffness, in-lb/rad
L	rotor lift, lb
L/D_E	ratio of rotor lift to equivalent drag
ℓ/d	blade element lift-to-drag ratio
nP	frequency of nth harmonic of rotor speed
PNL	perceived noise level, dB
PRL	pushrod load, lb
Q	rotor torque, ft-lb
Q'	instantaneous blade torque, ft-lb
Q_d	instantaneous blade drag torque, ft-lb
Q_ℓ	instantaneous blade lift torque, ft-lb
PF	rotor propulsive force, lb
P_1, P_2, P_3	penalty functions
$\bar{P}_1, \bar{P}_2, \bar{P}_3$	normalized penalty functions
R	radius, ft
S_{4P}	average 4P servo load, lb
T	rotor thrust, lb
V	airspeed, ft/sec
x	blade radial coordinate, ft

z	blade vertical shear force, lb
α	angle of attack, deg
$\dot{\alpha}$	first time derivative of angle of attack, deg/sec
$\ddot{\alpha}$	second time derivative of angle of attack, deg/sec ²
β	blade flap angle, deg
θ_T	blade linear twist angle, deg
θ_{tip}	tip elastic twist angle, positive for noseup twist, deg
θ_{T1s}	1P sine elastic twist component, negative fourier series, deg
θ_{T1c}	1P cosine elastic twist component, negative fourier series, deg
θ_{75}	blade pitch angle at .75R, deg
Λ	sweep angle, deg
μ	advance ratio, $V/\Omega R$
ρ	density of air, slug/ft ³
σ	rotor solidity, ratio of the total blade area to the rotor disk area
σ_F	flatwise stress, lb/ft ²
ψ	blade azimuth position, positive counterclockwise referenced to downstream position, deg
Ω	rotor rotational speed, rad/sec